UNIVERSITÉ CÔTE D'AZUR | ÉCOLE DOCTORALE SCIENCES ET TECHNOLOGIES DE L'INFORMATION ET DE LA COMMUNICATION

Politecnico di Torino 1859

ScuDo Scuola di Dottorato ~ Doctoral School WHAT YOU ARE, TAKES YOU FAR

THÈSE DE DOCTORAT

Contrôle non destructif de produits alimentaires par imagerie microonde et millimétrique

Ali Darwish

Laboratoire d'Electronique, Antennes et télécommunications (LEAT)

Présentée en vue de l'obtention du grade de docteur en Electronique **d'** Université Côte d'Azur **et de** Politecnico di Torino

Dirigée par : Claire Migliaccio / Francesca Vipiana

Soutenue le : 9 avril 2025

Devant le jury, composé de :

Christian Waldschmidt, Professeur des Universités, Ulm Université, Allemagne

Lorenzo Crocco, Directeur de recherche, CNR - IREA Conseil national de la recherche d'Italie, Italie

Hervé AUBERT, Professeur des Universités, Institut National Polytechnique de Toulouse, et d'Laboratoire d'Analyse et d'Architecture des Systèmes Centre National de la Recherche Scientifique (CNRS), France

UNIVERSITÉ FRANCO ITALIENNE | UNIVERSITÀ ITALO FRANCESE

Contrôle non destructif de produits alimentaires par imagerie microonde et millimétrique

---

Controllo non distruttivo dei prodotti alimentari mediante imaging a microonde e onde millimetriche

---

Non-destructive Evaluation of Food Products by Microwave and mmW Imaging

---

Ali Darwish

Jury:

Présidente du jury

Christian Waldschmidt, Professeur des Universités, Ulm Université, Allemagne

Rapporteurs

Lorenzo Crocco, Directeur de recherche, CNR - IREA Conseil national de la recherche d'Italie, Italie

Hervé AUBERT, Professeur des Universités, Institut National Polytechnique de Toulouse, et d'Laboratoire d'Analyse et d'Architecture des Systèmes Centre National de la Recherche Scientifique (CNRS), France

Examinateur

Christian Waldschmidt, Professeur des Universités, Ulm Université, Allemagne

Dirigée par

Claire Migliaccio, Professeur des Universités, Université Côte d'Azur, France

Francesca Vipiana, Professeur des Universités, Politecnico di Torino, Italie

Abstract

Non-destructive Evaluation of Food Products by Microwave and mmW Imaging

Ensuring food safety and quality is a major concern in the food industry, as physical contamination can pose significant health risks to consumers, damage brand reputation, and lead to legal consequences. Common detection methods, such as X-ray inspection, have limitations, particularly in identifying contaminants like plastic, wood, and glass, which have low density and can be difficult to detect. This work explores an alternative solution based on microwave sensing, introducing a novel approach to contamination detection. The proposed system leverages low-power, non-ionizing microwave signals to identify foreign bodies without compromising food integrity or requiring extensive modifications to existing production lines. It offers a cost-effective and real-time inspection method, capable of operating in-line without interrupting the manufacturing process.

The detection principle relies on analyzing how microwave signals interact with different materials, taking advantage of the dielectric contrast between contaminants and food products. A set of antennas surrounding the target captures signal variations, which are then processed to determine the presence of foreign objects. The system is designed to acquire data efficiently while maintaining compatibility with the speed and constraints of industrial food processing environments.

Detecting contaminants in food and beverage products using scattering parameters involves solving an inverse problem, which is nonlinear and ill-posed. This process is computationally expensive and may not be suitable for real-time, in-line detection. In this research, we integrate Machine Learning (ML) techniques to overcome the challenges of the inverse problem and to automate the classification process. We investigate the robustness and effectiveness of different classifiers, such as Support Vector Machines (SVM) and Multi-Layer Perceptron (MLP) networks, by training them on large-scale datasets collected from experimental trials. These models learn to distinguish between uncontaminated and contaminated food items. The classifiers successfully identifies a variety of foreign materials, including different types of plastics, glass, and wood, demonstrating high accuracy across thousands of test cases.

Furthermore, we extend our research to millimeter-Wave (mmW) imaging, investigating the integration of mmW systems with ML tools for nut inspection. The promising results achieved using mmW imaging and ML classification in agrifood applications, particularly for soft fruits like apples and peaches, inspire us to evaluate the effectiveness of this approach for more challenging cases—specifically, in-shell seeds such as almonds and walnuts.

The results obtained in this thesis highlight the potential of the microwave/mmW-based system as a

robust, scalable, and efficient solution for real-time food contamination detection and agrifood inspection. By integrating microwave sensing with machine learning, this approach offers a powerful alternative to traditional inspection methods, improving food safety and quality in industrial settings.

Keywords : microwave imaging, millimeter-Wave imaging, artificial intelligence, remote sensing, Near-field sensing, electromagnetic modeling, antenna.

Évaluation Non-Destructive des Produits Alimentaires par Imagerie Micro-ondes et mmW

Garantir la sécurité et la qualité des aliments est une préoccupation majeure dans l'industrie alimentaire, car la contamination physique peut présenter des risques importants pour la santé des consommateurs, nuire à la réputation de la marque et par là même conduire à des poursuites judiciaires. Les méthodes de détection actuelles, telles que l'inspection par rayons X, présentent des limites, notamment en ce qui concerne l'identification de contaminants tels que le plastique, le bois et le verre, qui ont une faible densité et peuvent être difficiles à détecter, ou encore lorsque les contaminants sont cachés dans le produit. Ce travail explore une solution alternative basée sur la détection par un système exploitant les microondes. L'avantage de cette solution réside dans le caractère non ionisant des signaux envoyés ainsi que dans la possibilité de réaliser un système à faible puissance injectée. Ainsi, identifier les contaminants dans les aliments pourra s'effectuer sans compromettre leur intégrité ni nécessiter de modifications importantes des chaînes de production existantes. De plus, ce système devra fonctionner en temps réel sur une ligne de production, sans que le processus de fabrication ne soit interrompu.

Le principe de la détection repose sur l'analyse de l'interaction des signaux microondes avec différents matériaux, en tirant parti du contraste diélectrique entre les contaminants et les produits alimentaires. La matrice de diffraction collectée par les 6 antennes qui entourent la cible est traitée pour déterminer la présence de corps étrangers. Le système est conçu pour être compatible avec les contraintes des environnements industriels de transformation des aliments.

La détection des contaminants dans les produits alimentaires et les boissons à l'aide des paramètres de diffusion implique la résolution d'un problème inverse, non linéaire et mal posé. Ce processus est coûteux en termes de calcul et difficilement compatible avec une détection sur une ligne de production opérant en temps réel. Dans ce travail de doctorat, nous intégrons des techniques d'apprentissage automatique pour surmonter les difficultés du problème inverse et automatiser le processus de classification. Nous étudions la robustesse et l'efficacité de différents classificateurs, tels que les machines à vecteurs de support (SVM) et les réseaux de perceptrons multicouches (MLP), en les entraînant sur des ensembles de données à grande échelle collectées lors de campagnes de mesure. Ces modèles apprennent à distinguer les aliments contaminés des aliments sains. Les classificateurs identifient avec succès une variété de matériaux étrangers, y compris différents types de plastique, de verre et de bois, sur des milliers de cas de test.

En outre, nous étendons notre recherche à l'imagerie par ondes millimétriques (mmW), en étudiant l'intégration des systèmes mmW avec des outils de ML pour l'inspection de fruits à coque. Cette étude est motivée par les résultats prometteurs obtenus dans cette même gamme de fréquences sur des fruits à peau fine et contenant une grande quantité d'eau, comme les pommes et les pêches. Ici, la présence de la coque ainsi que le fait qu'elle renferme un fruit sec rend l'étude plus complexe.

Les résultats obtenus dans ce travail de doctorat mettent en évidence le potentiel du système basé sur les microondes et les ondes millimétriques en tant que solution robuste, évolutive et efficace pour la détection en temps réel de la contamination des aliments et l'inspection agroalimentaire. En intégrant la détection par micro-ondes à l'apprentissage automatique, nous proposons une alternative puissante aux méthodes d'inspection traditionnelles, améliorant ainsi la sécurité et la qualité des aliments dans les environnements industriels.

Mots clés : imagerie micro-ondes, imagerie millimétrique, intelligence artificielle, télédétection, détection en champ proche, modélisation électromagnétique, antenne.

Controllo non distruttivo dei prodotti alimentari mediante imaging a microonde e onde millimetriche

Garantire la sicurezza e la qualità degli alimenti è una delle principali preoccupazioni dell'industria alimentare, poiché la contaminazione fisica può comportare rischi significativi per la salute dei consumatori, danneggiare la reputazione del marchio e portare a conseguenze legali. I comuni metodi di rilevamento, come l'ispezione a raggi X, hanno dei limiti, in particolare nell'identificazione di contaminanti come plastica, legno e vetro, che hanno una bassa densità e possono essere difficili da rilevare. Questo lavoro esplora una soluzione alternativa basata sul rilevamento a microonde, introducendo un nuovo approccio al rilevamento della contaminazione. Il sistema proposto sfrutta segnali a microonde a bassa potenza e non ionizzanti per identificare i corpi estranei senza compromettere l'integrità degli alimenti o richiedere modifiche alle linee di produzione esistenti. Offre un metodo di ispezione economico e in tempo reale, in grado di operare in linea senza interrompere il processo di produzione.

Il principio di rilevamento si basa sull'analisi del modo in cui i segnali a microonde interagiscono con i diversi materiali, sfruttando il contrasto dielettrico tra contaminanti e prodotti alimentari. Una schiera di antenne, che circondano il prodotto sotto analisi, cattura le variazioni di segnale, che vengono poi elaborate per determinare la presenza di oggetti estranei. Il sistema è progettato per acquisire dati in modo efficiente, mantenendo la compatibilità con la velocità e i vincoli degli ambienti industriali di lavorazione degli alimenti.

Il rilevamento di contaminanti nei prodotti alimentari e nelle bevande utilizzando i parametri di diffusione comporta la risoluzione di un problema inverso, non lineare e malposto. Questo processo è computazionalmente costoso e potrebbe non essere adatto per il rilevamento in linea in tempo reale. In questa ricerca, integriamo tecniche di apprendimento automatico (ML) al problema inverso per automatizzare il processo di classificazione. Analizziamo la robustezza e l'efficacia di diversi classificatori, come le macchine a vettori di supporto (SVM) e le reti di percettori multistrato (MLP), addestrandoli su serie di dati su larga scala raccolti da prove sperimentali. Questi modelli imparano a distinguere tra alimenti non contaminati e contaminati. I classificatori identificano con successo una varietà di materiali estranei, tra cui diversi tipi di plastica, vetro e legno, dimostrando un'elevata precisione su migliaia di casi di test.

Inoltre, estendiamo la nostra ricerca all'imaging a onde millimetriche (mmW), studiando l'integrazione di sistemi mmW con strumenti di ML per l'ispezione delle noci. I risultati promettenti ottenuti con l'imaging mmW e la classificazione ML in applicazioni agroalimentari, in particolare per frutti rossi come mele e pesche, ci hanno stimolato a valutare l'efficacia di questo approccio per casi più impegnativi, in particolare per semi in guscio come mandorle e noci.

I risultati ottenuti in questa tesi evidenziano il potenziale del sistema basato sulle microonde/mmW come soluzione robusta, scalabile ed efficiente per il rilevamento della contaminazione alimentare e l'ispezione agroalimentare in tempo reale. Integrazione del rilevamento a microonde con l'apprendimento automatico offre una potente alternativa ai metodi di ispezione tradizionali, migliorando la sicurezza e la qualità degli alimenti in ambito industriale.

Parole chiave : imaging a microonde, imaging a onde millimetriche, intelligenza artificiale, telerilevamento, rilevamento in campo vicino, modellizzazione elettromagnetica, antenna.

James Clerk Maxwell once said:

"Almighty God, Who hast created man in Thine own image, and made him a living soul that he might seek after Thee, and have dominion over Thy creatures, teach us to study the works of Thy hands, that we may subdue the earth to our use, and strengthen the reason for Thy service."

As a physicist specializing in Electromagnetics, my academic journey began with the study of the fundamental laws of nature—starting with Newton's classical thoughts on the universe and nature, progressing through Maxwell's theory of Electromagnetism, and extending to the modern insights of Einstein and Feynman. Throughout these years, I have often felt humbled by the brilliance and contributions of these great minds. During my PhD, I was fortunate to apply Maxwell's theories in an industrial project designed to benefit and improve human lives. Yet, it is a sobering reality that the same scientific principles can also be used for destruction. This contrast serves as a reminder of the responsibility that comes with knowledge and the importance of using it for the greater good.

I dedicate this thesis to my dearest parents, my brother, my sisters, my nieces, my nephews, and my beloved partner, who have endured my absence throughout these years. Their unwavering support and belief in me have been a source of strength on this journey.

Dedication

Acknowledgements

I would like to express my sincere gratitude to my supervisors, Claire Migliaccio and Francesca Vipiana, for their unwavering support and guidance throughout this journey. I am also thankful to Jorge Tobon Vasquez, Marco Ricci, Jerome Lanteri, Flora Zidane, and Laurent Brochier for their collaboration during this period. I would like to extend my appreciation to Jean-Yves Dauvignac and Rosa Scapaticci for their valuable input and their key roles in the Individual Monitoring Committee meetings. Finally, I offer my thanks to all my colleagues and friends at Polito and UniCA, whose support and companionship have made this experience truly enriching.

I also acknowledge the Franco-Italian University for funding this PhD through the VINCI Program 2021 (C3-1978).

Ali Darwish

Nice, avril, 2025

Author's Publication List

Peer-Reviewed Journal Paper

[J1] A. Darwish, M. Ricci, F. Zidane, J. A. Tobon Vasquez, M. R. Casu, J. Lanteri, C. Migliaccio and F. Vipiana. Physical Contamination Detection in Food Industry Using Microwave and Machine Learning. Electronics, 11(19), 3115 (2022). https://doi.org/10.3390/electronics11193115

[J2] A. Darwish, M. Ricci, J. A. Tobon Vasquez, C. Migliaccio and F. Vipiana. Near-field microwave sensing technology enhanced with machine learning for the non-destructive evaluation of packaged food and beverage products. Sci Rep 14, 13413 (2024). https://doi.org/10.1038/s41598-024-62287-6

Peer-Reviewed International Conference Paper

[C1] A. Darwish, M. Ricci, J. A. Tobon Vasquez, C. Migliaccio and F. Vipiana, "In-Line Microwave Non-destructive Evaluation of Packaged Food Products via the Support Vector Machine Algorithm," 2023 IEEE International Symposium on Antennas and Propagation and USNC-URSI Radio Science Meeting (USNC-URSI), Portland, OR, USA, 2023, pp. 343-344, doi: 10.1109/USNC-URSI52151.2023.10237859.

[C2] A. Darwish, M. Ricci, J. A. Tobon Vasquez, C. Migliaccio and F. Vipiana, "Support Vector Machine for Multiclass Contaminant Classification in Food Products Using Microwave Sensing," 2024 IEEE International Symposium on Antennas and Propagation and INC/USNC-URSI Radio Science Meeting (AP-S/INC-USNC-URSI), Firenze, Italy, 2024, pp. 931-932, doi: 10.1109/AP-S/INC-USNC-URSI52054.2024.10685942.

[C3] A. Darwish, M. Ricci, J. A. Tobon Vasquez, C. Migliaccio and F. Vipiana, "Microwave-Assisted Detection of Physical Intrusions in Commercial Food Packaged Products via Machine Learning," 2024 54th European Microwave Conference (EuMC), Paris, France, 2024, pp. 573-576, doi: 10.23919/EuMC61614.2024.10732555.

[C4] A. Darwish, J. Lanteri, L. Brochier, F. Vipiana, and C. Migliaccio, "Investigation of in-shell seeds MMW classification," 2025 IEEE International Symposium on Antennas and Propagation and INC/USNC-URSI Radio Science Meeting (AP-S/INC-USNC-URSI), Ottawa, Canada, 2025 (accepted paper).

Peer-Reviewed National Conference Paper

[N1] A. Darwish, M. Ricci, J. A. Tobon Vasquez, C. Migliaccio and F. Vipiana, "Détection de contaminants dans les produits agro-alimentaires," 23iéme journées Nationales Microndes, Jun 2024, Juan les Pins, France. , pp.4, 2024. ⟨hal-04608069⟩

Contents

1 Motivation and State of art

1.1 Food contamination concerns

Food is a basic necessity for human beings, but it can also pose serious health risks if it becomes contaminated [1]. Most food safety risks that lead to food contamination can be classified into one of three main categories: biological, chemical, or physical contamination [2, 3]. Across the entire food and beverage industry, physical contamination incidents are relatively common [4]. According to the 2024 report on the challenges and management of foreign material contamination in food, 92% of respondents in packaged food production encounter physical contamination at least once per three months [4]. This suggests that physical contamination represents a significant portion of overall food contamination incidents. Physical contaminants are defined as foreign objects, just a few millimeters in size, that can occur anywhere food is handled or at any stage during the manufacturing process. In the context of food production's unyielding commitment to safety, companies are committed to preventing physical contaminants from entering their different food chain processes, ensuring that they deliver products of the highest safety and quality to the market. However, despite these efforts, numerous recalls still occur all over the world due to physical contaminants entering the food chain, which pose risks to consumers, such as mouth, throat, or intestinal injuries, and broken teeth [2, 5]. This risk applies to all types of food, including beverages, bottled water, and other nutritional products.

In the food manufacturing process, food packaging plays a big role in the quality of the products. It is one of the crucial stages in the production chain, primarily due to materials used in this phase like plastic, glass, metal, and nylon [6]. These materials come from different sources within the production stages. For instance, glass and metal contaminants can result from broken or damaged equipment and machines at different points in the manufacturing process. While, plastics and nylon are frequently encountered at most stages, from equipment to packaging materials, due to their widespread usage [5]. Food manufacturing companies face the challenge of detecting these physical contamination hazards. However, failing to ensure that all food products are free of contamination and safe for consumption could have serious consequences for companies in the food industry. It can severely damage the company's reputation and lead to significant economic losses [3, 7, 8]. For this reason, companies try to find rigorous and reliable inspection techniques to detect physical contaminants in their food products before they reach the market.

Another challenge related to the food industry, particularly in agriculture, is detecting defects in fruits and vegetables using non-destructive methods. Defects in fruits can be classified into two categories: progressive or permanent [9]. Progressive defects are those that evolve, making the condition of the fruit

worse with time, such as mold or open wounds, which can spread and affect the overall quality of the fruit. Permanent defects, on the other hand, do not change over time, such as scars or closed wounds that result from physical damage or bad growth conditions [9, 10]. To detect diseases and defects in fruits and vegetables, expert farmers rely on the traditional method of visual inspection with the naked eye. However, many of these diseases do not appear on the surface of the fruits, making visual inspection and detection impossible. Early detection is necessary and of high importance, because agriculture is a key factor in the socioeconomic development of many countries worldwide. It can help farmers avoid economic losses by identifying defects in produce before they become more problematic.

Based on all these concerns and risks, it is clear that there is a common interest in the food and agriculture industries in implementing a non-destructive inspection system to automatically control the quality of their products. The large-scale production lines and the growing need for traceability require the development of a system that can handle large volumes in real-time to remove damaged products from the production line. In the next section, we will summarize the techniques employed and the approaches explored to address this problem. By the end of this chapter, we introduce our methodology, which aims to resolve the issue and address the gaps left by the previous technologies.

1.2 Existing and Emerging Technologies

In the food industry, there are several ways to implement monitoring and inspection techniques to detect contaminants and defects. These methods include offline, online, at-line, and in-line approaches. Here's an overview of how these methods are applied:

- Offline Monitoring: involves collecting samples from the production line and testing them separately in a laboratory or designated testing area. This approach enables detailed analysis and is particularly useful in cases of biological and chemical contamination, which might not be feasible to address in real-time during production [11].
- Online Monitoring: This method involves diverting a sample from the main production line using dedicated loops or automated sampling systems integrated into the process stream, directing it to a separate measurement area. This setup allows for analysis of the collected samples in an environment that is isolated from the main production process, providing different conditions that may be advantageous for specific types of tests [12, 13].
- At-Line Monitoring: includes testing samples next to the production line using portable equipment. It provides quicker results than offline testing, enabling more frequent checks and the sorting of samples if contamination is detected [13, 14].
- In-Line Monitoring: refers to applications where sensors and detectors are mounted directly within the production process, these systems are placed at specific key control points. This approach provides continuous, real-time inspection and is particularly effective at identifying physical contaminants, such as metal, glass, or plastic fragments, through technologies like metal detectors or X-ray systems [13, 15].

To ensure the highest level of safety and quality in food and beverage manufacturing, it is necessary to test every product that moves along the conveyor belt by a non-invasive technique. From the overview

above, it is clear that in-line inspection methods are the safest and most effective for real-time detection of physical contamination in production chains.

1.2.1 X-Ray Food Inspection

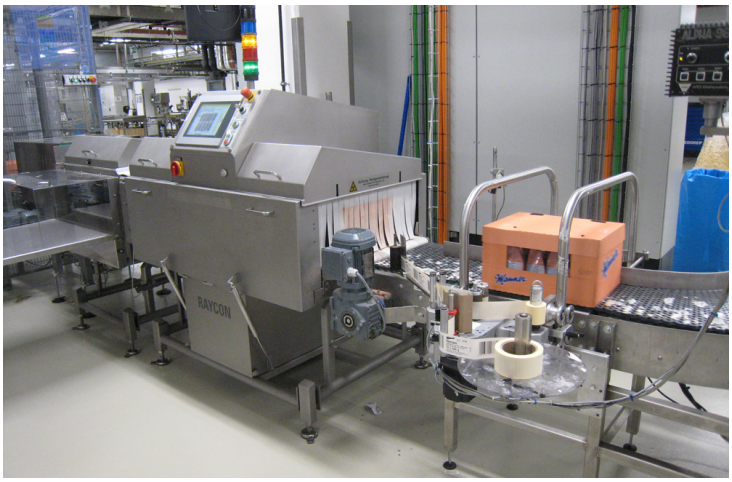

Figure 1.2.1: The X-ray inspection system functions along a conveyor belt [16].

X-rays are invisible electromagnetic waves with short wavelengths and high energy. While most people are familiar with X-ray technology through its use in medical imaging sector, it is also commonly implemented in food inspection. The implementation of X-ray inspection is one of the most widespread technologies to address the problem of detecting physical contamination and defects [17, 18]. X-rays can penetrate food products, allowing the visualization of internal features to detect physical contaminants or defects. However, X-rays have limitations in detecting intrusions like hair, paper, wood, and low-density materials like plastic [19–21]. Additionally, X-ray systems are expensive and require strict safety measures to protect operators from the hazards of ionizing radiation.

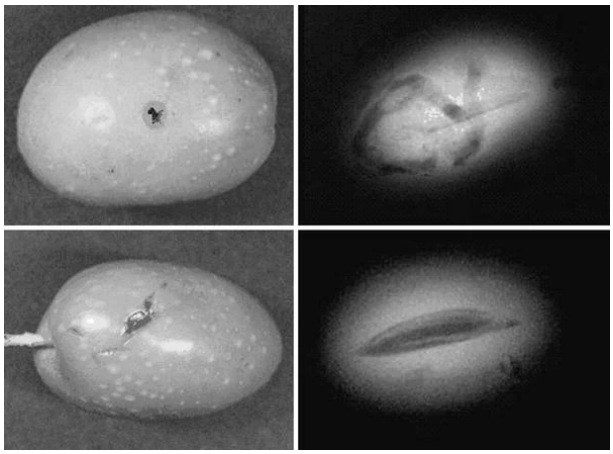

Figure 1.2.2: Digital photographs (on the left) and X-ray images (on the right) of two olives [16].

X-ray food inspection systems, like the one shown in Figure 1.2.1, can handle various types of food, including fresh fruits, grains, nuts, beverages, and packaged foods. Figure 1.2.2 displays X-ray inspection

images of two olives, highlighting the impact of the olive fruit fly on the internal structure of the fruits [22]. In [22], digital photographs and X-ray images compare olives with (top) and without (bottom) fruit fly infestation. The two olives show external damage in the digital photographs. However, X-ray imaging of the first olive reveals extensive internal structural damage, indicating a significant infection. In contrast, for the second olive, the external damage is unrelated to insect presence, as the X-ray image confirms no internal infestation.

1.2.2 Metal detection

Figure 1.2.3: Metal detection system integrated into the production line in the food industry [23].

Metal detection systems, such as the one shown in Figure 1.2.3, are also widely employed in the food industry for the same purpose [23, 24]. They are often used in combination with X-ray systems for comprehensive contamination detection throughout the production process [25]. Modern metal detector systems are highly effective in detecting small particles of ferrous (chrome, steel), non-ferrous (brass, aluminum), and stainless steel contaminants. Ferrous contaminants, which are rich in iron, are both conductive and magnetic. These properties make them easily detectable by metal detector systems. On the other hand, non-ferrous materials are low in iron and are non-magnetic, but they are still conductive, which allows metal detector systems to distinguish them. The critical ones are the stainless steel contaminants, that are known for their poor conductive and non-magnetic properties. These properties make them the most challenging metallic materials to detect, especially in high-salt media [26, 27]. However, they are restricted to identifying metal contaminants. They cannot detect non-metallic materials such as glass plastic and wood [24, 27], which are the main substances food encounters during production. Normally, food manufacturers opt for a single inspection system on their production line, using either metal detection or X-ray inspection. However, due to the many limitations of each system, it may sometimes be necessary to use both at different critical control points (CCPs) along the same production line to avoid false readings.

Figure 1.2.4: NIR imaging system in operation on a batch of olives [28].

1.2.3 Near-Infrared (NIR) spectroscopy

Infrared radiations are electromagnetic radiations generated by molecular vibrations. All objects emit a certain level of infrared radiation; when atoms absorb energy, they release it as infrared waves. Near-Infrared (NIR) spectroscopy is a method that operates in the near-infrared region of the electromagnetic spectrum within a wavelength range of approximately 700 to 2500 nanometers. When NIR light interacts with organic molecules, it causes bond vibrations, leading to energy changes that result in specific patterns of absorption or reflection across different wavelengths [29, 30]. These patterns can be analyzed and captured by NIR sensors, such as charge-coupled devices (CCDs), to determine the characteristics and features of the material being tested. NIR spectroscopy has emerged as a rapid, non-destructive alternative to the aforementioned food safety techniques [31], offering both online and in-line applications. NIR inspection provides valuable data, such as the quantitative analysis of chemical components, the overall quality of the sample, or moisture content. However, NIR spectroscopy has limitations. It relies on chemical reference methods for calibration [32], and due to its limited penetration depth, the spectrometer must be placed very close to or in direct contact with the item being tested as shown in Figure1.2.4. This shallow penetration restricts its effectiveness to detecting surface-level defects or analyzing thin layers, making it less suitable for inspecting the internal contents of packaged food during production.

In [33], the authors presented results of olive imaging using a digital 2CCDs Progressive Scan Multi-Spectral Camera, which is capable of capturing both visible and NIR images simultaneously. Figure1.2.5 displays images of a batch of black and green olives in both the visible and NIR spectrums. The number on each olive categorizes the olive by its level of defects, ranging from 0 to 4. Level 0 is 100% healthy, while Level 4 is 100% defective. The system demonstrates high effectiveness and accuracy in detecting defects within olives, but it still encounters the same limitations discussed earlier in this subsection.

1.2.4 Low-Frequency Terahertz (THz) Imaging

Terahertz imaging [35, 36] is another widely adopted technology in the food industry, used to assess both chemical and physical contamination in food and agricultural products [37]. The technique involves using electromagnetic waves in the terahertz spectrum to analyze the composition and structure of food

Figure 1.2.5: Images of olives in both visible (right) and NIR (left) spectrums [33].

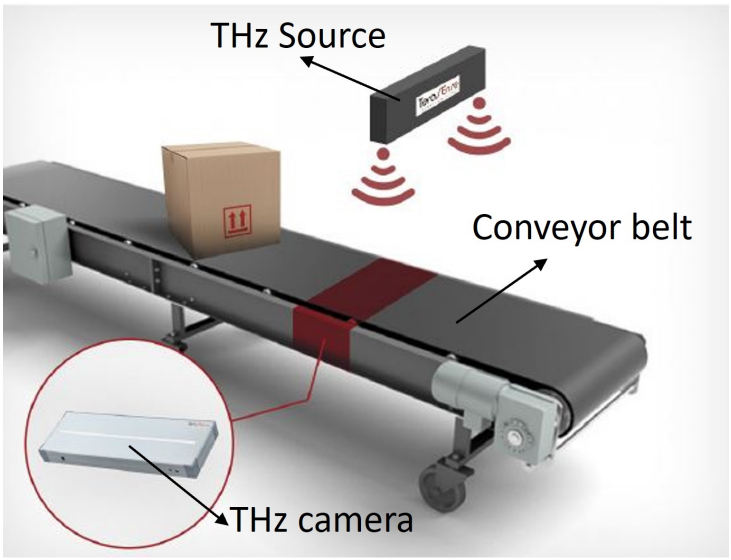

Figure 1.2.6: THz food inspection system [34].

products [38]. THz systems enable high-resolution detection based on the changes in electromagnetic properties in the tested volume. Despite its potential, the implementation of terahertz imaging technology faces several challenges. A major obstacle is the high cost, making it difficult for many food producers to adopt the technology [38, 39]. Additionally, THz waves can only penetrate a few millimeters in water and are highly sensitive to humidity [39, 40].

Figure1.2.7 shows two nuts being tested with a THz imaging system, which consists of a low-requency THz source operating at 100 GHz and a camera positioned below the conveyor belt to capture the signal, as illustrated in Figure 1.2.6. The image displays the transmission levels of the THz waves as they pass through the nuts. The difference in complex permittivity between the healthy nut (lower) and the mycotoxin-contaminated nut (upper) is clearly distinguishable in the transmission levels shown in Figure1.2.7.

Another test was conducted using the same system, this time to verify the presence of peanuts inside a nutshell, as shown in Figure1.2.8. Figure1.2.8(a) displays the nutshell under visual inspection, alongside

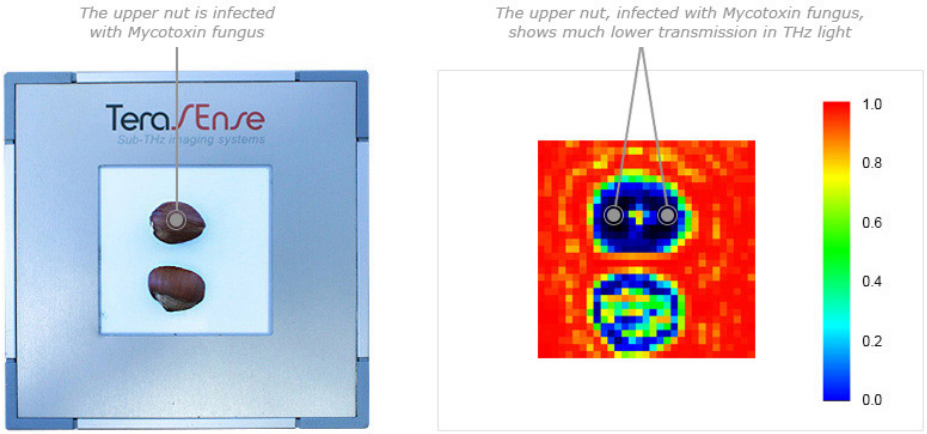

Figure 1.2.7: Terahertz images of two nuts [34].

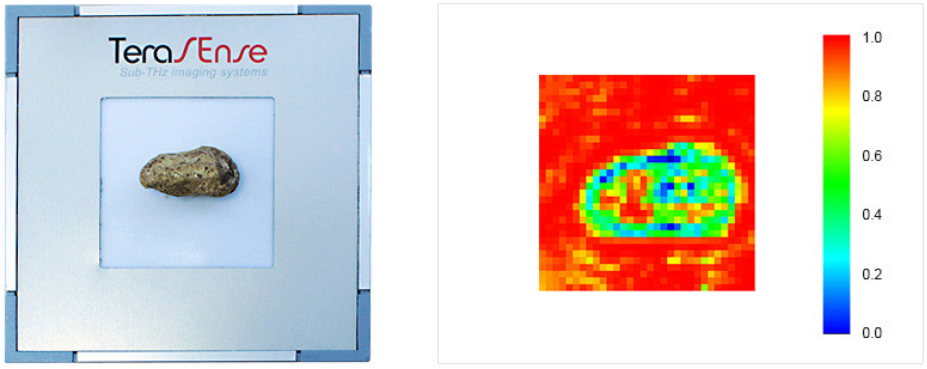

(a)

(b)

Figure 1.2.8: Terahertz image of a nutshell [34]: (a) The Terahertz map of the nutshell highlights high transmission in the empty space within. (b) A visible photograph of the nutshell, showing the location of the peanut inside.

the THz imaging of the same nutshell. The transmission signal's magnitude is higher in areas where there is no peanut inside, as clearly seen in the reconstructed THz image. By comparing Figures 1.2.8(a) and 1.2.8(b), it is evident that the lower transmission level in the THz image corresponds to the side of the shell containing a single peanut.

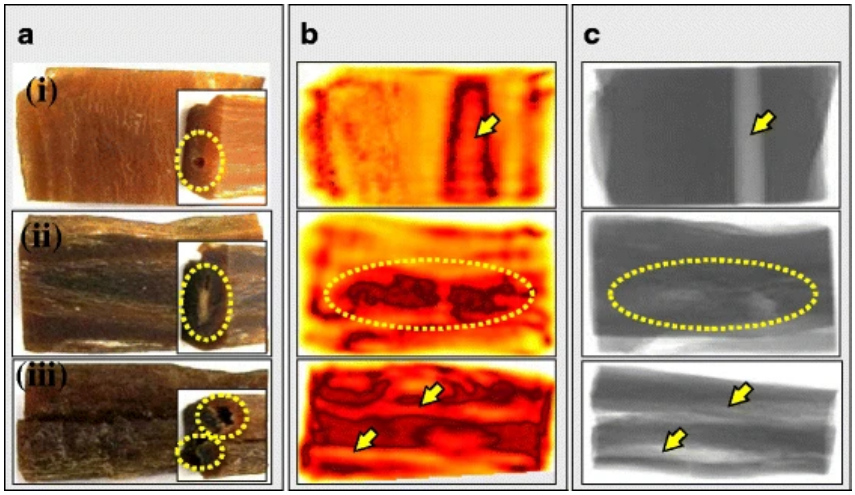

Figure 1.2.9: Red ginseng under test [41]: (a) The visible photographs. (b) The Terahertz inspection images. X-ray scan of the red ginseng.

Additional results are obtained using continuous-wave THz imaging with a horn antenna operating at 200 GHz (λ = 1.5 mm) as reported in [41]. The results pertain to testing red ginseng for food quality control, comparing findings from THz measurements with those from an X-ray scanning system. Figure1.2.9 shows three different red ginseng samples under test, labeled from i to iii, in three different inspection systems: visual (a), THz system (b), and X-ray system (c). The results clearly demonstrate the high resolution of THz inspection, which can precisely detect defects and their borders compared to the X-ray inspection system.

1.2.5 Summary

Table 1.2.1: This table summarizes the advantages and disadvantages of the technologies discussed before.

In-line technologies	Detection	Limitations
X-ray	Metals, glass, and rubber	High cost, ionizing radiation, and ineffective in detecting low-density materials
Metal detectors	Metals	Only capable of detecting metals
NIR	Metals, glass, and rubber	Requires calibration, limited penetration depth
THz imaging	Analysis of chemical and physical properties	High cost, and strongly absorbed by water

To summarize this section, Table 1.2.1 highlights the detection capabilities and limitations of each inspection system. Despite the implementation of these technologies, whether separately or in combination for a more efficient and comprehensive evaluation of food products, the food industry continues to

experience significant recalls of food and beverage items due to physical contamination [42–45] (detailed in Table. 1.2.2). This ongoing issue underscores the urgent need for companies in the food industry to actively seek and implement new technologies to address this problem and overcome the limitations of the current technologies.

Table 1.2.2: Recalls of food and beverage products in 2022 due to physical contamination (PC) according to U.S Food and Drug Administration (FDA) and the U.S Department of Agriculture (USDA).

	Total recalls	PC recalls	Reference
USDA	45	9	[44]
FDA	242	17	[45]

1.3 Microwave Imaging and Sensing: Principle and State of the Art

Like THz imaging, microwave and mmW inspection systems rely on variations in electric properties within the volume being tested. However, they offer a greater penetration depth, particularly in microwave, compared to THz, NIR, and X-ray inspection systems. A key advantage of microwave technology is that it operates at lower frequencies, allowing for simpler, less expensive electronics, which makes the equipment more compact and affordable compared to other technologies. These characteristics of microwaves present it as a powerful alternative non-destructive technique to be investigated and explored in different fields.

Significant interest in MicroWave Imaging (MWI) started to appear in the late 1970s and early 1980s, primarily in the field of medical applications [46–48]. Microwave tomography provides two [49] or three-dimensional [50] images of an object of interest based on the dielectric properties. The difference in the complex permittivity between the main material of the object under test and the intrusion that might be present within this medium causes an alteration in the scattering behavior of the impinging waves. In most MWI techniques, multiple antennas are positioned around the region of interest, functioning in both transmitting and receiving modes on either a single frequency or multiple frequencies. The retrieved data is processed using specialized algorithms known as inverse scattering techniques, which enable quantitative or qualitative analysis of the dielectric properties. Qualitative imaging relies on approximations to reconstruct an image that reveals the geometrical features of the Region of Interest (ROI). On the other hand, quantitative imaging provides numerical values for the electromagnetic properties in each section of the volume by solving an inverse problem.

Microwave sensing and imaging technology has emerged over the years as a powerful and promising alternative for non-destructive testing, offering excellent diagnostic capabilities across various fields. In biomedical applications, it has been explored for breast cancer detection [51–53] and brain imaging, such as stroke diagnosis [54–58]. It is also applied in Non-Destructive Evaluation (NDE) for material and structural characterization [59], geophysical uses like detecting concealed targets with Ground-Penetrating Radar (GPR) [60], and industrial applications, including near-field diagnostics for circuits and antennas [61]. The application of microwave technology across these fields relies on its ability to detect the contrasts in the complex permittivity between an object under test and a foreign target. This capability paves the way for exploring microwave technology in other industrial applications, such as food monitoring [62–65].

1.3.1 Microwave Measurement Techniques

Microwave measurement systems are designed using different configurations of front-end sensor units (antennas) and processing devices. Different microwave techniques for characterizing electric properties, such as permittivity, permeability, and conductivity, are widely applied in food measurement [66, 67]. Commonly used methods include open-ended coaxial probe reflection measurement, waveguide transmission measurement, horn antenna free-space measurement, and resonator cavity measurement. The system setups for microwave measurement methods are shown in Figure 1.3.1.

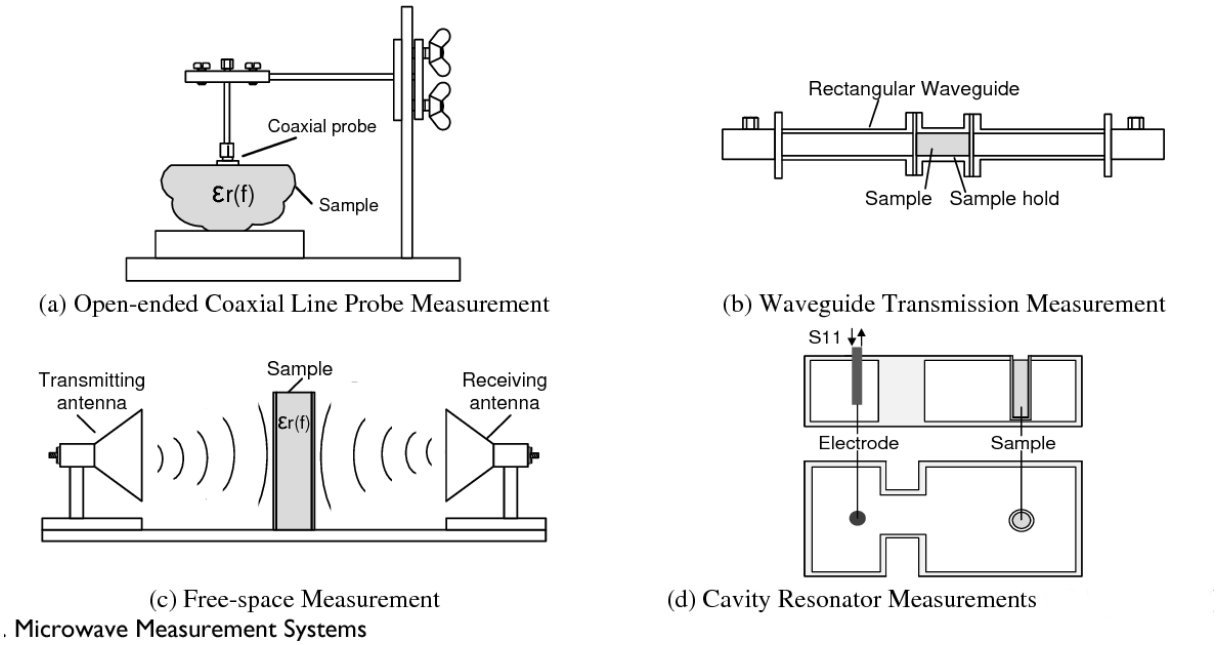

(a) Open-ended Coaxial Line Probe Measurement

(b) Waveguide Transmission Measurement

(c) Free-space Measurement

(d) Cavity Resonator Measurements

Figure 1.3.1: Microwave-based measurement methods [67]

1. **Open-Ended Coaxial Probe** (Figure 1.3.1(a)): A convenient technique for measuring the complex permittivity of liquids and semi-solids, commonly applied in measuring the complex permittivity of food and beverages [68], as well as evaluating meat quality [69].

2. **Transmission Lines and Waveguides** (Figure 1.3.1(b)): These techniques are preferred to be used at frequencies ranging from approximately 2.45 to 30 GHz [67] and support various configurations, including transmission, resonant cavity, and free-space methods. Applications include analyzing fat and salt content in beef [70] and monitoring muscle changes during meat aging [71].

3. **Free-Space Measurement** (Figure 1.3.1(c)): Used at microwave frequencies for obtaining transmission coefficients and precise permittivity measurements. It has been applied to determine moisture content in wheat and organic bulk materials [72] and in measuring the complex permittivity of cereal grain and oilseed [73].

4. **Cavity Resonator** (Figure 1.3.1(d)): Provides high-accuracy characterization by measuring shifts in resonant frequency and Q factor changes. Applications include moisture determination in food [74].

Case study: 1

An example of applying microwave free-space measurements in agriculture was demonstrated in 2014, when a research group in Thailand estimated the ripeness of durians (a tropical fruit) by only measuring the transmission coefficient S_{21} over a frequency range from 700 MHz to 2.7 GHz [75]. The study did not involve any imaging techniques or processing; it was based solely on analyzing the recorded scattering parameters specially the S_{21}. The motivation for this experiment came from the fact that durian fruit has a complex permittivity that changes with its level of ripeness. Specifically, the real part ($\epsilon^{'}$) decreases from 60 to 50 at a maturity stage of 50-70%, while the imaginary part ($\epsilon^{''}$) remains constant around 14 [76]. The variation in the real part of the complex permittivity of durian fruits at different maturity levels can be interpreted from an electromagnetic perspective, reflecting the fruit's ability to store energy inside or transmit the waves through it. A decrease in $\epsilon^{'}$ enhances the fruit's transparency to microwave, permitting increased wave transmission, whereas an increase in $\epsilon^{'}$ indicates a higher capacity for microwave energy storage within the fruit.

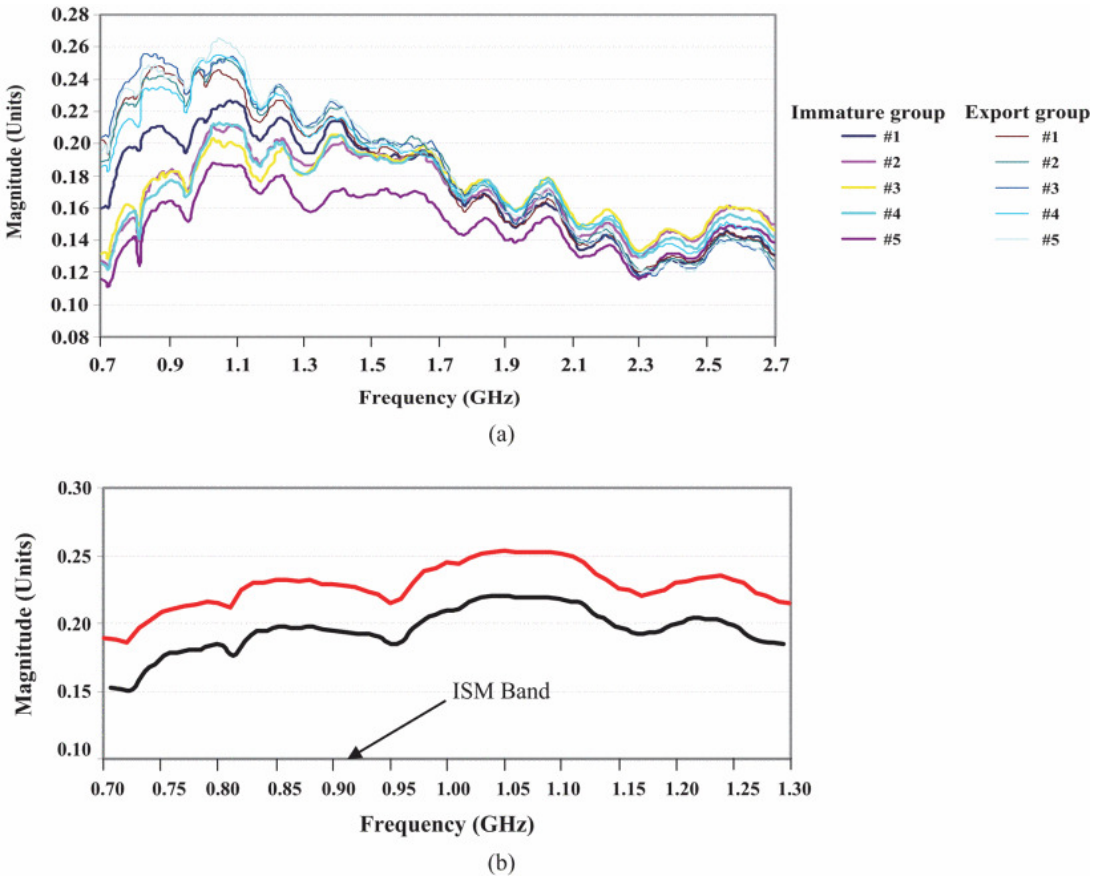

Figure 1.3.2: Measurement results [75]: (a) The magnitude of S_{21} for both immature and exported durians. (b) Averaged values for the immature group (black curve) and the export-ready group (red curve) across the frequency range of 0.7–1.3 GHz.

In [75], the authors proposed a method to classify durian maturity levels using microwave by comparing the S_{21} parameters of various durian samples. The system consisted of a transmitter and receiver antenna pair operating from 700 MHz to 2.7 GHz, calibrated by measuring the reference S_{21} without

a fruit sample between the antennas. The measured S_{21} values for different durian samples were subtracted from the reference, and the absolute values of the results, $|S_{21}|$, are shown in Figure 1.3.2. Figure 1.3.2(a) displays the $|S_{21}|$ for ten different samples, divided into two groups: immature (ranging from 50% to less than 70%), and ready for export ($\approx$ 70%). Figure 1.3.2(b) presents the averages for the two groups, clearly illustrating the lower $|S_{21}|$ values for the immature group (the black curve) compared to the export-ready group (the red one).

Case study: 2

Similar approaches, based on variations in the complex permittivity of food, have been conducted in [63]. Microwave spectrometry has proven to be a sufficiently sensitive technique for determining the sugar concentration in water and yogurt solutions, with measurements taken across a frequency range from 1 GHz to 20 GHz. The authors measured the complex permittivity of yogurt using an Agilent 85070C coaxial probe [63] coupled with a Vector Network Analyzer (VNA). Figure 1.3.3 illustrates the effect of sugar concentration on the real Figure 1.3.3(a) and imaginary Figure 1.3.3(b) components of the complex permittivity as a function of frequency. The permittivity values differ from those of pure water, with the real part of permittivity decreasing as the sugar concentration in yogurt increases. For the imaginary part, values increase with frequency and stay nearly constant across various sugar concentrations up to 7 GHz, after which they begin to decrease as concentration increases.

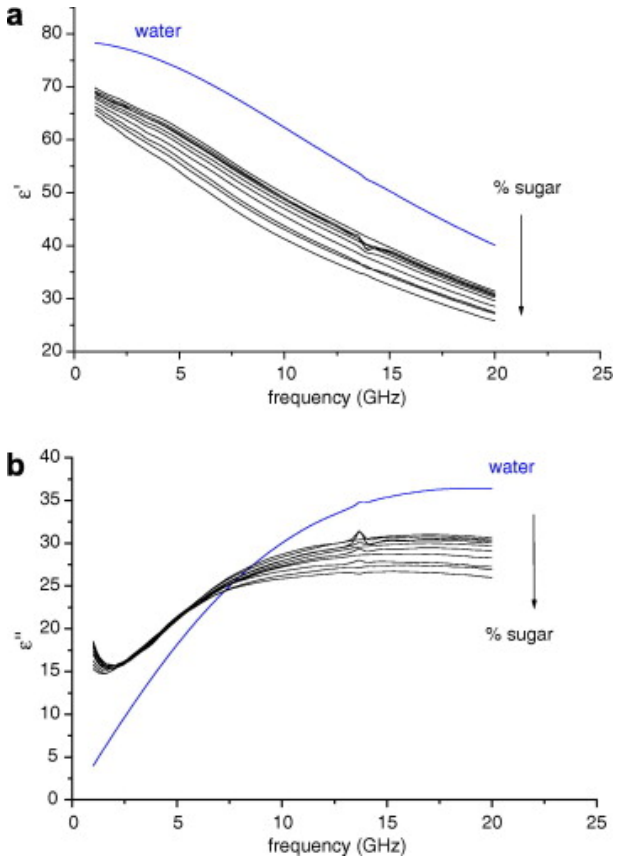

Figure 1.3.3: Microwave spectra corresponding to various sugar concentrations in yogurt [63]: (a) The real part of the complex permittivity. (b) The imaginary part of the complex permittivity.

Over the past decade, microwave technology has gained recognition as a powerful tool in the fields of food and agriculture, as it has the potential to overcome the limitations of the previously mentioned techniques used in food monitoring. It stands out as a favorable option due to its good penetration depth, low cost, non-ionizing radiation, and simplified system design compared to the other adopted technologies. The promising results of applying microwave technology for non-destructive testing of different types of foods and fruits have paved the way for more advanced analyses. Microwave technology can be used to extract detailed information from tested food items, including identifying defects in various fruits and nuts or detecting physical contaminants within food packages. This is achieved using MWI techniques, which require solving the inverse problem.

1.3.2 Microwave Imaging and Sensing: Principles and Inverse Scattering

As previously mentioned, MWI involves using microwave signals to detect targets within the region of interest. This process is carried out by illuminating a volume under test using a set of antennas that produce low-power signals, which are emitted and received by the multiple antennas at one or more frequency points. The aim of the imaging process is to quantitatively describe an object under test by collecting the retrieved scattering parameters data at a specified number of discrete sample points along the boundaries of the region of interest (i.e., where the antennas are positioned). This involves creating a comprehensive map of the volume's physical properties by solving the inverse scattering problem, as the electromagnetic fields can only be sampled at a specific number of locations on the domain's boundaries.

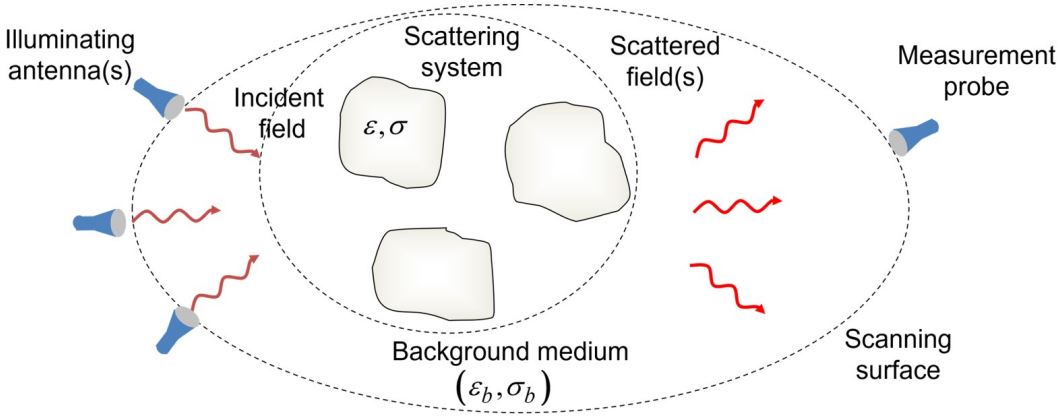

Figure 1.3.4: Microwave imaging scenario: within the investigation domain, which is surrounded by a background medium, the scatterers produce scattered fields when illuminated by the incident fields from the antennas.

Figure 1.3.4 illustrates a scenario that mimics a microwave imaging problem. A set number of transmitting and receiving antennas are arranged at specific positions along the scanning surface, which forms the boundary surrounding the volume under test. The background medium, represented by $(\varepsilon_b, \sigma_b)$, corresponds to the primary material of the food in the case of food monitoring, while the scattering system, denoted by (ε, σ), indicates the presence of a physical intrusion within the food package. The presence of contaminants within the radiated domain creates a contrast in the complex permittivity, $\Delta\chi$, between the background and the intrusions. This $\Delta\chi$ alters the scattering behavior of the electric fields, resulting in variations in the measured scattering matrices, ΔS. $\Delta\chi$ is defined as:

$$\Delta\chi = \frac{\varepsilon_c - \varepsilon_b}{\varepsilon_b} \tag{1.3.1}$$

where ε_c and ε_b are the complex permittivity of the intrusion and the background within the volume under test respectively.

The antennas surrounding the ROI capture the multi-view scattering matrix of the system, which includes the food package, the antennas, and the air in between. To evaluate the dielectric contrast change, $\Delta\chi$, the difference in the scattering matrices, ΔS, between the measured scenario and the reference scenario must be calculated. When the food product is illuminated, the presence of contaminants will lead to a variation of the measured scattering matrices. In the context of food monitoring, the measured scenario corresponds to the case where the food jar may contain an intrusion, while the reference scenario represents a case where it is confirmed to be free of any intrusions.

(a) (b) (c)

Figure 1.3.5: The different electric fields in a microwave imaging scenario. (a) E_{inc}, (b) E_{tot}, and (c) E_{scat}.

The total electric field (E_{tot}) in this scenario arises from the combination of the incident electric field (E_{inc}), representing the field with no scatterers in the domain, and the scattered field (E_{scat}), produced by the scatterers. The three different electric fields are shown in Figure 1.3.5 and the relationship between them is as follows:

$$E_{tot} = E_{inc} + E_{scat} \tag{1.3.2}$$

One of the key challenges in MWI systems is that, while they can capture the electromagnetic fields generated by radiating sources, they are unable to account for contributions from non-radiating sources. This limitation leads to a loss of information, making the problem inherently ill-posed and non-linear. Additionally, the scattered signals are influenced in a non-linear behaviour by the potential presence of contaminants. The chosen solution involves a linearization based on assumptions valid for the given scenario, followed by regularization. From an imaging perspective, the contaminant inside the food jar can be assumed as a small perturbation inside the medium, making a differential imaging approach an appropriate choice [53, 65, 77]. The input data for an imaging problem is ΔS here, representing the difference between the scattering parameters S, measured for a given food product and the scattering parameters S_b measured for the “reference” product (the product without any contaminants). The output is an image that displays the variation in electric contrast $\Delta\chi$, within the food product caused by the contaminant. Given the known background field (the food), the small perturbation represented by $\Delta\chi$, and the small impact of the scatterers on the incident field, we can apply the distorted Born Approximation

(DBA) [78] to calculate $\Delta\chi$ starting from ΔS. The problem can thus be modeled as the inversion of the following equation:

$$\Delta S(\mathbf{r}_p, \mathbf{r}_q) = \mathcal{L}\{\Delta\chi\} = -\frac{j\omega\varepsilon_b}{2}\int_D \mathbf{E}_b(\mathbf{r}_p, \mathbf{r}) \cdot \mathbf{E}(\mathbf{r}, \mathbf{r}_q)\Delta\chi(\mathbf{r})\, d\mathbf{r} \tag{1.3.3}$$

where:

- D is the Region of Interest (ROI), i.e., the volume of the object under evaluation (the food/beverage product)
- $\mathcal{L}\{\Delta\chi\}$ represents the integral operator that relates the difference in the scattering matrices, S, to the change in dielectric contrast, $\Delta\chi$. The kernel of $\mathcal{L}$ is given by $-j\omega\varepsilon_b/2 * \mathbf{E}_b(\mathbf{r}_p, \mathbf{r}) \cdot \mathbf{E}(\mathbf{r}, \mathbf{r}_q)$, for $\mathbf{r} \in$ D. This kernel is computed offline for all antenna combinations p and q, as well as for all positions within the ROI.
- $\mathbf{r}_p$ and $\mathbf{r}_q$ are the positions of the Rx and Tx antennas on the measurement surface
- $\mathbf{E}_b(\mathbf{r}_p, \mathbf{r})$ represents the known "background" electric field radiated in the ROI by the antenna located at $\mathbf{r}_p$ when the volume has no foreign object (E_{inc}), thus $\Delta X = 0$
- $\mathbf{E}(\mathbf{r}, \mathbf{r}_q)$ is the total field in the ROI measured by the antenna located at $\mathbf{r}_q$, given as the superposition of the incident field $\mathbf{E}_b(\mathbf{r}, \mathbf{r}_q)$ (independent of ΔX) and the resulting scattered field $\mathbf{E}_{scat}$ caused by ΔX (i.e., $\mathbf{E}(\mathbf{r}, \mathbf{r}_q) = \mathbf{E}_b(\mathbf{r}, \mathbf{r}_q) + \mathbf{E}_{scat}$)
- the symbol "·" denotes the dot product between vectors
- ε_b is the "background" dielectric constant
- ω is the operating angular frequency used by the antennas, with $\omega = 2\pi\mathbf{f}$

Equation 1.3.3 can be linearized using the Born approximation, assuming weak scatterers; in this case, the total field is approximated by the incident field, such that $\mathbf{E}(\mathbf{r}, \mathbf{r}_q) \approx \mathbf{E}_b(\mathbf{r}, \mathbf{r}_q)$. Consequently, $\mathcal{L}$ is replaced by $\mathcal{L}_{\mathbf{Born}}$, and leads to:

$$\Delta S(\mathbf{r}_p, \mathbf{r}_q) = \mathcal{L}_{\mathbf{Born}}\{\Delta\chi\} = -\frac{j\omega\varepsilon_b}{2}\int_D \mathbf{E}_b(\mathbf{r}_p, \mathbf{r}) \cdot \mathbf{E}_b(\mathbf{r}, \mathbf{r}_q)\Delta\chi(\mathbf{r})\, d\mathbf{r} \tag{1.3.4}$$

where $\mathcal{L}_{\mathbf{Born}}$ is the linear integral operator relating the aforementioned variation of the scattering matrices ΔS to the dielectric contrast $\Delta\chi$ inside D. The linearized equation can then be evaluated using its discretized form, as follows:

$$[\Delta S] = \mathbf{L}[\Delta\chi] \tag{1.3.5}$$

A commonly used method to solve 1.3.5 is the truncated singular value decomposition (TSVD) algorithm [78], where the unknown differential contrast function is determined using a regularized inversion formula, presented as follows:

$$\Delta\chi = \sum_{n=1}^{T} \frac{1}{\sigma_n}\langle[\Delta S], [\mathbf{u}_n]\rangle[\mathbf{v}_n] \tag{1.3.6}$$

wherein σ_n, $[\mathbf{u}_n]$, and $[\mathbf{v}_n]$ are the n-th singular value, and the right and left singular vectors of $[\mathbf{L}]$, respectively. T is the truncation index, chosen to adequately balance between reconstruction stability (concerning data noise and modeling inaccuracies) and image definition (in terms of resolution) [78].

MWI systems have the capability to produce tomographic images; however, in this thesis, the focus shifts to utilizing the raw measurement data produced by these systems directly with machine learning (ML) algorithms to classify food and beverage samples, bypassing image creation and solving the inverse problem. This approach enables faster processing, aligning with the speed requirements of real-time production line operations. For this reason, we refer to the technology as Microwave Sensing rather than Microwave Imaging. Nonetheless, the fundamental principles of the inverse problem, as outlined in this subsection, are consistent across both approaches.

1.3.3 Microwave Imaging for Monitoring in the Food and Agriculture Industry

Recently, there has been increasing interest in applying MWI and sensing technologies, within the food industry. Researchers have investigated the use of MWI principles for detecting physical contaminants in packaged foods and beverages. This subsection highlights key recent studies and research in this area. A common goal across these studies has been to develop an MWI system that detects physical contaminants in food packages using a non-invasive method, seamlessly integrable into a production line.

Case study: 1

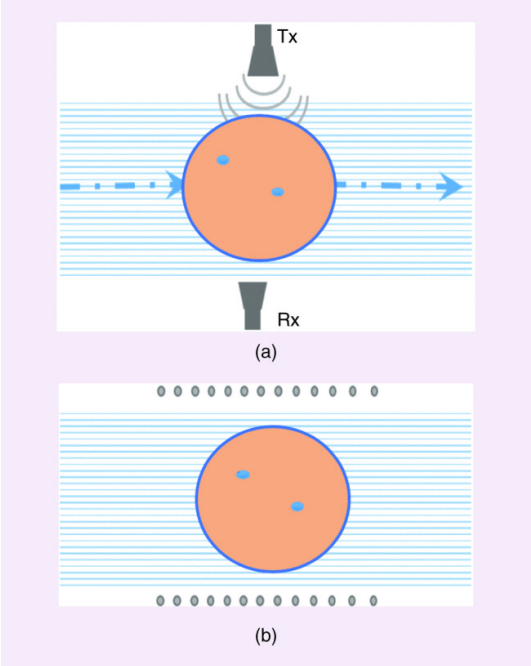

Figure 1.3.6: Concept of the MWI system [65]: (a) a food product (orange circle) moves along the production line (direction indicated by dashed arrows) with two antennas positioned on either side, and (b) an equivalent setup using two virtual antenna arrays (gray dots) on both sides of the line with the food product centered. Rx: receiver; Tx: transmitter.

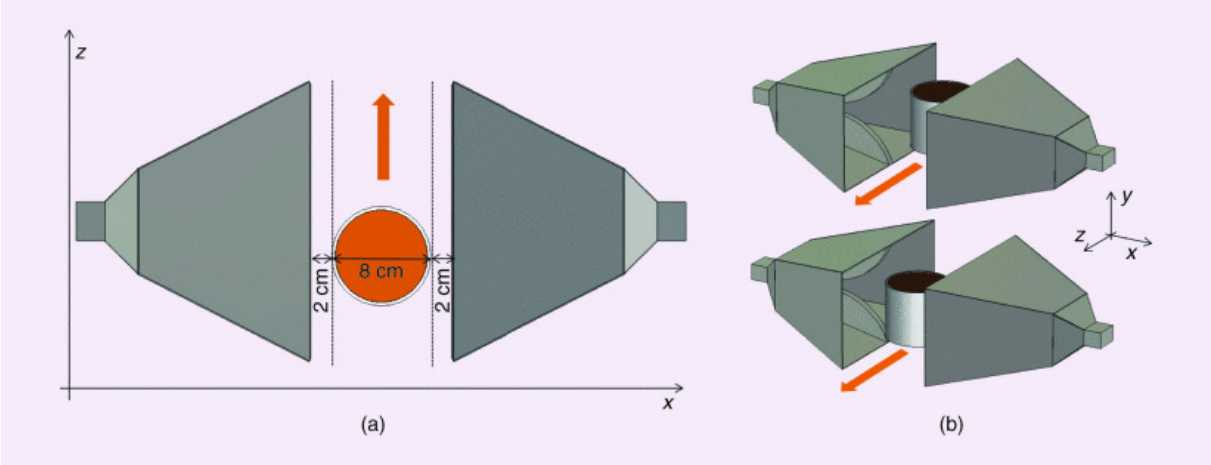

Figure 1.3.7: (a) Simulated 3D scenario in the xz-plane showing geometric dimensions, and (b) a 3D view at various time instants [65] .

The Wavision Research Group (Dept. of Electronics and Telecommunications, Politeccnico di Torino, Torino, Italy) has been actively engaged over the past few years in exploring the use of MWI in the food industry. In [65], the principle of MWI, as discussed in the subsection on microwave imaging principles, was applied to packaged food samples containing hazelnut-cocoa cream. The setup presented in Figure 1.3.6 shows two wideband horn antennas positioned opposite each other, with a jar of hazelnut-cocoa cream placed at the center between them. The two antennas illuminate the jar sample and are connected to a vector network analyzer (VNA), which sequentially records measurements of the (2×2) scattering matrix. As the jar is moving, the author assumed the setup to be equivalent to an array of antennas positioned on both sides of the line with the food product stationary in the center, as illustrated in Figure 1.3.6(b), where the virtual antennas are represented by gray dots. The speed of the conveyor belt and the VNA measurement time determine the number of (2×2) scattering matrices captured during each data acquisition. In this study, the (2×2) scattering matrices are recorded at 13 positions, represented by the gray dots in Figure 1.3.6(b). The choice of the working frequency range is strongly dependent on the dielectric properties of the food and the size of the used jar (8 cm for the long diameter). Taking all parameters into account, the authors chose an operating frequency of 10 GHz, with a spatial resolution equal to $\lambda_c/4 = 4$ mm at this frequency, where λ_c represents the wavelength of the propagating microwave within the hazelnut cocoa creme. Notably, the spatial resolution should be comparable to the contaminant size used in this study (5 mm in radius), indicating the system's ability to detect the contaminant within the medium.

Figure 1.3.7 presents a simulated scenario that shows the jar's movement between the two horn antennas (as if it is carried by a conveyor belt) and highlights the various positions where data are recorded. The SVD truncation index T was selected based on the distribution of singular values with an assumed Signal-to-Noise Ratio (SNR) of 70 dB. To keep a sufficient number of right singular vectors $[\mathbf{v}_n]$ for accurately reconstructing the contrast variation $\Delta\chi$ a noise threshold of –30 dB was set, that corresponds to T = 82. The reconstructed images from the simulation data are presented in Figure 1.3.8 in 3D views. The reported results are simulated at 10 GHz. The reference scenario is presented in the first column, where the small yellow spots indicate the location of the contaminant across different plane views. The contaminant included in these simulations is a metallic sphere with a radius of 5 mm. The

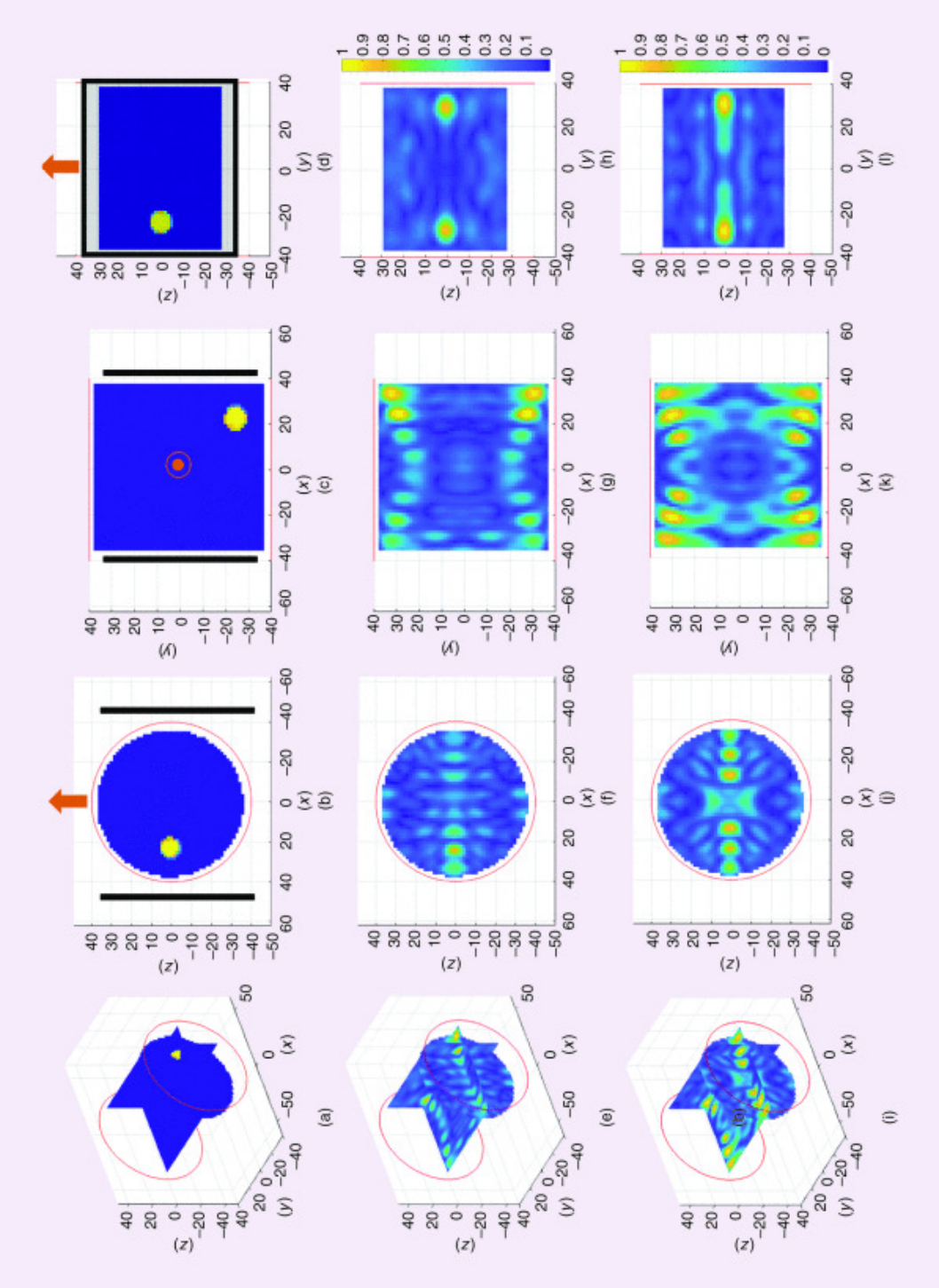

Figure 1.3.8: Simulation results [65]: (a)–(d) 3D permittivity contrast in the reference scenario. (e)–(h) Reconstructed tomographic images using both monostatic and bistatic data. (i)–(l) Reconstructed images using bistatic data only. The columns correspond to a different view, with black lines indicating the two horn antennas and orange arrows showing the jar's movement direction. the axes unit is millimeters.

orange arrow shows the movement direction of the jar (along the **Z** axis). The second column, images (e-h), displays the results where both monostatic and bistatic data are used in the imaging reconstruction,

whereas the third column includes the results when only bistatic data are considered. In the xz-plane (f), the contaminant was detected with minor replicas along the x-axis. In the yz-plane (h), the synthetic aperture enabled correct z-axis imaging, but limited y-axis measurements caused specular artifacts. The xy-plane image (g) showed combined artifacts due to non-uniform antenna radiation patterns. The third column of Figure 1.3.8 shows the 3d images reconstruction using only bistatic data, excluding self-terms ($\Delta S_{(p,p)}$ and $\Delta S_{(q,q)}$). The contaminant was still identified, but the reconstructions appeared fully symmetrical relative to the yz-plane between the antennas. This symmetry arises because bistatic measurements produce identical transmitter–target–receiver paths by reciprocity, whereas monostatic data provide side-specific information on the contaminant's location in the jar.

Figure 1.3.9: System configuration for simulating movement [65]: (a) the whole setup and (b) the two antennas positioned near the jar.

In discussing the measurements, the author presents a scenario similar to the previously discussed simulation. Figure 1.3.9 displays the two horn antennas and the test jar centered in between. Measurements were recorded at 13 different positions and manually adjusted in the same manner as in the previously described simulation. The measurements were conducted within an anechoic chamber to minimize external interference and the data was recorded at 10 GHz. The jar was positioned in 13 different positions to simulate real-case sampling. The contaminant, as in the simulations, was a metallic sphere with a 5 mm radius.

The image reconstruction results derived from the measurements are shown in Figure 1.3.10. Similar to the simulation results, the first column indicates the expected position of the contaminant within the jar, which remains undetectable by eye due to the opaque chocolate filling. The second column displays the reconstructed images derived only from the bistatic data, with monostatic data excluded to avoid potential inaccuracies in reconstruction, as the antennas used are not identical. Similar to what obtained from the synthetic data, the contaminant was detected, with some replicas along the x-axis. Additionally, the reconstruction results were fully symmetrical relative to the yz-plane, as only bistatic data were used for measurement. The final column of Figure 1.3.10 displays 3D tomographic reconstructions from the difference between scattering parameters measured with uncontaminated jars. These images, normalized to the maximum reconstructed values with contaminants, show noticeably lower values in the uncontaminated scenario. This test is crucial in industrial applications to minimize false positives.

To summarize, this paper [65] is the first to explore an MWI technique for detecting physical contamination in food packaging. The study provides a proof-of-concept with areas for improvement. Enhancements include automating synchronization between measurements and jar movement on the conveyor belt,

which would allow for more accurate metrics and practical imaging algorithms.

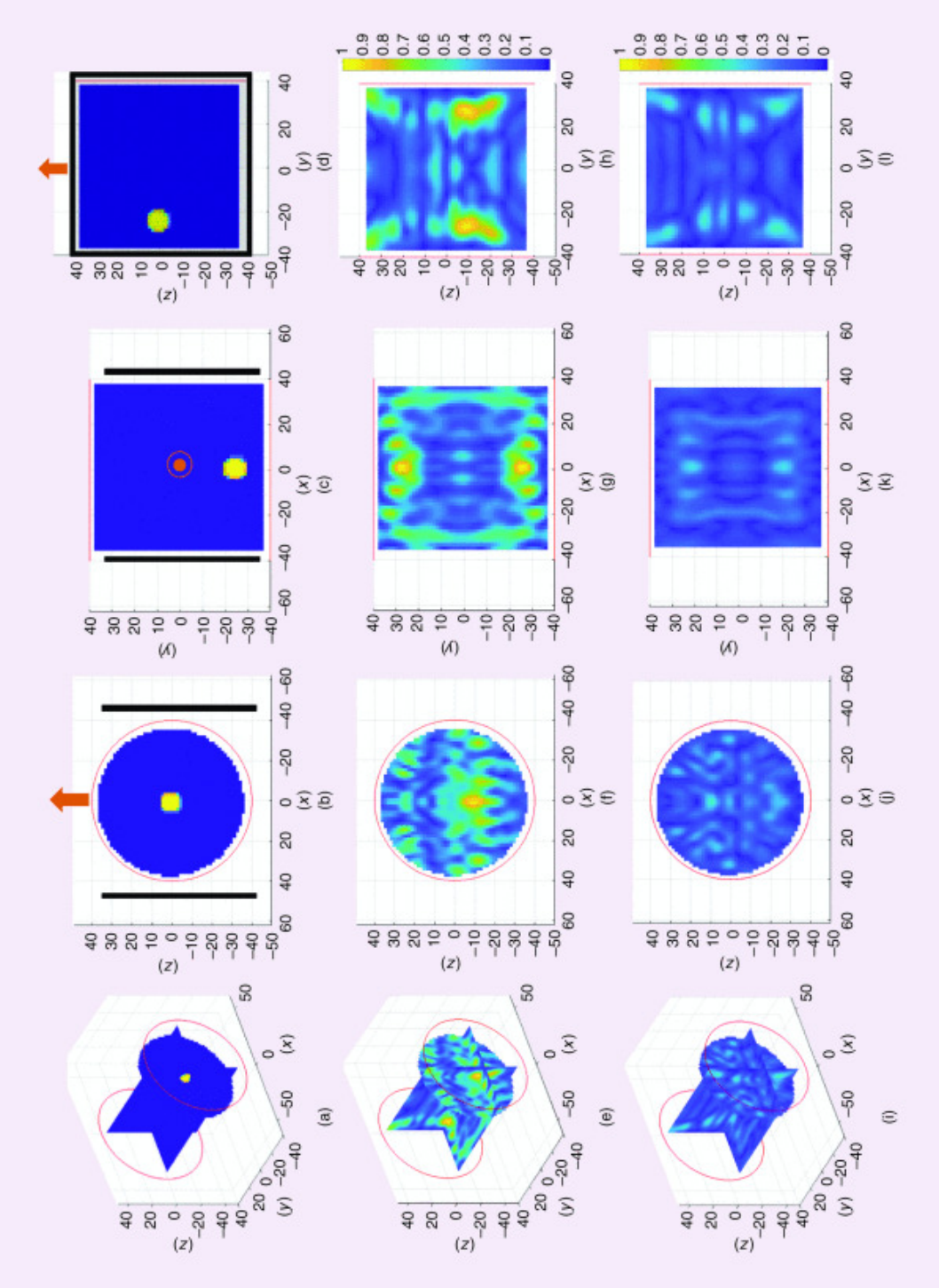

Figure 1.3.10: Measurement data results [65]: (a)–(d) depict the 3D reference scenario, (e)–(h) show the reconstructed tomographic images using bistatic data alone, and (i)–(l) display the images obtained by subtracting two sets of data acquired with uncontaminated jars. Each column represents a different perspective, with black markers indicating the two horn antennas and orange arrows illustrating the jar's movement. All dimensions are in millimeters.

Case study: 2

Similar approaches were introduced by another group in [79, 80], where MWI techniques were applied using the same steps outlined above to solve the inverse problem via TSVD, with enhancements achieved by exploiting the symmetry properties of the food package geometry under test. In [79], the authors employed a system similar to that introduced in [65]. This system used two horn antennas positioned with the food package centered between them. Considering the motion of the food jar, the setup effectively creates an equivalent configuration of multiple synthetic antenna pairs radiating the jar as shown in Figure 1.3.11

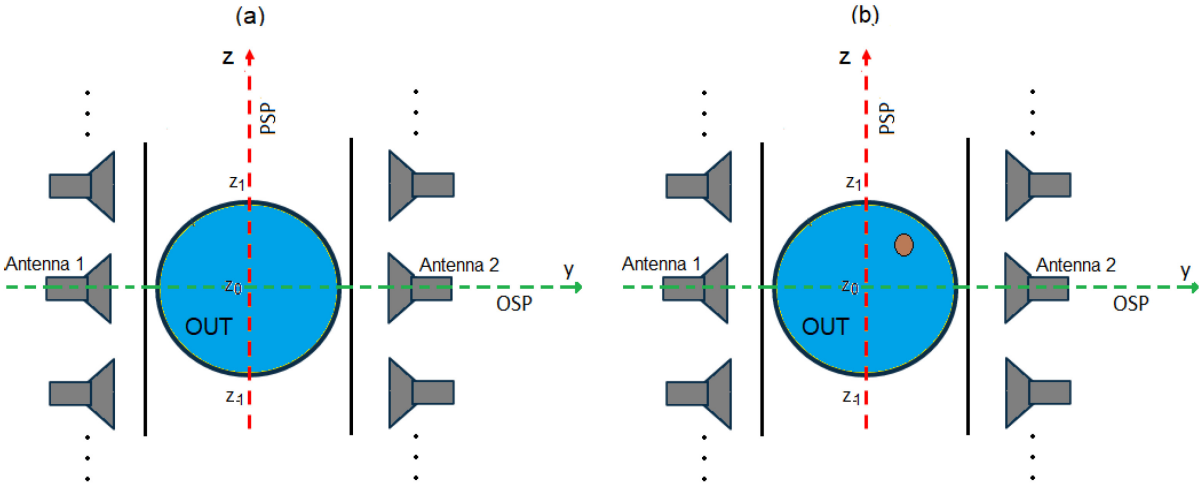

Figure 1.3.11: Symmetries exploited in the proposed detection and imaging methods [79]: (a) OUT without inclusions, maintaining symmetry; (b) OUT with an inclusion, causing a disruption in symmetry.

The scope of the work in [79] focuses on homogeneous food packaged in circular non-metallic jars. It introduces two symmetry-based approaches: the Parallel Symmetry Plane (PSP)-Based approach, which identifies changes in the reflection coefficients (S_{ii}, with i = 1, 2) between two antennas when the PSP-plane (the xz-plane in Figure 1.3.11) dividing the jar into two symmetric halves along its movement direction—is disrupted by an inclusion; and the Orthogonal Symmetry Plane (OSP)-Based approach, which detects variations in all scattering parameters caused by the breaking of symmetry with respect to the OSP-plane (the xy-plane in Figure 1.3.11) perpendicular to the movement direction that divides each antenna into symmetric parts. These techniques effectively detect foreign inclusions in food packages by exploiting symmetry disruptions. In both approaches, the reconstruction of intrusion images is achieved by solving Equation 1.3.6. For the PSP-based approach, this involves $\Delta S_{ii} = S_{ii}(z_n) - S_{jj}(z_n)$ (i = 1, 2 and j = 2, 1), where z_n represents the n-th measurement position along the z-direction. However, for the OSP-based approach, the difference in the scattering matrices is calculated as $\Delta S_{ij} = S_{ij}(z_n) - S_{ij}(z_{-n})$, where the scattering matrices are obtained from each pair of antennas and their mirror pairs at z_{-n} with respect to the xy-plane. The effectiveness of the two approaches depends on the position of the contaminant within the food jar. The OSP-based approach fails when the intrusion lies on or very close to the xy-plane, while the PSP-based approach encounters limitations when the inclusion is located on or near the xz-plane.

The simulated scenario illustrated in Figure 1.3.12 demonstrates the use of two WR-187 horn antennas operating within the frequency range of 4.0 to 5.8 GHz, sampled at 11 discrete frequency points. The

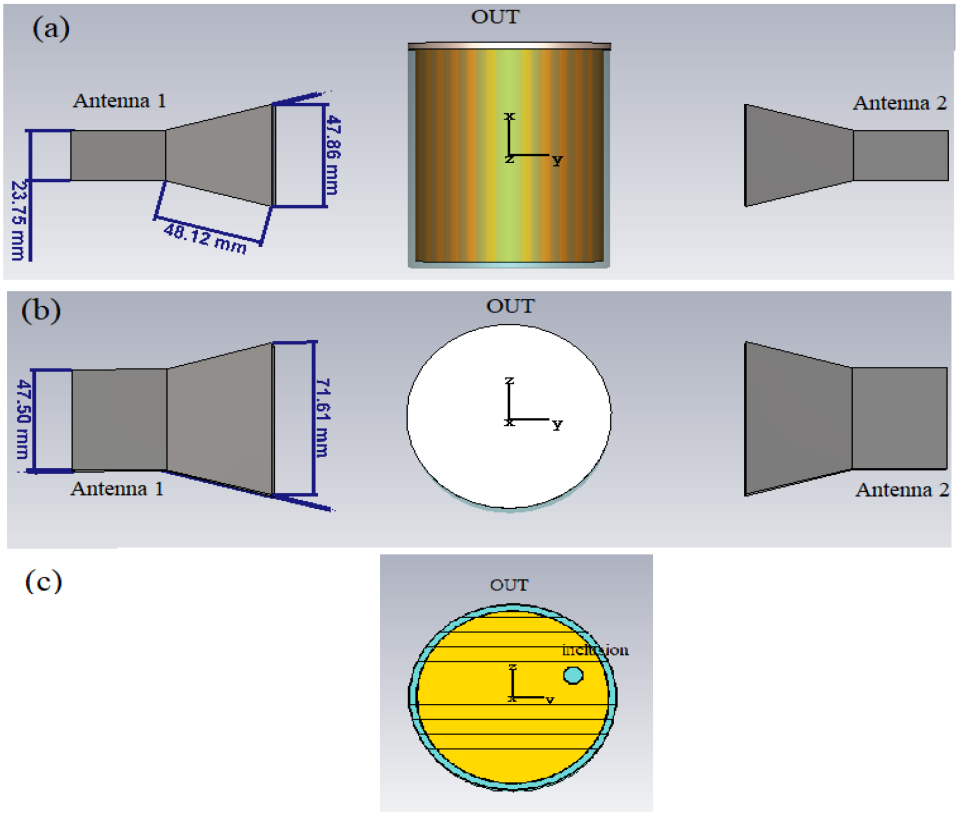

Figure 1.3.12: Numerical setup used in the simulations [79]: (a) front view, (b) top view, and (c) cross-sectional view of the OUT.

positions are defined along $z_n = -6$ to $z_n = 6$, with a step size of $\Delta z = 1$ cm ($n = -6, \ldots, 6$, resulting in a total of N = 13 positions). The jar is filled with a homogeneous medium having a complex relative permittivity of $\epsilon_r = 3 - j0.42$, typical for oil-based food products like hazelnut-cocoa cream. A small glass inclusion ($\epsilon_r = 6$) with a diameter of 8 mm is placed at the position shown in Figure 1.3.12(c) with the small blue circle.

Figure 1.3.13 presents the outcomes of three different scenarios: Figure 1.3.13(i) for the PSP-based approach, Figure 1.3.13(ii) for the OSP-based approach, and Figure 1.3.13(iii) for the combined application of both approaches. A satisfactory reconstruction is achieved when implementing the two approaches separately, as illustrated in Figure 1.3.13(i) and Figure 1.3.13(ii). However, two distinct spots are evident: the first corresponds to the inclusion's actual position, representing the inclusion itself, while the second is its mirrored with respect to the xz-plane in Figure 1.3.13(i) and the xy-plane in Figure 1.3.13(ii). Although the PSP-based and OSP-based approaches can operate independently, their combination offers significant advantages as shown in Figure 1.3.13(iii). It effectively eliminates "the mirrored spot" thereby resolving ambiguities caused by symmetrization, and minimizes the risk of failure when the inclusion is located along their respective symmetry planes.

The work presented in [79] is a numerical study, but it provides promising evidence that MWI can serve as a powerful technique for detecting physical contaminants in food packages. However, the Symmetry-Based Microwave Imaging approach adopted by the authors imposes certain limitations. These include the requirement for symmetry in the geometry of the jar and antennas with respect to the

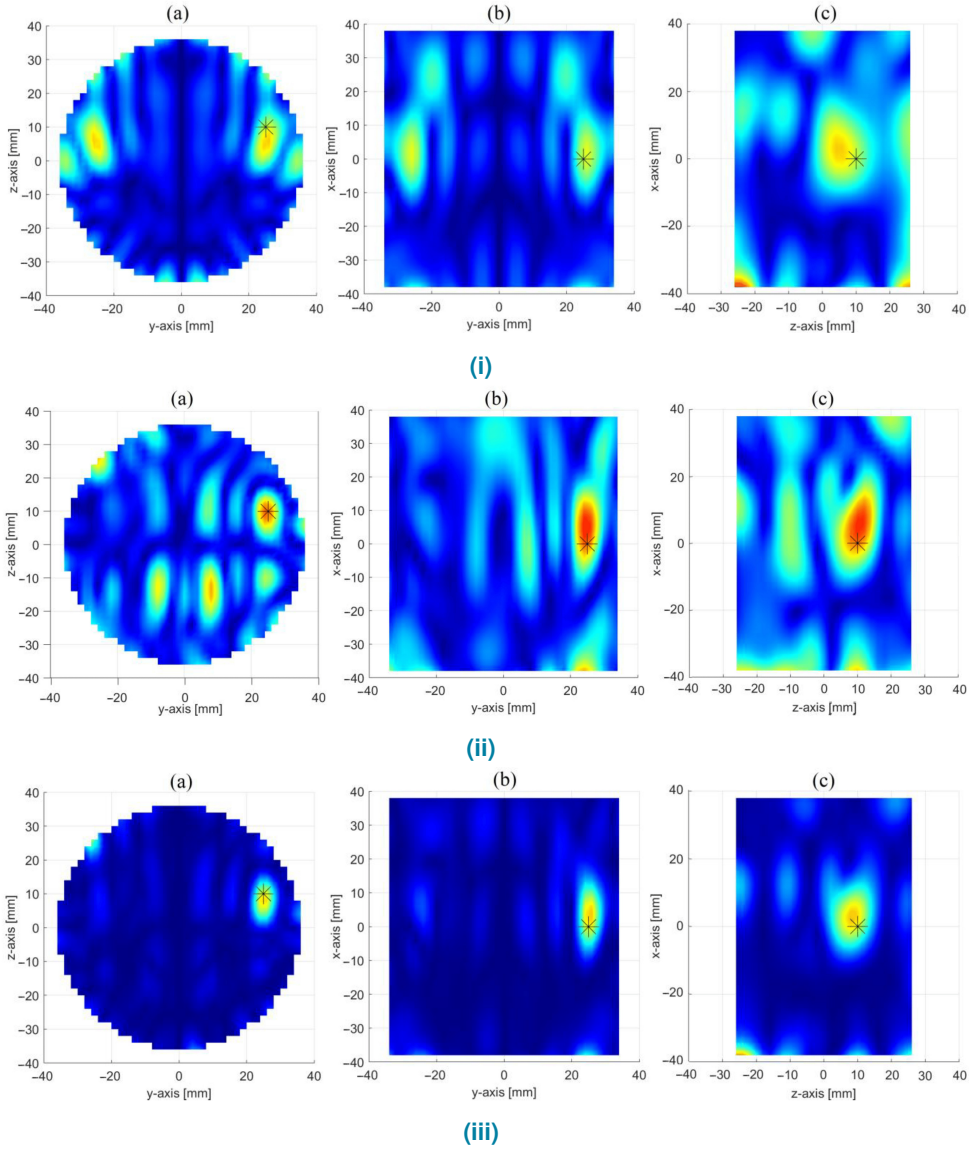

Figure 1.3.13: Reconstruction of the dielectric constant using different approaches [79]: (i) PSP-based approach, (ii)) OSP-based approach, and (iii) combined PSP and OSP approaches. Images are shown in three orthogonal planes crossing the inclusion center.

two discussed planes, the homogeneity of the food medium, and constraints related to the position and size of the contaminant within the jar.

Case study: 3

Building on the work in [79], the same research group developed a preliminary proof of concept involving an MWI system that employs two circularly loaded antipodal Vivaldi antennas (CLAVAs) to detect contaminants in packaged food items using the Symmetry-Based (SB) MWI approach [80]. The antennas must be wideband to probe the object under test (OUT) response at diverse frequencies, ensuring sufficient frequency diversity for reliable imaging. Ultrawideband (UWB) antennas are preferable to achieve high imaging resolution across a variety of food types, from oil-based to high water-content

products, by utilizing different frequency sub-bands. The selection of CLAVAs in [80] proves advantageous due to several factors: their ultra-wideband operation spanning 1 to 15 GHz, compact size, and symmetric shape, which maintains the validity of the SB MWI approach utilized in this study.

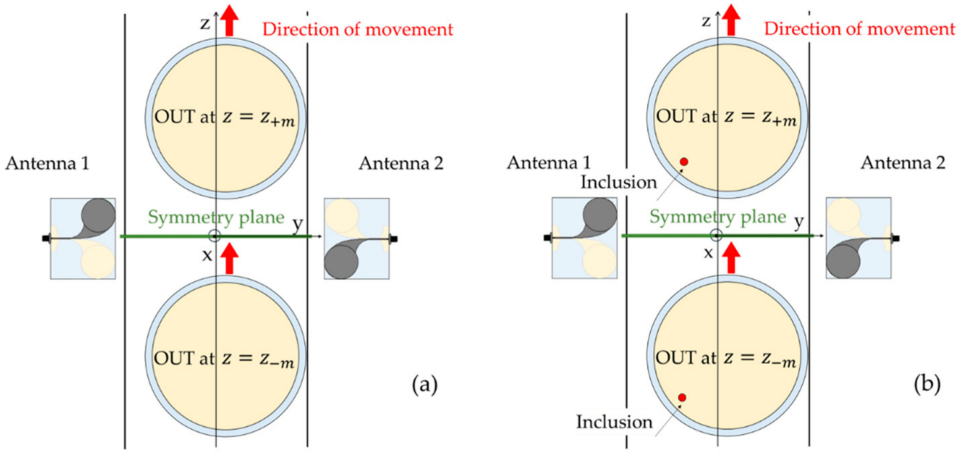

Figure 1.3.14: Illustration of the system's symmetry properties [80]: (a) The system exhibits symmetry with respect to the xy-plane, where the OUT at position z_{-m} is a mirror image of the system at position z_{+m}. (b) The inclusion disrupts this symmetry.

The simulation and measurement setups for the new system are depicted in Figures 1.3.14 and 1.3.15, respectively. The simulation scenario is similar to that presented in [79], with the horn antennas replaced by CLAVA ones. The authors continued testing food jars containing hazelnut-cocoa cream and using the same intrusion materials, but this time operating within the 4 to 7 GHz range, with a step size of 0.25 GHz. The results are compared between SB approach that introduced in [79] and the Reference-Based approach (RB) as the one introduced in [65].

Figure 1.3.16 shows the images reconstruction obtained in [80]. From panels (a)–(c) obtained from the SB approach, it is evident that, in the absence of the inclusion, the maps appear mostly uniform, with weak spots likely caused by slight errors in manually positioning the jar. Panels (d)–(f) reveal well-defined and localized spots using the RB approach, clearly indicating the presence of the inclusion. These spots include one at the actual position (highlighted by the red dashed circles in Figure 1.3.16) and three additional ones at symmetrical positions relative to the planes y = 0 and z = 0. Finally, panels (g)–(i) present the images obtained using the RB approach, showing good consistency with those produced by the SB approach. The RB approach accurately identifies a spot at the exact location of the inclusion, along with a less intense spot at the symmetrical position relative to the y-axis (attributable to reciprocity). The primary spot aligns perfectly with one of those observed in panels (d)–(f).

Case study: 4

Away from packaged food products, the agricultural application presented in [81] investigates the use of Frequency Modulated Continuous Wave (FMCW) radar to detect and remotely estimate the intra parcel quantity of grapes. The system shown in Figure 1.3.17 consists of a horn lens antenna, an FMCW radar, a patch array antenna, and a mechanical platform for scanning purposes. The transmission is performed through the horn lens antenna (Tx antenna) with a 28 dBi gain and a 6° beamwidth. Backscattered

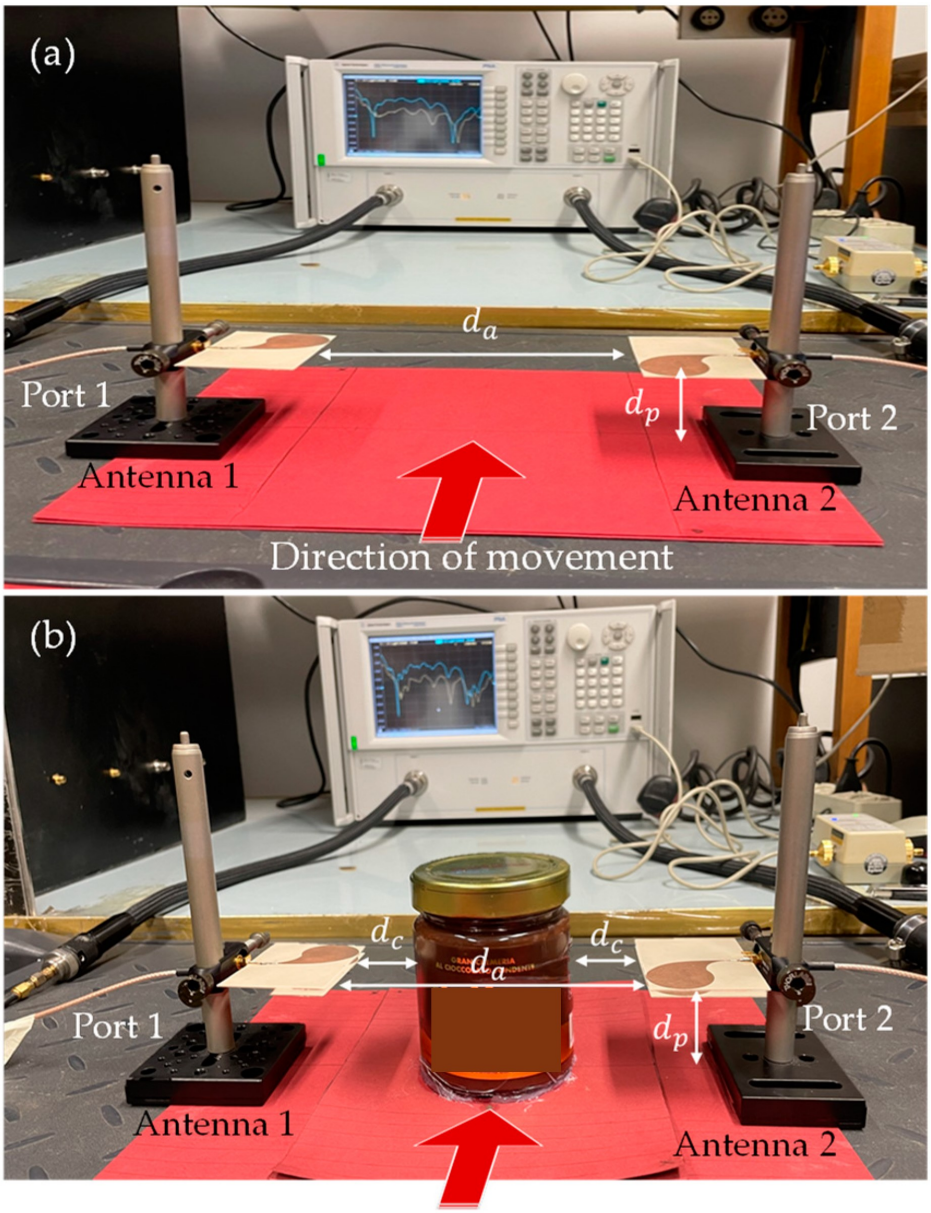

Figure 1.3.15: Experimental setup [80]: (a) Two CLAVAs positioned facing each other without the OUT. (b) The OUT placed between the antennas. The red arrow denotes the direction of the OUT's movement.

electromagnetic waves from the grapevines are captured by a 1 $\times$ 5 patch array antenna (Rx antenna) that offers a gain of 8.6 dBi, with a beamwidth of 60° in the azimuthal plane and 25° in the elevation plane.

The system enables the rotation of the Tx and Rx radar antennas with an accuracy of 1° in azimuth (θ) and elevation (ϕ). This rotational capability facilitates mechanical scanning of the radar beam, allowing for the derivation of a 3D representation of the grapevine echo level distribution. The ground-based microwave FMCW radar moves between the rows of grapevines. Beam scanning is conducted in front of each plant at a distance of 1 m, covering angles of $\pm$30° in azimuth and –10° to 30° in elevation. As an illustration, the cross-sectional view of the obtained radar image is shown in Figure 1.3.18. The grapevine rows are easily detectable in this image due to their specific geometric and physical properties.

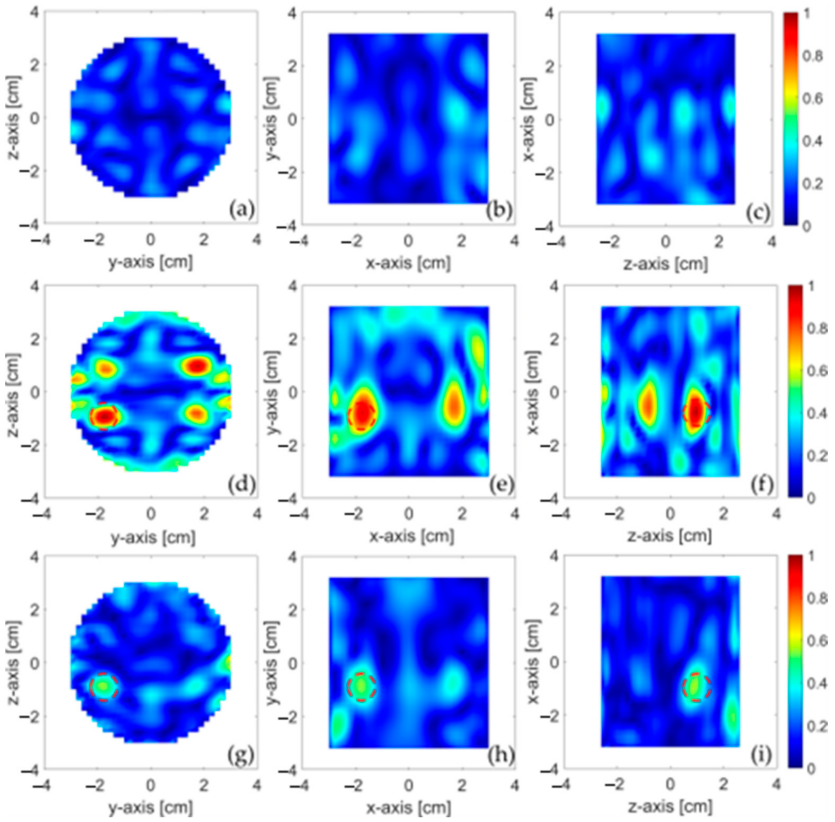

Figure 1.3.16: Reconstruction of the intrusion displayed in three orthogonal cut planes passing through its center [80]: (a–c) SB approach applied to the OUT without the intrusion; (d–f) SB approach applied to the OUT with the intrusion; (g–i) RB approach applied to the OUT with the intrusion. The dashed circles in the panels indicate the inclusion's position.

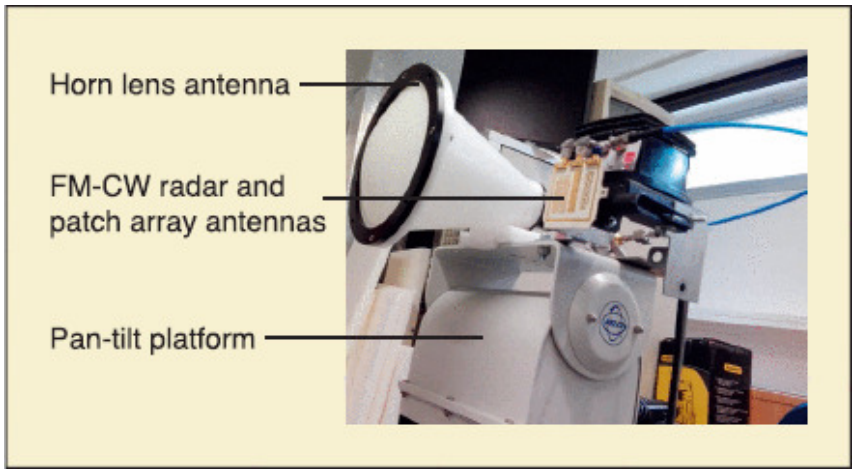

Figure 1.3.17: Ground-based microwave FMCW radar [81].

To estimate the grape quantity, electromagnetic echo levels are recorded at distances ranging from 0.5 m to 1.5 m in front of different grapevine plants. For a constant volumetric mass density of grapes, the grape volume increases linearly with both mass and water content. Therefore, the volume of grapes on a plant can be estimated by measuring the echo level produced by the water content in the grapes.

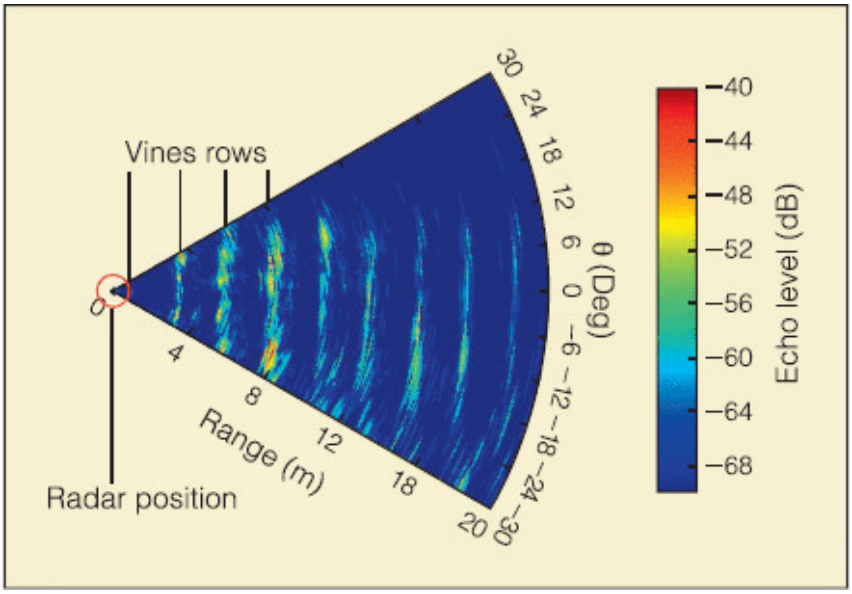

Figure 1.3.18: A two-dimensional polar plot illustrating the electromagnetic echoes from the vineyard (cut-plane $\phi = 0°$). The high echo levels enable the identification of the vine row locations [81].

These plants are composed of leaves, grapes, and wood. The water within the grapes and leaves has a relative permittivity (ϵ_r) of about 30 at 24 GHz, leading to a strong reflection of the incident microwave field. Inorganic objects (such as iron wires or irrigation pipes) also produce significant echoes. A contour detection-based algorithm is applied to the 3D radar image, and a new parameter, called the spreading factor, is defined to classify the grape echo levels. The total quantity of grapes is calculated from measurements using an appropriate estimator. This microwave-based remote sensing approach provides a solution for estimating the grape quantity, even when they are hidden by leaves.

1.3.4 Machine Learning-Assisted Microwave Sensing in the Food Industry

The aforementioned applications of MWI approaches to detect physical contaminants in food packaging have demonstrated promising potential. These systems rely on solving inverse problems to identify contaminants. However, their practical implementation in real-world scenarios remains limited by several factors, such as the speed of conveyor belts, the automated movement of food jars along the belt, noise levels, the size and material of the contaminant, and the homogeneity of the food medium. For example, in most existing studies, manual positioning of jars along predefined points was used, which does not reflect the complexities of a real production environment.

In addition, the analysis of the data generated by microwave inspection systems in the food industry is often complex, time-intensive, and requires highly skilled operators. In this context, ML techniques have emerged as valuable tools in the food industry. For instance, instead of addressing the inverse problem by regularizing the non-linearity of data, which is highly sensitive to noise, ML tools can overcome these challenges through a statistical approach that utilizes the scattered data to accurately determine the presence or absence of contaminants.

Real-time quality control in the food industry demands an innovative approach that combines microwave sensing with ML tools to enable fast data processing and continuous operation. Integrating ML can

bridge the gap between the high-speed requirements of production lines and the complex computational demands of microwave sensing systems [82, 83]. This hybrid approach has already proven effective in various applications, including remote sensing [84], ground-penetrating radar (GPR) [85], water pollutant detection [86, 87], material identification [88], and medical applications [89–93].

The implementation of Artificial Intelligence (AI) in food inspection emerged with image processing, vision-based techniques [94–96], Hyperspectral Imaging (HSI) systems [97] and NIR imaging systems [98]. In the next subsection level, we present some of the studies that integrate different food inspection systems with AI tools, focusing primarily on detecting defects in fruits for agricultural production purposes.

Case study: 1

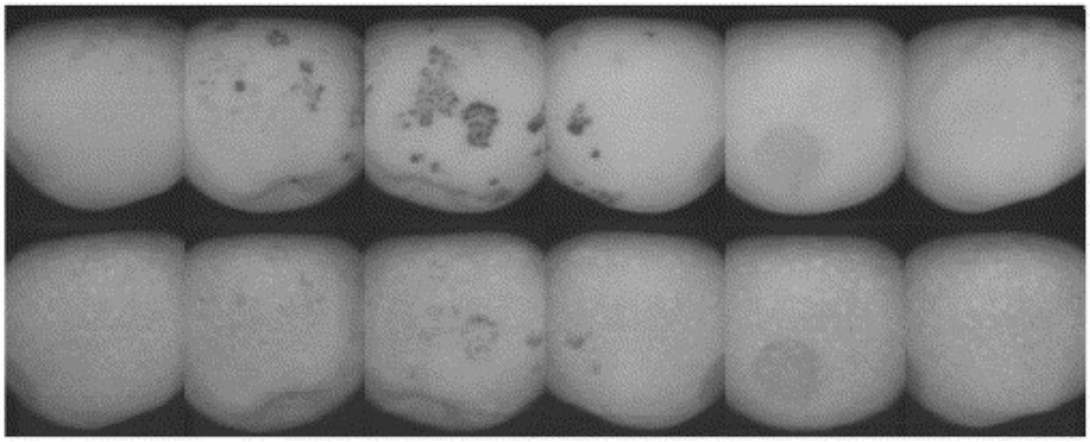

Figure 1.3.19: Images captured for different apples using two filters: the upper row shows six images taken with a 740 nm filter, and the lower row displays six images captured with a 950 nm filter [98]

The authors in [98] used an NIR imaging system with a CCD camera in capturing images for different apples using two optical filters at 740 nm and 950 nm as shown in Figure 1.3.19. The approach in this study focuses on classifying images based on their overall appearance, which involve defects identification through segmentation as shown in Figure 1.3.20. Sets of images representing different classes are organized into a matrix, where each image is treated as a sample, and its pixel values serve as variables. Principal Component Analysis (PCA) is then applied to this data matrix for dimensionality reduction. The most significant principal components are subsequently used to train a neural network for classification.

A combination of three threshold-based segmentation techniques and an artificial neural network utilizing principal components was used to detect the defects and to classify the apples. The study quantitatively evaluated the system's performance in both orientation verification and integration of the segmentation methods, testing it across eight apple varieties. The classification and defect detection accuracy achieved with this approach ranged from 78% to 92.7%.

Case study: 2

In [96] the authors presented a computer vision-based approach for segmentation aimed at identifying defects in various fruits (e.g., apples, bananas) and vegetables (e.g., potatoes, tomatoes). The methodology proposed in [96], illustrated in Figure 1.3.21, starts with imaging using a digital camera.

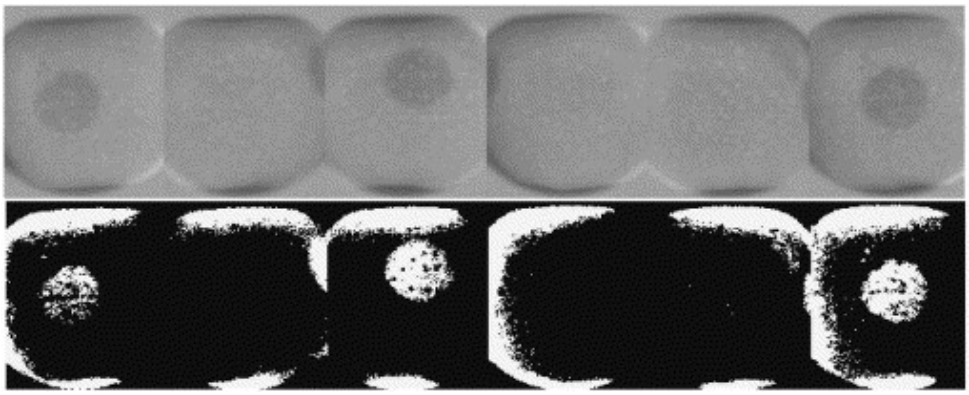

Figure 1.3.20: Top: images of apples captured with a 950 nm filter; Bottom: the same image after applying threshold segmentation [98].

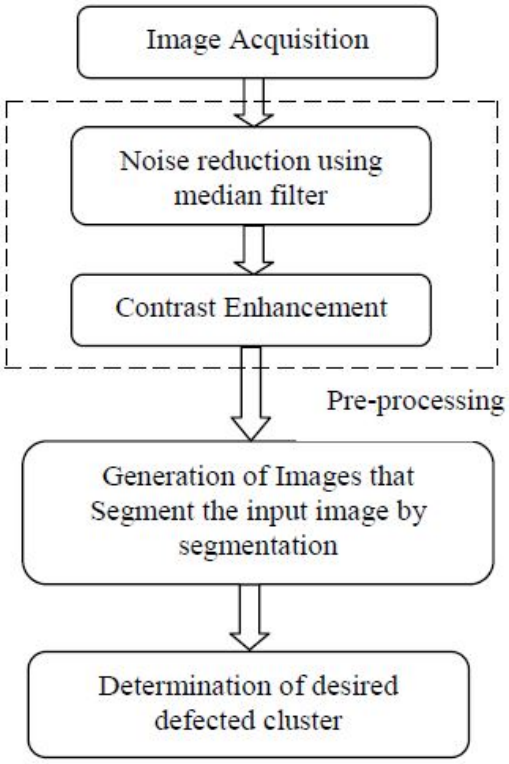

Figure 1.3.21: The workflow [96].

This is followed by preprocessing steps to remove noise that may arise during image acquisition and to enhance image contrast. Finally, segmentation is performed to detect the defective regions in the tested fruit samples.

In Figure 1.3.22 we present an example of the results obtained by the authors in [96], demonstrating the application of digital imaging and segmentation applied to a partially defected apple. Applying the Otsu segmentation method to the RGB image enabled the extraction of the defective region, as shown in Figure 1.3.22, resulting in the efficient identification of unhealthy apples. This approach is effective for detecting defects on the outer surface of fruits and vegetables, as shown in Figure 1.3.22, because it

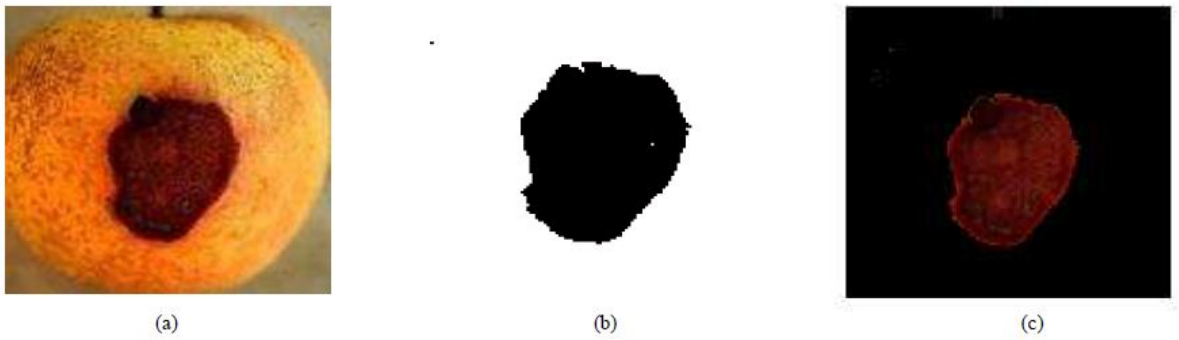

Figure 1.3.22: Experimental results of segmentation using the Otsu method [96]: (a) Input RGB image of a disease-affected apple; (b) Grayscale image obtained after applying the Otsu segmentation method; (c) Output image highlighting defective regions after restoring the color information from the input image.

relies on digital imaging that captures the surface of the object. However, it is not suitable for detecting internal defects within the samples, as it does not collect images or provide information about their internal structure.

Case study: 3

The promising results from studies integrating various inspection systems with machine learning (ML) tools in the agriculture industry, as discussed in [96, 98], along with the limitations of these systems discussed earlier in this chapter, have motivated researchers to explore combining ML classification methods with microwave and millimeter-wave (mmW) imaging and sensing technologies in food safety. Researchers and scientists are particularly interested in mmW measurements for several reasons: mmW systems offer higher spatial resolution compared to microwaves, their antennas are more compact, and they provide very high bandwidths, enabling faster data transmission rates. In this context, detecting defects in food and fruit extends beyond the microwave spectrum to the millimeter wave (mmW) spectrum (30 to 300,GHz). Our team at the LEAT Laboratory in France is actively engaged in applying millimeter-wave (mmW) imaging to a range of civil applications, including aviation safety [99], Foreign Object Debris (FOD) detection [100, 101], health monitoring [102], and more recently, food safety and fruit quality inspection [103–105].

In [103–105], the authors introduced a mmW imaging system as shown in Figure 1.3.23 for detecting defects in fruits such as apples and peaches. A monostatic measurement configuration was chosen for several reasons: it is compact, cost-effective, and well-suited for fruits like apples and peaches, which have high water content. The high absorption characteristics of water-rich fruits make it unlikely for the mmW waves to penetrate through. The approach began with spatial scanning of apple samples using a mmW imaging system (Figure 1.3.23). The scanning covered different angles of incidence, recorded data at different frequencies (92, 94, and 96 GHz), and accounted for polarization. A two-dimensional fast Fourier transform (2D-FFT) was then applied to generate images, followed by the use of a ML classifier to distinguish between healthy and spoiled fruits. The workflow of this approach can be summarized in Figure 1.3.24.

The full scanning area as illustrated by the green line in Figure 1.3.25 is $30° \times 30°$ in θ and ϕ with a step of $0.2°$, centered on the apple. The scanning is performed over the surface of a hemisphere, maintaining a

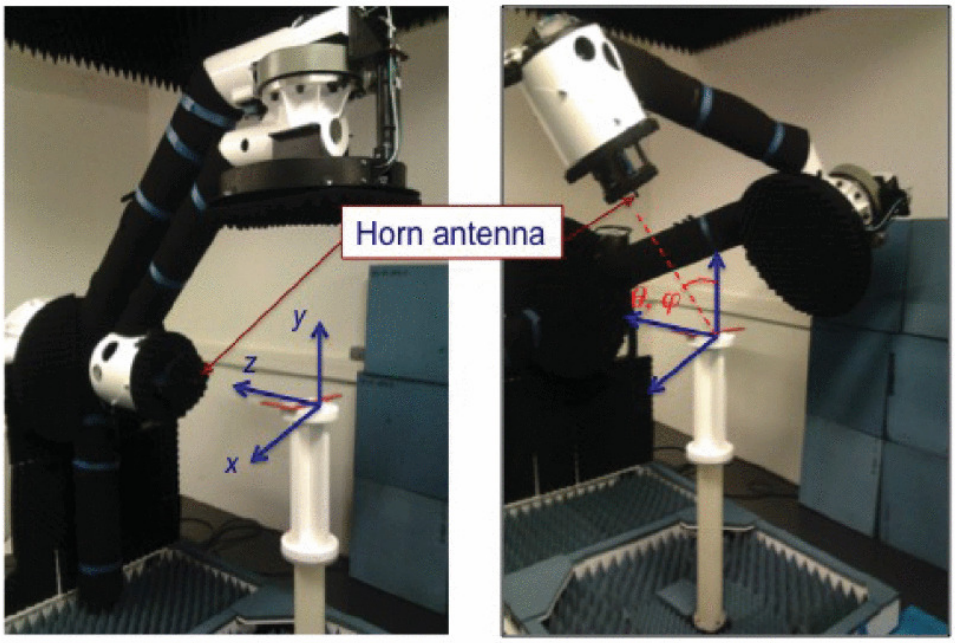

Figure 1.3.23: The measurement system [104]

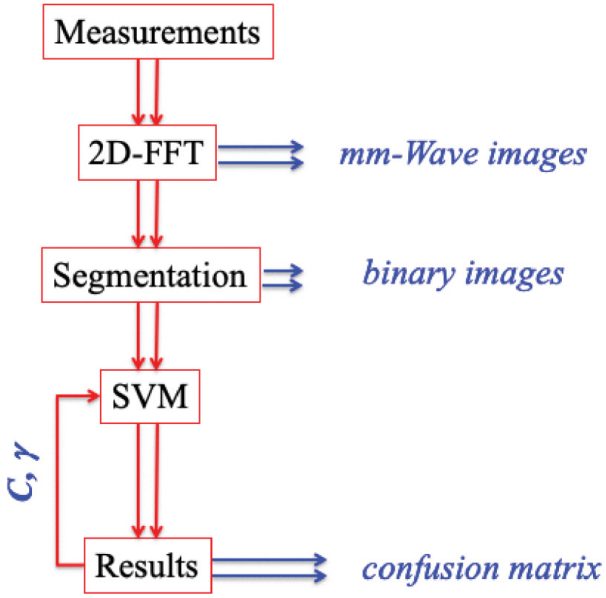

Figure 1.3.24: The workflow [104]

constant distance between the horn antenna and the apple under test. The 0.2° step in θ and ϕ produces a 151 $\times$ 151 matrix representing the reflection coefficient S_{11} at each point within the scanning area. The authors divided this matrix into smaller patches along the diagonal of 10° $\times$ 10° (shown as purple areas in Figure 1.3.25), with a scan step of 0.2°. Each patch consists of 51 $\times$ 51 measurement points, resulting in a total of 101 patches for each frequency as shown in 1.3.26. A 2D-FFT is applied to the selected patches to generate the images. Consequently, each apple under test is represented by 101 $\times$ 3 patches corresponding to the three frequencies.

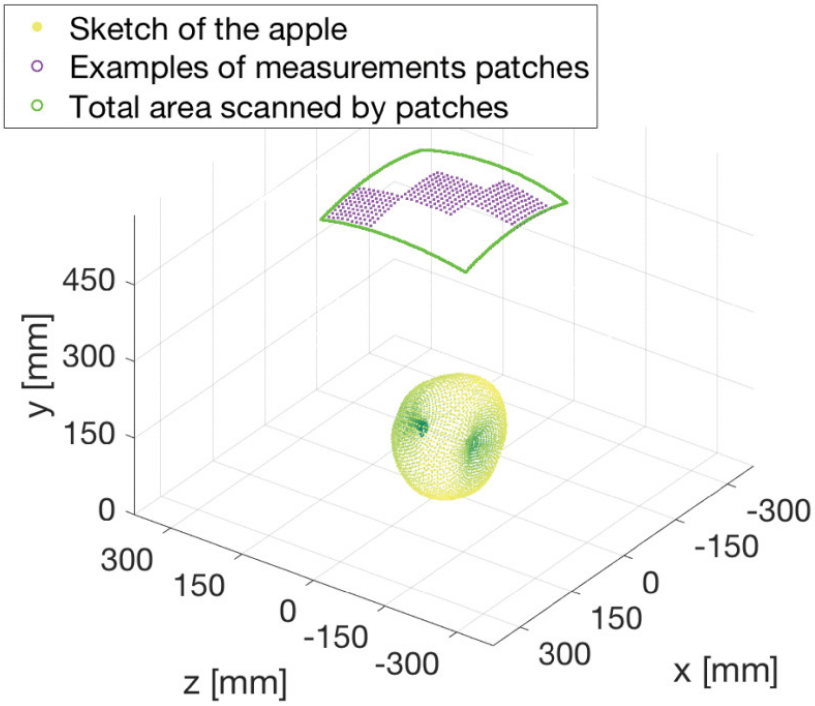

Figure 1.3.25: The scanning area [104]

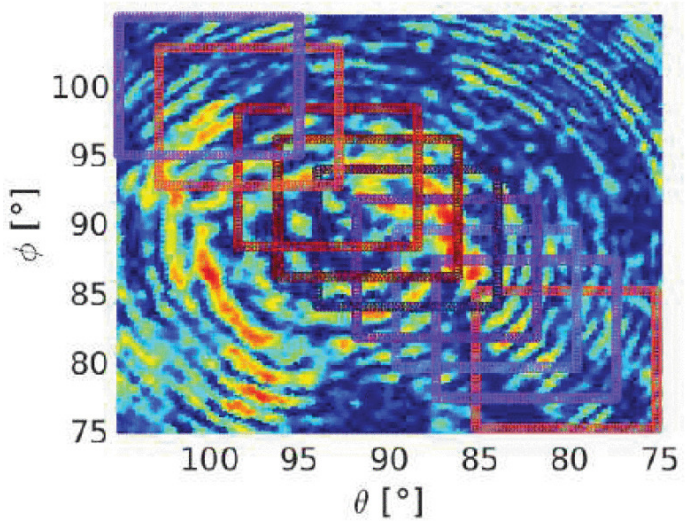

Figure 1.3.26: Plot of the amplitude over the entire scanned area, with squares indicating the patches along the diagonal [105].

After obtaining the 2D-FFT of the patches, image segmentation is performed to convert the images from RGB to binary as shown in Figure 1.3.27. This step is important as it simplifies the data by isolating key features, making it easier to identify and analyze regions of interest, such as defects or patterns, within the images. After segmentation, the authors used non-linear Support Vector Machine (SVM) for the classification stage. To build the database, the authors chose three pairs of Golden apples, categorized by size: large, medium, and small. Each pair consisted of one healthy and one damaged apple of the same

size. The database contains 101 measurement patches per frequency for each of the six apples, resulting in a total of 1818 images. The authors developed a dataset using six apples, allocating four for training and two for testing. This approach resulted in approximately a 67% – 33% split between the training and testing datasets, yielding 1212 training samples and 606 testing samples. The images are categorized into two classes: healthy, labeled as –1 and damaged, labeled as +1. The authors implemented the Grey Wolf Optimization (GWO) algorithm to select the optimal hyperparameters (C^*, γ^*), which are critical for shaping the model's behavior and defining the hyperplane boundaries that separate the different classes. The proposed approach successfully classified healthy and damaged apples by including the diversity in frequencies and the number of measurement points, achieving an accuracy of 80%.

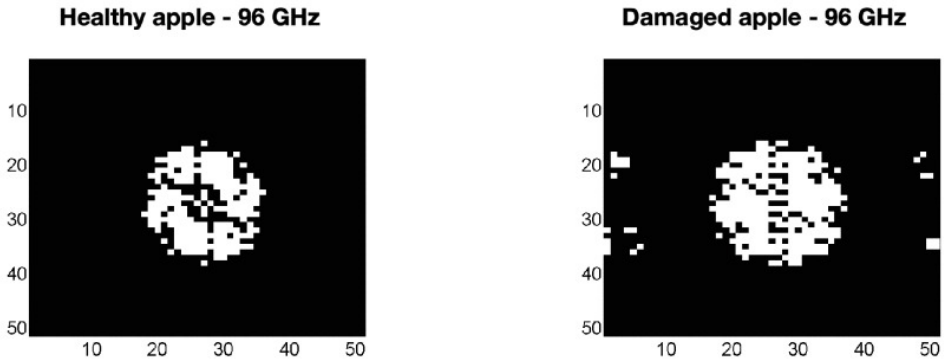

Figure 1.3.27: Segmented images at 96 GHz: Healthy apple (left) and damaged apple (right) [104].

Case study: 4

Recently, a group in Turkey [106] conducted a study combining microwave sensing technology with a neural network to classify walnuts as either healthy or spoiled, utilizing a compact antipodal Vivaldi antenna. The study focuses on analyzing the retrieved scattering parameters directly using a neural network, without applying any preprocessing or solving the inverse problem to the data. The measurements were conducted over a frequency range of 7 to 12 GHz, with a step size of 50 MHz, resulting in a total of 101 frequency points, and at five different walnut positions. The experiment involved 180 walnuts, including 150 from the most recent harvest (assumed to be healthy) and 30 from a three-year-old harvest (assumed to be spoiled). Three sample groups were created from 150 healthy walnuts and 30 rancid walnuts: Healthy unshelled Walnuts (HSW), Glued Unshelled Walnuts (GSW), and Rancid Walnuts (RW). The authors created separate datasets for classification, using reflection coefficients and transmission coefficients independently.

The highest classification accuracy was achieved when the walnuts were placed at the center between the two antennas, with datasets based on either Reflection Coefficients (RCs) or Transmission Coefficients (TCs). Testing with the TCs dataset achieved the highest accuracy of 98.75% in distinguishing between HSW and GSW, and 80.83% in classifying RW and HSW.

Case study: 5

A recent study [107] investigated the classification of liquids for security screening, employing the same mmW imaging system and methodology described in [103]. The measurements covered a frequency

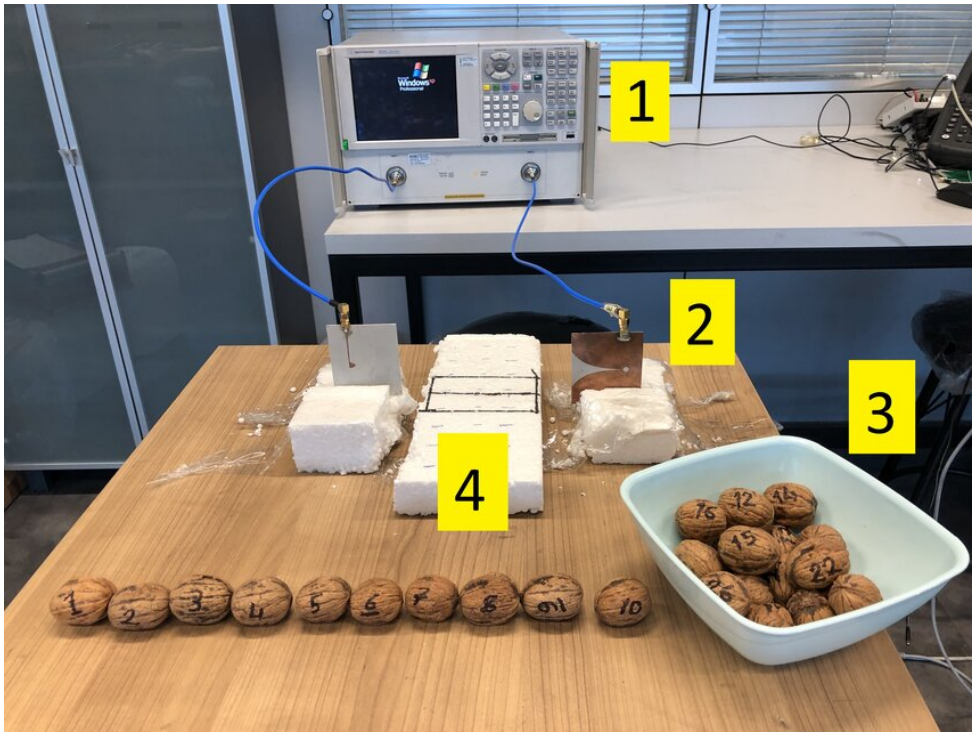

Figure 1.3.28: Experimental setup and walnut samples [106]: (1) N5230A PNA Series Network Analyzer, (2) Vivaldi antennas for transmission and reception, (3) labeled walnut samples, and (4) defined rectangular measurement area.

range from 90 to 100 GHz with 2 GHz intervals. Since testing explosive liquids in the laboratory is both prohibited and illegal, the study focused on a proof of concept using various liquid types, including cola, water, and energy drinks. Two different scenarios were considered: a liquid bottle concealed beneath a jacket and a bottle in direct view. For a more realistic scenario, the measurements included a water bag representing the human body at millimeter-wave frequencies, which was covered with a garment-like fabric, such as a T-shirt. The data was acquired using a 3D spherical scanner [103], which scanned a spatial area of $30^\circ \times 30^\circ$ above the object with a step size of 0.2°. The collected data were processed using a 2D-FFT to reconstruct images for each frequency.

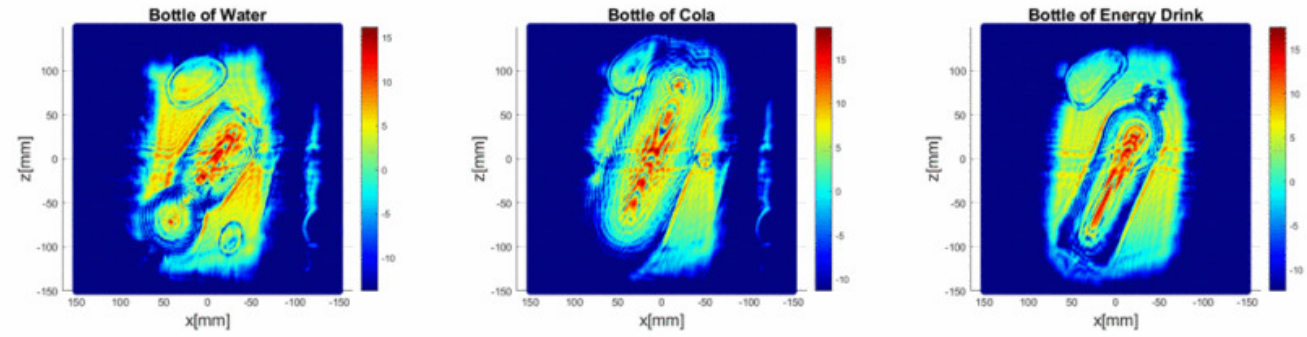

Figure 1.3.29: Images obtained using 2D-FFT for three different liquid samples at 96 GHz [107].

Figure 1.3.29 shows the amplitude of the 2D-FFT results obtained from scanning three different

types of liquid bottles at 96 GHz. The database for the machine learning classification process was constructed using the same methodology as in [103], i.e., the $30^\circ \times 30^\circ$ scanning matrix was segmented into $10^\circ \times 10^\circ$ patches along the diagonal with a scan step of 0.2°. A 2D-FFT was then applied to each patch, resulting in 101 images corresponding to each bottle under test at each single frequency. Using six frequencies ranging from 90 to 100 GHz, a total of 606 images were generated for each bottle in each scenario. The images are then processed further using segmentation with the Otsu method. A total of 3636 images from three bottles were used to construct the dataset for the ML classification. The non-linear SVM algorithm was implemented, and multi-class classification was performed to differentiate between the three distinct classes. The algorithm was trained using data from the scenario where the liquid bottle was directly visible, while the test dataset included measurements where the bottle was concealed beneath a jacket. The GWO is used to determine the optimal hyperparameters for optimal performance, while the implementation of the cross-validation helps in avoiding overfitting. The results were perfect, achieving an accuracy of 100%. Although the primary goal of this study is focused on security applications, its success highlights the potential effectiveness of microwave and mmW inspection techniques for classifying beverages. This approach could be further explored in future studies to detect specific targets, such as contaminants, within beverage products.

1.4 Conclusion

Throughout this chapter, we highlighted the importance of addressing food safety and quality concerns in the food and agriculture industry, particularly focusing on the presence of physical contaminants in food and beverage products and defects in fruits. These challenges not only damage the reputation of companies in the sector but also lead to significant economic losses. We also discussed the advantages and limitations of various existing and emerging techniques implemented to address these issues. The main drawbacks can be summarized as follows: X-ray technology fails to detect low-density materials such as plastic, paper, and wood; metal detector systems are limited to detecting metals; and NIR and THz imaging have limited penetration depth. These limitations are evident in the latest reports on food product recalls, as discussed and presented in Table 1.2.2. This highlights the need to explore more effective techniques to address the limitations of the current technologies.

The microwave non-destructive technique has been proposed as an alternative to these methods due to its advantages, including excellent penetration depth, low-cost equipment, compact systems suitable for integration into production lines, and the ability to handle a wide variety of food and beverage products across its broad spectrum. The application of microwave technology in food and agriculture has followed two distinct approaches: characterizing the complex permittivity of the fruit or food under test using microwave non-destructive techniques, or employing microwave tomography, a type of MWI technique, to reconstruct differences in complex permittivity between the medium under test and an expected target within the medium. Both approaches involve solving the inverse problem. Despite the numerous studies discussed in this chapter on the application of MWI in the food and agriculture industry, there remains a need for more robust and reliable systems. These systems should be capable of achieving the same objectives in less time to suit in-line production processes, while also accommodating various types of contaminants and a wide range of food products.

In this thesis, we build on the principles of MWI and sensing techniques to develop a monitoring system

for detecting physical contaminants in packaged foods and beverages during an in-line process. The system is designed for seamless integration into a production line in the food industry. The scope of this work begins with the theory of electromagnetic wave propagation and scattering at microwave frequencies. It then progresses to the design of the system, including a numerical evaluation of its performance and efficiency. The system is validated through testing on various food and beverage products, following a comprehensive process that spans data analysis and the implementation of ML classification tools, making the detection process suitable for real-time application.

2 Microwave System Design: Requirements and Numerical Assessment

As mentioned in the first chapter, the main objective of this thesis is to develop a microwave sensing system for detecting physical contaminants in food and beverage products. The system must be capable of operating in real-time within an in-line process, ensuring that every product moving along the conveyor belt is inspected using a non-destructive technique. This involves several significant challenges, such as the speed of the conveyor belt, which demands rapid differentiation between contaminated and uncontaminated samples. Additionally, the inspection system must be compact enough to integrate seamlessly with the conveyor belt without interrupting the production process. And finally, the system must also be cost-effective. The movement of the sample on a conveyor belt offers the advantage of collecting data from various angles and positions, enabling a comprehensive examination. However, using a conveyor belt presents challenges, as it requires rapid measurements and fast data processing. Additionally, the microwave sensing system must operate in the near-field region of the antennas, which introduces complexities due to antenna coupling effects, non-uniform field distributions, and calibration difficulties.

This chapter focuses on defining the system requirements. It begins with an analysis of the electromagnetic properties of food products, particularly their dielectric constants. Next, it explores the optimal frequency bandwidth for system operation, taking into account the issue of signal attenuation. Following this, the chapter examines the most suitable types of antennas to cover a wide range of frequencies, enabling the system to handle diverse food materials. Finally, it addresses the optimal arrangement, positioning, and number of antennas for effective system performance. After defining the microwave sensing system, it is crucial to analyze and characterize its near-field performance, as the measurements will be conducted within the radiating near-field region of the antennas. This analysis involves conducting measurements and simulations to evaluate the near-field radiation patterns, the spatial coverage of the electric field within the ROI, and the time-domain reflectometry of the antenna.

2.1 Food from the Perspective of Electromagnetic Waves

Food products and materials are generally considered dielectrics [108]. A dielectric is defined as an electrical insulator medium in which the positive and negative charges within atoms or molecules are bounded by atomic and molecular forces, preventing them from moving freely. When an external electric field is applied to a dielectric, the charges cannot flow because there are no free charges, unlike in the

case of conductors. However, the material can become polarized, with the bound charges slightly shifting their positions, forming electric dipoles. The term "dielectric" refers to materials that exhibit this property of polarization in response to an electric field.

The dielectric properties of food are essential for understanding and modeling their behavior during Radio-Frequency (RF) and microwave processing. Analyzing these properties is critical for understanding how food materials respond in various applications within the food industry, such as microwave heating, radio wave processing, and quality control. The dielectric behavior of foods is influenced by factors including frequency, moisture content, temperature, and composition [109]. Understanding these properties is essential for designing RF and microwave processing equipment, as they determine how energy from RF and microwave fields is stored, transmitted, and dissipated within the material.

2.1.1 Permittivity, Relative Permittivity, and Dielectric Constant

The interaction between electromagnetic radiation and dielectric materials results in energy storage within the material, which is characterized by the permittivity of the material. To understand the physical concept behind permittivity, let's first consider one of the most important conceptual ideas in physics: the speed of light in vacuum. There is a tightly dependent relationship between permittivity (ϵ_0), permeability (μ_0), and the numeric value of the speed of light (c) in vacuum, which is well-known and expressed in the following equation:

$$c = \frac{1}{\sqrt{\epsilon_0 \mu_0}} \tag{2.1.1}$$

Where $\mu_0 = 4\pi \times 10^{-7}$ H/m ; $\epsilon_0 = (1/36\pi) \times 10^{-9}$ F/m ; and $c = 3 \times 10^8$ m/s.

Although vacuum is "empty" in a classical sense, it still has inherent electromagnetic properties characterized by ϵ_0 and μ_0. These constants describe the vacuum's resistance to changes in electric and magnetic fields. The speed of light is a universal constant, linking space and time in the fabric of spacetime. Its dependence on ϵ_0 and μ_0 shows that these constants are intrinsic properties of spacetime itself, influencing not just light but all electromagnetic phenomena. From Equation 2.1.1, a higher value of ϵ_0 or μ_0 would slow down the propagation of electromagnetic waves by reducing the speed of light (c). This effect becomes evident when transitioning from a vacuum to another dielectric medium, such as food in our case, where the concept of relative permittivity is introduced.

The relative permittivity denoted by ϵ_r, is a dimensionless quantity that describes how an electric field interacts with a material compared to a vacuum. This quantity has a complex nature formed of real and imaginary parts. The complex representation of the dielectric constant captures both the material's ability to store and dissipate electrical energy.

$$\varepsilon_r = \frac{\varepsilon_{abs}}{\varepsilon_0} = \varepsilon' - j\varepsilon'' \tag{2.1.2}$$

ε_{abs} is the actual permittivity of the material before normalizing it with ε_0. The real part in Equation 2.1.2 ϵ' represents how much electric energy can be stored inside the material when it is subjected to an external electric field and it is also called the dielectric constant of the material. However, the imaginary part of the same equation ϵ'' corresponding to how much the material is lossy or dissipative when it is subjected to the same field.

In this thesis, we focus on developing a microwave sensing system capable of accommodating a wide variety of food and beverage products, which corresponds to a broad range of relative permittivity values. To achieve this objective, it is essential first to analyze the dielectric properties of different types of food. Generally, the dielectric constant of food ranges from 2 to 80 [110], depending primarily on two factors: fat- or oil-based food media, which are characterized by low dielectric constant values, and water-based food media, which are high-loss materials with high dielectric constant values. The goal is to create a single measurement system capable of operating with both oil-based and water-based food and beverage products. As discussed earlier in the first chapter, the fundamental concept of a microwave imaging or sensing systems is to detect the contrast in the relative permittivity between the background, represented by the food material, and the contaminant materials. Therefore, it is important to analyze the relative permittivity of common contaminant materials that may be found in food and beverage products, such as plastic (Polytetrafluoroethylene (PTFE) and Polyethylene Terephthalate (PET)), glass (Soda–Lime Glass (SLG)), and wood, as well as the relative permittivity of various food components, including water and oil.

Table 2.1.1: Relative permittivity ranges for various contaminants over a frequency range of 2 to 10 GHz.

Contaminants	Relative permittivity range (ϵ_r)
PTFE	2 - 2.1
PET	3 - 3.2
SLG	4.7 - 10
Wood	2 - 16

Table 2.1.1 presents the relative permittivity ranges for different types of contaminants over a frequency range of 2 to 10 GHz. For the measurements of the dielectric properties of oil and water, we use a 2-ports P9375A Keysight VNA [112] along with 85070D Keysight dielectric probe together with the keysight software suite [113]. Figure 2.1.1(b) shows that the relative permittivity of water significantly exceeds that of oil Figure 2.1.1(a), resulting in a more pronounced dielectric contrast with respect to the contaminant materials shown in Table 2.1.1 compared to the contrasts between the permittivity of oil and the contaminants. This heightened contrast facilitates the detection of intrusions in water as opposed to oil. On the other hand, the conductivity values are notably higher in the case of water, indicating a reduced penetration depth within water compared to oil.

2.1.2 Penetration Depth and Frequency Bandwidth selection

Selecting the operating frequency bandwidth is a trade off between the penetration depth of electromagnetic (EM) waves, the dimensions of the food jar being tested, and the required resolution to detect intrusions as small as a few millimeters. In this study, we focus on testing food jars with standard dimensions, such as the 350 g chocolate cream jar. These jars are standard commercial products with an elliptical cylindrical shape, featuring a minor axis of 6.6 cm, a major axis of 7.5 cm, and a height of 10.5 cm. Designing a system capable of operating across different frequency bandwidths is crucial for detecting various types of contaminants in food and beverage products. Shorter wavelengths offer higher spatial resolution, making them ideal for detecting smaller intrusions, as resolution is inversely proportional to wavelength. On the other hand, longer wavelengths are preferable in lossy media due to their greater penetration depth capability. High-loss materials present challenges for wave penetration, but selecting an appropriate operating frequency bandwidth can effectively address this challenge. The penetration

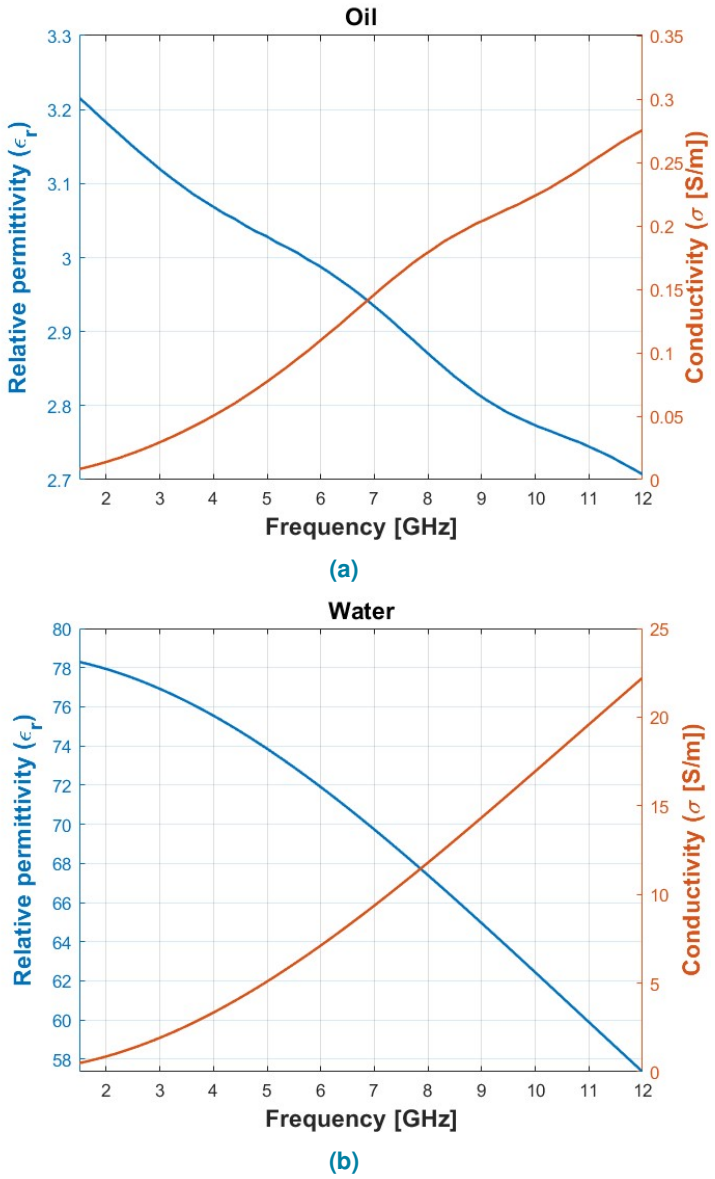

Figure 2.1.1: (a) Relative permittivity and conductivity of oil. (b) Relative permittivity and conductivity of water [111]

depth, δ, is calculated using the following formula:

$$k = k_0\sqrt{\varepsilon_r - j\frac{\sigma}{\omega\varepsilon_0}} = \beta - j\alpha, \quad \delta = \frac{1}{\alpha}, \tag{2.1.3}$$

in which k is the propagation constant, $k_0 = \omega\sqrt{\varepsilon_0\mu_0}$ is the free space propagation constant, ω is the angular frequency, ε_0 and μ_0 are the free space permittivity and permeability respectively, ε_r and σ are the medium relative permittivity and conductivity respectively.

A sufficient penetration depth must be ensured to fully cover the volume under test. Penetration depth is defined as the distance electromagnetic wave can penetrate into a material before its energy decreases to 1/e, approximately 37% of its original value at the boundary. As shown in Figure 2.1.2, higher frequencies result in lower penetration depths; however, higher frequencies also provide better

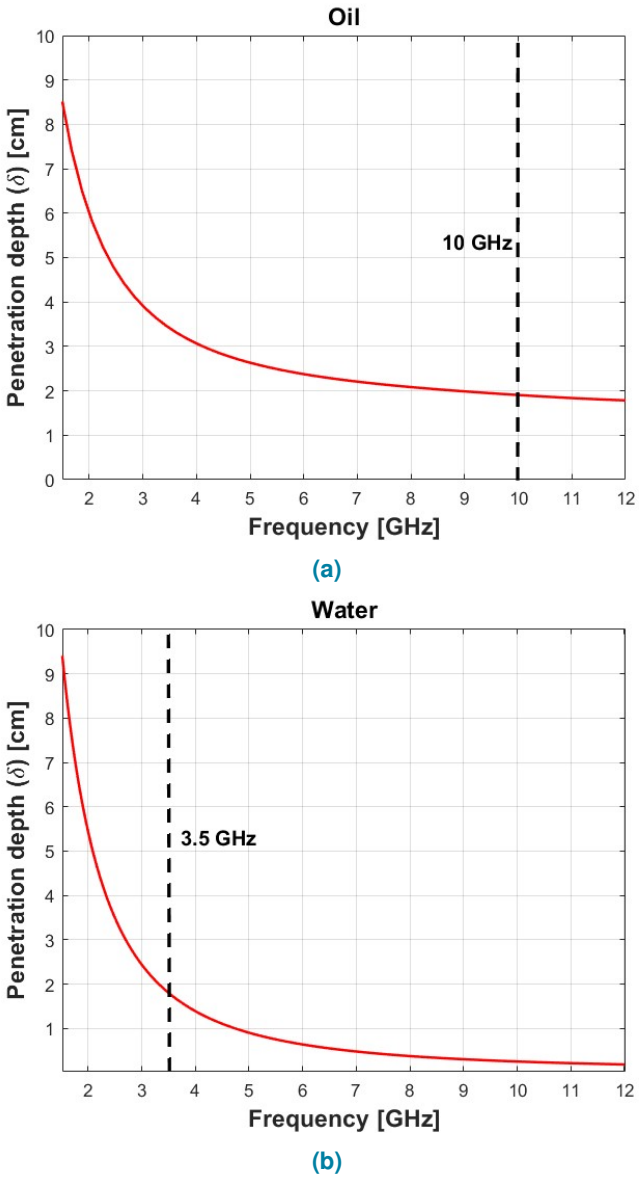

Figure 2.1.2: (a) Penetration depth within oil. (b) Penetration depth within water [111]

resolution for detecting smaller physical contaminants. The penetration depth plots (Figure 2.1.2) for oil and water emphasize the importance of establishing an upper frequency limit for each material to avoid excessively low penetration depths, particularly in water. Conversely, the lower limit of the operating frequency bands for each material depends on the required resolution to detect physical intrusions a few millimeters in size within the material.

A penetration depth of 2 cm ensures that the waves interact sufficiently with the material near the center of the jar without requiring excessively low frequencies, which would compromise resolution. Given the jar's diameter of 8 cm, a penetration depth of 2 cm allows the wave energy to decay as it propagates through the material, but not to the point where signal detection or interaction becomes impractical. Based on this, the upper frequency limits are selected as 10 GHz for oil-based products and 3.5 GHz for water-based products.

The propagated wavelength divided by 4 ($\lambda_p/4$) is significant in defining the spatial resolution and the system's ability to detect small features or structures within the medium. If we consider the relative permittivity of oil (ε_r = 2.8) at 10 GHz, we find that $\lambda_p/4$ = 4.5 mm. However, for water with a relative permittivity (ε_r = 75) at an upper frequency limit of 3.5 GHz we calculate $\lambda_p/4$ to be equal to 2.5 mm. These spatial resolutions demonstrate the system's capability to detect small physical intrusions, validating the chosen upper frequency limits for both cases.

To determine the lower frequency limits, we calculate $\lambda_p/4$ for each case. For oil-based products (ε_r = 2.9) at 6 GHz, $\lambda_p/4$ is 7.3 mm, while for water-based products, (ε_r = 78) at 1.5 GHz for, $\lambda_p/4$ is 5.6 mm. It is important to note that in this application, the goal is not to precisely identify the size of the contaminant but simply to detect its presence. Therefore, the critical factor is not achieving the highest spatial resolution possible but ensuring the field scattered by the contaminant is detectable at the lowest intensity. This consideration supports the selection of these frequencies as the lower limits for the two cases.

In conclusion, we define the operating frequency bandwidth as 6 GHz to 10 GHz for oil-based food samples, and 1.5 GHz to 3.5 GHz for water-based food products.

2.2 System Design

2.2.1 Antenna Design Parameters

The antenna is a key component in any microwave sensing system, as it is responsible for transmitting and receiving microwaves. In our application, selecting the appropriate antenna type is crucial for designing an efficient microwave sensing system. When evaluating the role of antennas in this context, several key factors must be considered, including bandwidth, polarization, radiation pattern, and gain. Bandwidth specifies the range of frequencies over which the antenna operates effectively, while polarization refers to the property of an EM wave that defines the time-varying direction and relative magnitude of its electric field vector. The radiation pattern illustrates the directional behavior of the antenna, which is important in most microwave applications. Gain is defined as the ratio of the radiation intensity in a specific direction to the radiation intensity that would be obtained if the input power were radiated isotropically [114]. In our case, where the sensing technique is applied in the near-field region, the antenna's gain becomes less relevant, as it is primarily a far-field concept.

In this system, we opted for a PCB-printed monopole antenna with a clover-shaped design, inspired from [115]. The omnidirectional nature of the antenna provides wide angular coverage, allowing it to transmit and receive microwaves from all directions. This capability enables the detection of contaminants at various positions within the jar being tested. The simplicity and omnidirectional characteristics of monopole antennas make them suitable for close-range applications. However, achieving wide bandwidth poses challenges, such as maintaining a stable radiation pattern across the entire bandwidth, ensuring proper impedance matching, and addressing electrical size constraints. Considering all these parameters, we optimize the antenna from [115] to meet the specific requirements of our application, prioritizing stability in the radiation pattern, the desired bandwidth, and proper impedance matching.

The clover-shaped antenna consists mainly of four ellipses, as shown in Figure 2.2.1. The Super-Wideband (SWB) radiator features multiple resonating patches with abrupt terminations to get multiple

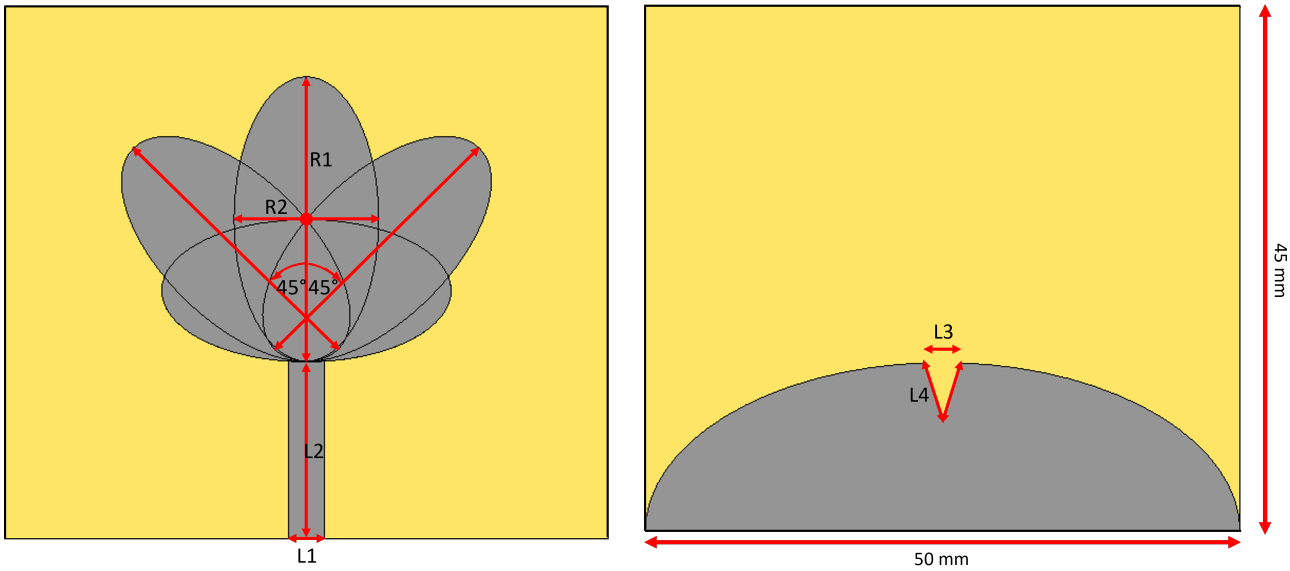

(a) Front view of the design

(b) Rear view of the design

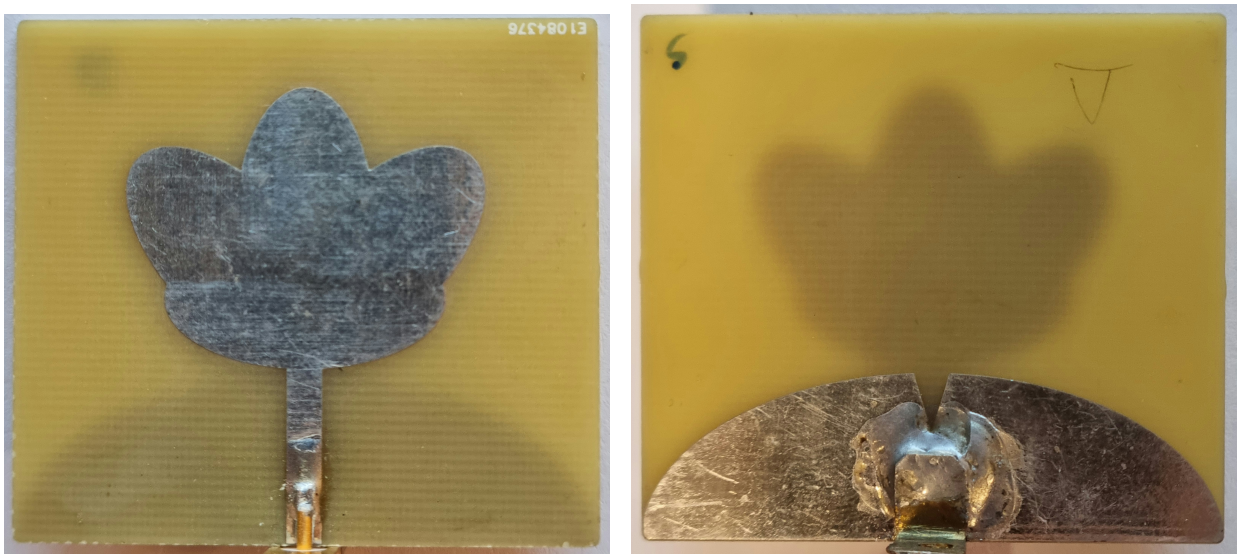

(c) Front view after fabrication

(d) Rear view after fabrication

Figure 2.2.1: Red labels indicate the following: L1 and L2 represent the width and length of the antenna's transmission line, while R1 and R2 denote the longer and shorter radii of the four ellipses comprising the antenna structure. Additionally, L3 and L4 correspond to the dimensions of the V-cut triangular shape in the ground plane [111].

resonances. Each ellipse has a larger radius (R1) of 24 mm and a smaller radius (R2) of 12 mm. The primary ellipse is aligned with the transmission line at a 0° angle relative to it. Two additional ellipses form the flower-shaped structure by being rotated +45° and -45° relative to both the transmission line and the central ellipse. The fourth ellipse is aligned horizontally and rotated 90° with respect to the transmission line. The four ellipses are combined to create a clover-shaped geometry, ensuring wideband performance from approximately 1 GHz to beyond 30 GHz. The clover-shaped design exhibits some symmetry, which results in achieving a more uniform omnidirectional radiation pattern. However, the

radiation characteristics are influenced by the flower-like arrangement of the four ellipses.

The antenna is designed according to the following standards: the metallic flower structure of the antenna and the ground plane have a thickness of 0.03 mm and they are printed on a standard FR-4 substrate (ϵ_r = 4.1) with a thickness of 1.55 mm. The overall dimension of the antenna is 50 $\times$ 45 mm^2. L1 and L2 represent the width and length of the transmission line, measuring of 3 mm and 15 mm, respectively. The ground plane has a semi-ellipsoidal shape with an optimal triangular cut, as shown in Figure 2.2.1(b). L3 and L4, measuring 3 mm and 5.2 mm respectively, represent the optimal dimensions of the V-cut, chosen to achieve the best impedance matching performance within the desired frequency band.

2.2.2 Optimal Number of Antennas

Once the type of antenna is selected, the next step is to determine the optimal number of antennas and their configuration around the food product under test. This is essential for maximizing the amount of relevant information gathered while minimizing complexity and avoiding redundancy. The required number of antennas in microwave sensing and imaging applications is influenced by factors such as the desired image resolution, the size of the target object, and the wavelength of the electromagnetic waves. Generally, increasing the number of antennas improves sensing performance by providing more detailed information about the target. However, a larger number of antennas also increases system complexity and cost. Thus, it is crucial to balance the number of antennas with sensing performance, system size, and cost considerations.

The optimal number of antennas can be estimated starting from degrees of freedom theory in electromagnetic [116, 117]. This technique has already been used in the design of biomedical MWI systems in [77, 118] based on the spatially band-limited properties of EM fields [119]. Taking into account the geometric dimensions of the target's cross-section and its intersection with the antenna plane, the required number of samples can be estimated to measure the radiated fields from a source of the same size as the target along a curve enclosing it. In [119] a novel approach was done to estimate the number of the of samples required for a non-repetitive measurement of the field emitted by a source encompassed within a curve with a perimeter denoted by 'P'. According to the Nyquist rule estimated in the aforementioned reference, $N_0 = \frac{2P}{\lambda}$, it is recommended to take evenly spaced samples at a distance of $\lambda/2$. N_0 serves as an upper limit for the number of independent samples necessary to accurately capture the scattered field. The resulting N0 provides an estimate of the required number of antennas for obtaining independent and non-redundant data.

In [120], the authors apply this method to estimate the optimal number of antennas required for designing an MWI system to detect contaminants within food packaging. The cross-section of the cylindrical jar under test forms a rectangle with sides measuring 6.6 cm and 7.5 cm, corresponding to the major and minor axes, respectively. Based on these target dimensions and a frequency of 10 GHz, N_0 is calculated to be approximately 18. Due to system constraints, it is not possible to position any antenna directly facing the lower part of the tested sample. This limitation arises from the presence of the conveyor belt and its supporting structure, which holds both the belt and the food samples. Consequently, N_0 is reduced by half (= 9 antennas). Furthermore, since the VNA [113] used in this application has six ports, N_0 is further reduced to six antennas for this configuration. The six antennas are arranged in an arc shape surrounding the jar under test, as illustrated in Figure 2.2.3.

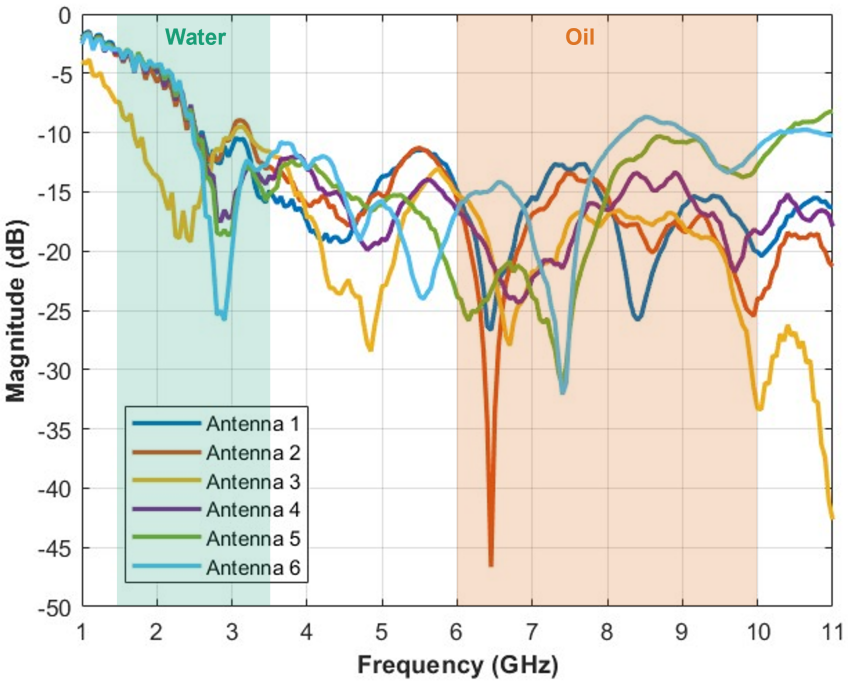

Figure 2.2.2: The Reflection Coefficient Magnitude (S_{11}) of the Six Antennas in the System

Figure 2.2.2 presents the reflection coefficients (S_{11}) of the six fabricated antennas used in the microwave sensing and imaging system. The S_{11} plots demonstrate good matching performance, spanning approximately from 2 GHz to 11 GHz.

2.2.3 In-Line Microwave Sensing Inspection Scanner

After selecting the appropriate antenna type, determining the optimal number of antennas required for our application, and configuring their arrangement around the tested samples, we introduce the microwave sensing system illustrated in Figure 2.2.3. The system consists of six antennas mounted on an arch-shaped support, enabling samples to pass through smoothly without interruptions or delays. These antennas are connected to a six-port VNA [113], which captures the transmitted signal from the radiating antenna in complex-number format across the operating frequency band.

To minimize industrial interference, the antenna array setup is enclosed within a shielding box. The outer layer of the box is metal, mitigating external interference, while the inner layer is made of microwave absorbers to reduce signal reflections. The food industry's conveyor belt operates at an average speed of 20 meters per minute (approximately 33 cm/s), necessitating compatibility between measurement and data processing times. A photocell is used to trigger the VNA, initiating the measurement as the jar approaches the antenna array. This process ensures accurate timing through an automatic, adaptive delay.

The subsequent sections provide a comprehensive overview of the, numerical analyses, and the antenna's performance evaluation in its near-field region.

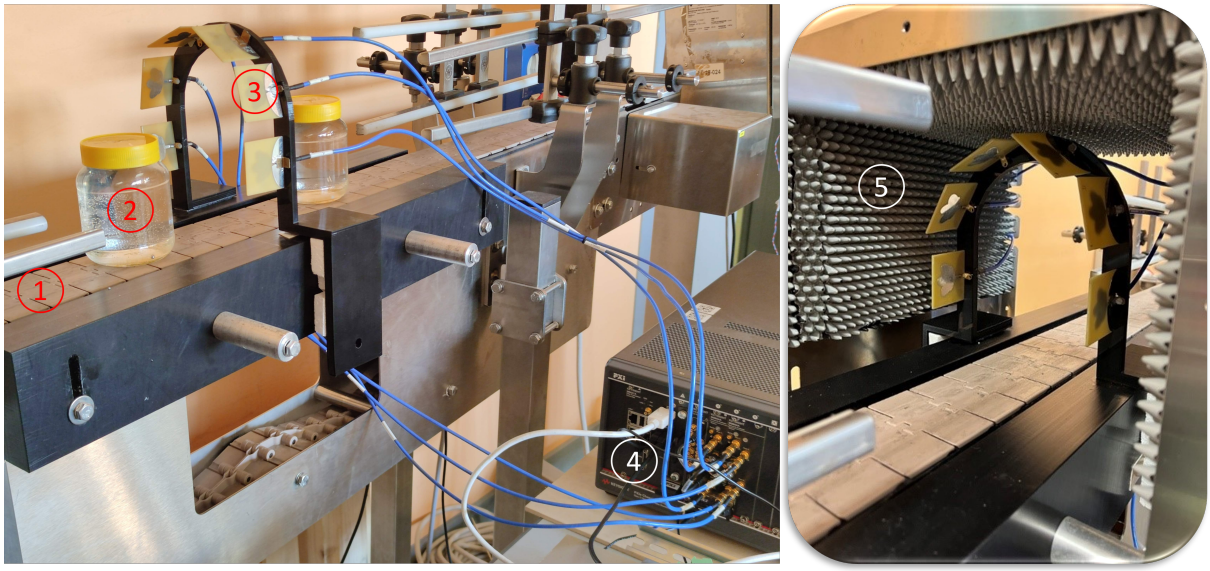

Figure 2.2.3: The measurement system consists of: (1) the conveyor belt, (2) the jar being tested, (3) the antennas, (4) the vector network analyzer (VNA), and (5) the shielding box. [111].

2.3 Near-Field Analysis: Measurements and Simulations

Near-field microwave sensing is conducted with a relatively short electrical distance between the antenna and the surface of the MUT. In this region, the presence of reactive evanescent waves enables high sensitivity, while the concentrated electromagnetic energy (facilitated by small-sized probes) allows for high-resolution imaging. The resolution and sensitivity of near-field sensing to variations and flaws in the sample depend on the probe's aperture size, the electromagnetic field distribution in its near-field region, and the distance to the target. The near-field region can be divided into two subregions: the reactive near-field, where evanescent waves are present and decay rapidly, enabling high sensitivity for sensing applications, and the radiating near-field (Fresnel-Region), where electromagnetic waves begin to propagate away from the antenna. The limit of the radiated near-field region ($R_{rad–NF}$) is determined by the following equation:

$$0.62\sqrt{\frac{D^3}{\lambda}} < R_{rad\text{-}NF} < \frac{2D^2}{\lambda}, \tag{2.3.1}$$

where D = 6.7 cm is the maximum dimension of the antenna (the diagonal), and λ is the wavelength. From 2.3.1, we observe that $R_{Rad\text{-}NF}$ is confined between two boundaries: it immediately follows the reactive near-field region and precedes the start of the far-field region (Fraunhofer-Region).

Table 2.3.1: The extent of the radiated near-field region ($R_{rad\text{-}NF}$) at the upper and lower frequency limits of the oil and water bandwidths.

Food material	Frequency (GHz)	$R_{rad\text{-}NF}$ range (cm)
Oil	6	4.8 – 18
Oil	10	6.2 – 30
Water	1.5	2.4 – 5
Water	3.5	3.8 – 11

For the selected frequency bands, $R_{Rad\text{-}NF}$ is estimated using Equation 2.3.1 at the limits of each band: 1.5 GHz and 3.5 GHz for water-based measurements, and 6 GHz and 10 GHz for oil-based measurements. Table 2.3.1 provides the range of $R_{Rad\text{-}NF}$ for both water and oil cases. In the measurement setup, the shortest distance between the antennas and the jar is approximately 5 cm, specifically between either antenna 1 or antenna 2 and the jar, as shown in Figure 2.3.1. For the oil-based frequency band, this distance falls within the radiated near-field range at 6 GHz, which spans from 4.8 cm to 18 cm. However, at 10 GHz, this distance lies in the reactive near-field region, as the radiated near-field region begins at 6.2 cm and extends to 30 cm. For the water-based frequency band, the jar is located at the upper limit of the radiated near-field region at 1.5 GHz, where the region begins at 2.4 cm and extends up to 5 cm. At 3.5 GHz, the jar lies within the radiated near-field region, which spans from 3.8 cm to 11 cm. This analysis should also account for the dimensions of the jar and the varying distances between the jar and the other antennas in the configuration. Consequently, it can be concluded that the measurements primarily occur in the radiated near-field region. However, at certain frequencies, such as 10 GHz, the jar falls within the reactive near-field region when considering the 5 cm distance between the jar and the closest antenna (antennas 1 and antenna 2). However, for the other antennas, where the distance is greater, the measurements take place within the radiated near-field region.

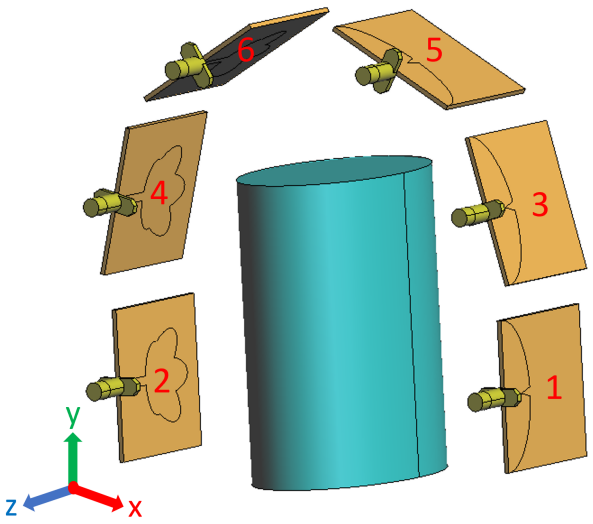

Figure 2.3.1: The simulated setup corresponds to the real measurement arrangement with six antennas positioned around the jar under test [111].

For a comprehensive understanding of the performance of the antenna array elements integrated into our sensing system, simulations and measurements are conducted to analyze the near-field region. The following subsections offer an in-depth examination and assessment of the Electric-Field (EF) propagation radiated by the antenna within the region of interest.

E-Field distribution in the Near-Field region

To measure the near-field, we randomly selected one of the six antennas and we use the near-field measurement setup shown in Figure 2.3.2. This system includes a network analyzer, the transmitting

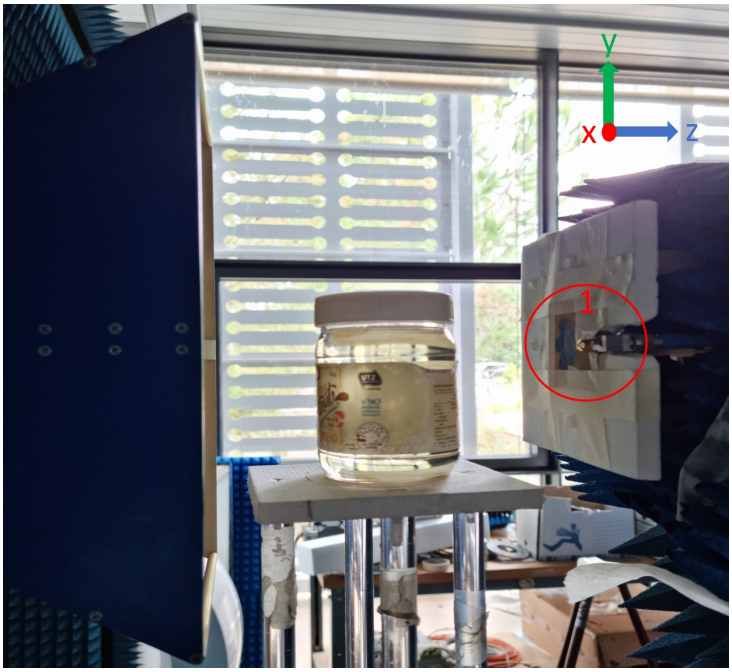

(a)

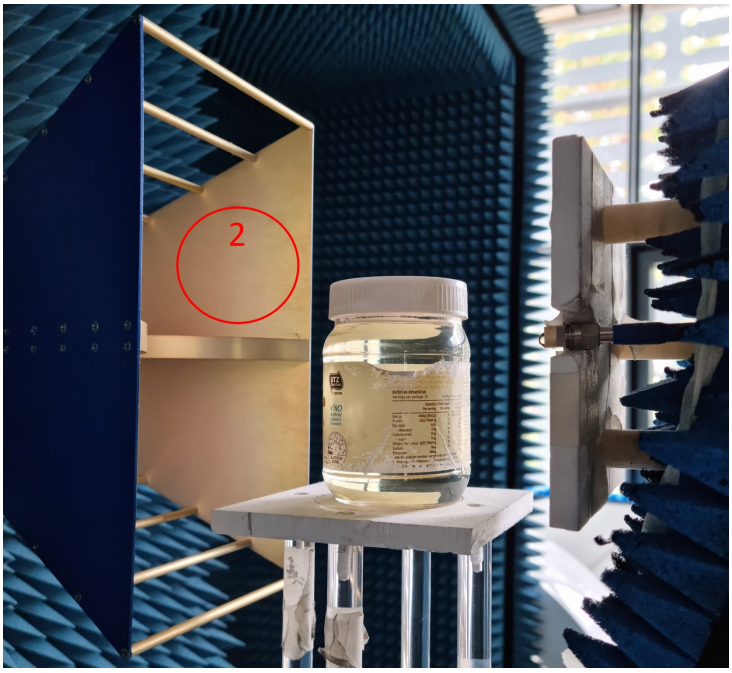

(b)

Figure 2.3.2: The near-field measurement system [111]: (a) The setup includes the transmitting antenna, labeled as 1, which is the flower-shaped antenna used in the configuration. (b) The setup also features the receiving wideband horn antenna, labeled as 2.

antenna from our study, and the receiving antenna, which is a wide-band horn antenna operating starting from 2 GHz. Measurements and simulations were performed across a wide frequency range of 2 to 12 GHz, providing data for near-field characterization and subsequent time-domain analysis—both essential are useful to fully understand and analyze the addressed problem.

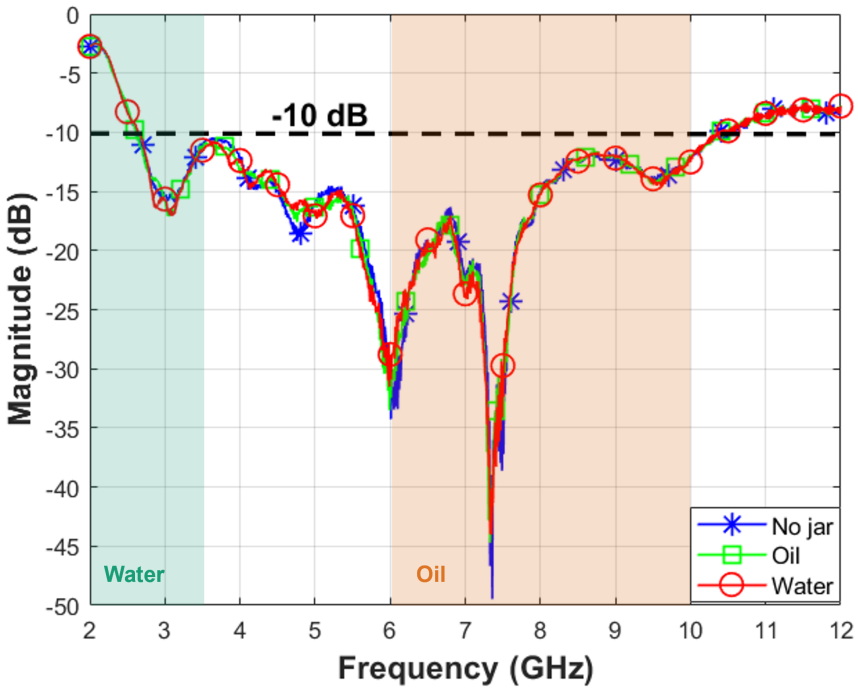

Figure 2.3.3: The measured S_{11} amplitudes for the employed antenna in three scenarios: an empty jar, a jar filled with oil, and a jar filled with water [111].

Before performing the near-field measurements, we record the S_{11} of the transmitting antenna under three different scenarios by measuring the reflection coefficients at the antenna port. These scenarios are illustrated in Figure 2.3.3. In the first scenario (blue curve), we analyzed the impedance matching of the antenna without any jar present. The results demonstrate good matching performance within the bandwidths of interest, except at the lower frequencies of the lower bandwidth, as highlighted by the green and orange shaded regions in Figure 2.3.3. However, since the system operates with a jar present, two additional scenarios were examined: one with a jar filled with oil (green curve) and another with a jar filled with water (red curve). The three curves are nearly superimposed, indicating that the presence of the jar does not significantly impact impedance matching. Overall, the antenna exhibits good matching except below 2.5 GHz. While mismatching below this frequency suggests reduced power transmission into the jar, it does not entirely prevent transmission, particularly for water-based products. For instance, at 2 GHz, the penetration depth is 6 cm (as shown before in Fig 2.1.2(b)). Consequently, it is early to exclude the frequency range between 1.5 and 2.5 GHz at this stage. Further analysis of the experiments and classification results will determine the relevance of these frequencies.

To measure the near-field of the antenna, a mechanical stepper motor is used to move the receiving horn antenna for scanning purposes. The transmitting and receiving antennas are aligned centrally and positioned 17 cm apart. The horn antenna captures the radiated waves across a scanning area of 20 cm in the vertical y-direction and 25 cm in the horizontal x-direction, with a step increment of 2.5 mm in both directions. Since the focus is on measuring the antenna's near-field, the measurements are conducted without the jar present. The results, shown in Figure 2.3.4, depict the magnitude of the near-field (normalized to the maximum value across all frequency points). The plots reveal a decline in

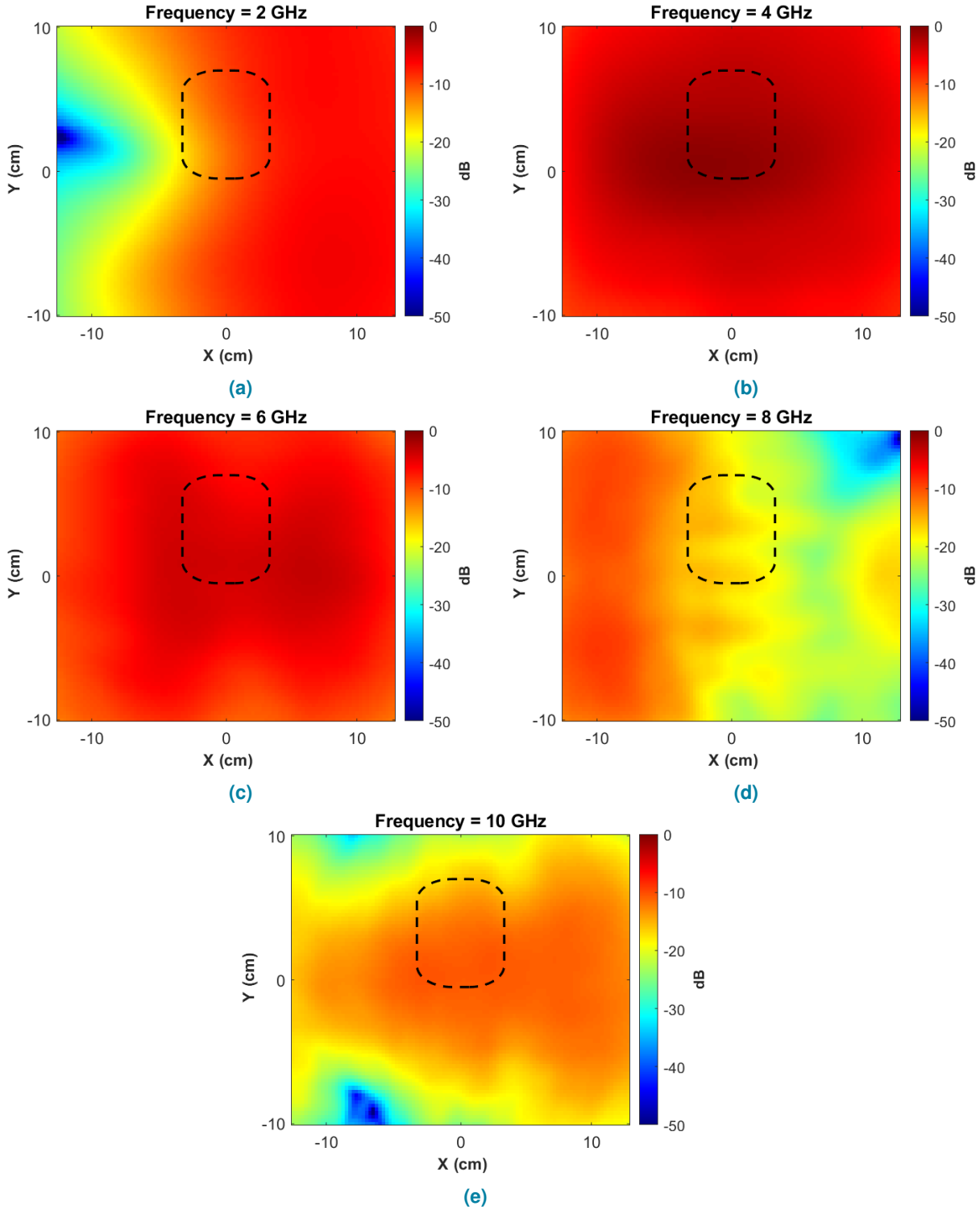

Figure 2.3.4: The measured amplitude of the antenna's near-field (normalized to the maximum magnitude across all frequency points) without any jar present. The dotted rectangular shape in the plot represents the expected position of the food jar within the measurement setup [111].

field strength as the frequency increases, particularly beyond 8 GHz. This observation will be corroborated by the overall system measurements discussed in the dataset construction section.

2.3.1 Simulated antenna near-field radiation

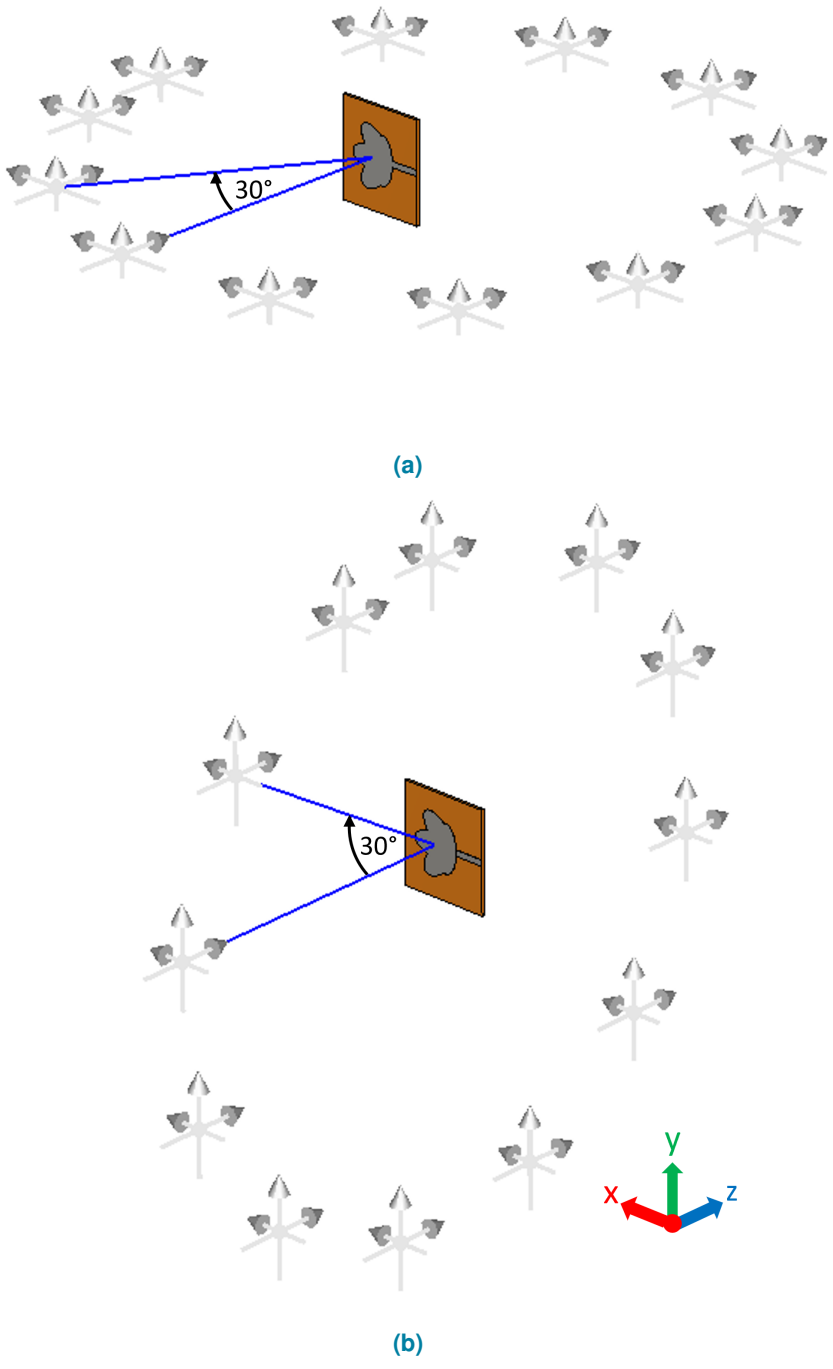

Figure 2.3.5: The radiated antenna, and surrounding it in a circular arrangement from 1° to 360° are receiving probes, each positioned at every 1° interval: (a) The XZ plane with $\varphi = 0°$, $\theta \in [0, 360°]$. (b) The YZ plane with $\varphi = 90°$, $\theta \in [0, 360°]$

To gain deeper insights into the near-field pattern changes, we derive the electric field strength in the near-field from the simulation. To achieve this, we incorporate two field probe arrays arranged in a circular

configuration around the antenna with a radius of 15 cm. This radius represents the maximum separation distance between two elements within our antenna array. The setup shown in Figure 2.3.5 allowed us to capture the electric field components in azimuth at φ equals zero, and in elevation at φ equals 90°.

In Figures 2.3.6 and 2.3.7, we illustrate the E-field characteristics, including the total E-field magnitude as well as its x, y, and z components, presented in separate plots for the utilized antenna across different frequencies in two planes: one with φ set to 0° (XZ plane) and the other with φ set to 90° (YZ plane). Based on the findings showcased in Figures 2.3.6 and 2.3.7, it is worth noting that the magnitude of the x-component of the E-field, which has the same orientation as the feeding line, is closely aligned with those of the total field. In contrast, the magnitudes of the y and z components are notably lower, as expected. This analysis is useful in establishing an approximate understanding of the radiation pattern in the near-field and may also elucidate the observed decline in the magnitude of the near-field above 8 GHz shown in Figure 2.3.4(d,e). This drop is due to the spatial shift in the main lobe of the pattern as the frequency changes. However, as our antenna array is comprised of six antennas arranged in an arc shape, each time an antenna emits radiation, one of the other antennas receives back the scattered waves, which contain information about the jar.

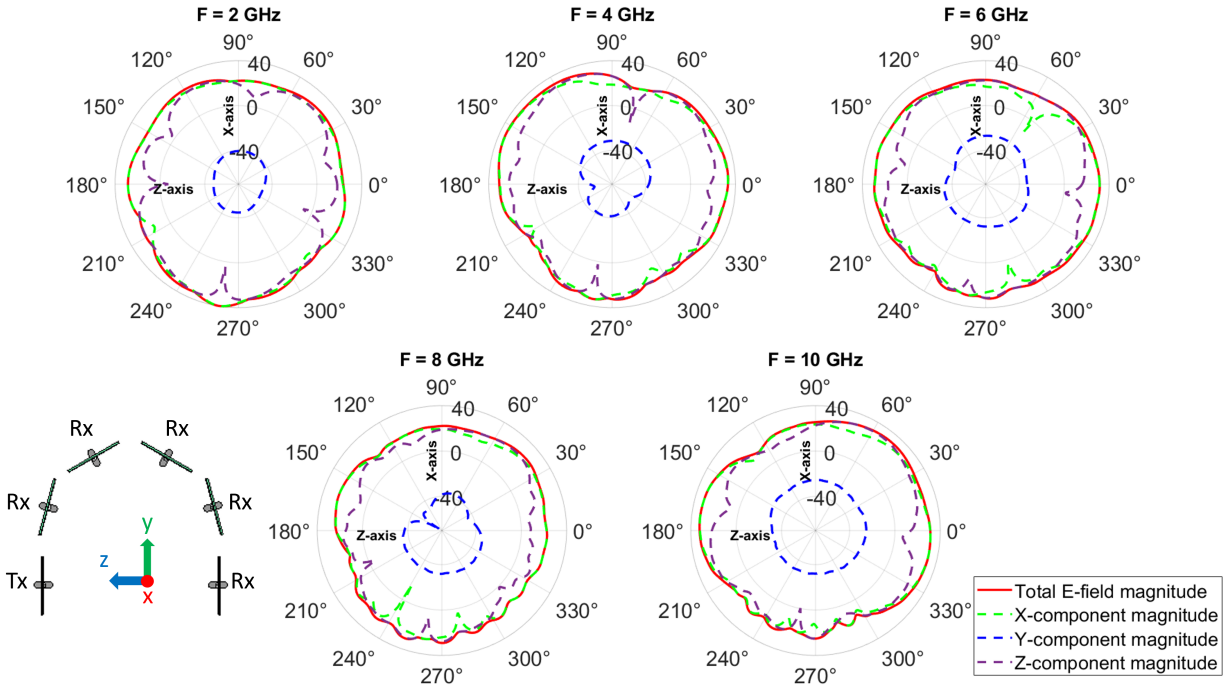

Figure 2.3.6: Electric field strength [dB(V/m)] within XZ plane in the absence of any jar at: 2 GHz, 4 GHz, 6 GHz, 8 GHz and 10 GHz. The labels "Tx" and "Rx's" indicate the transmitting and receiving elements of the antenna array respectively.

2.3.2 Electric-Field (EF) Spatial Coverage

The spatial coverage of the E-field serves as a measure of how effectively an antenna array illuminates a specific point within the radiated volume. In simpler terms, it evaluates how thoroughly the electromagnetic waves emitted by the antenna array reach and interact with a particular point in the testing space. To gain

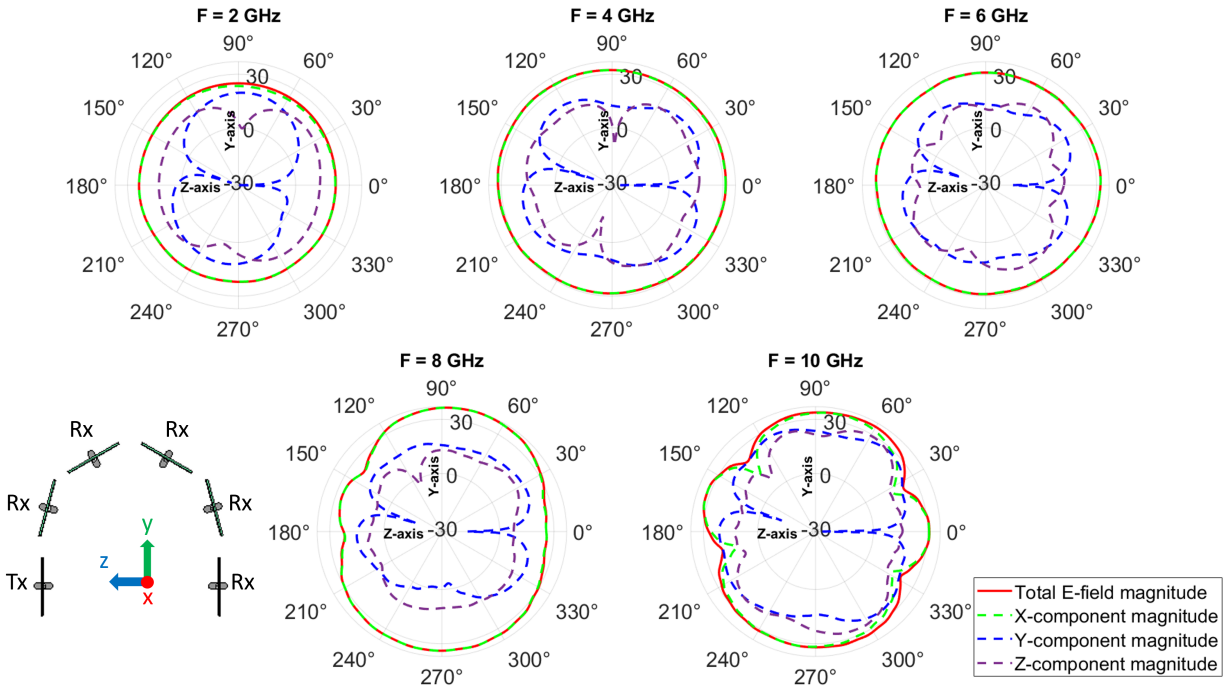

Figure 2.3.7: Electric field strength [dB(V/m)] within YZ plane in the absence of any jar at: 2 GHz, 4 GHz, 6 GHz, 8 GHz and 10 GHz. The labels "Tx" and "Rx's" indicate the transmitting and receiving elements of the antenna array respectively.

a clearer understanding of E-field spatial coverage, we simulate the system using its actual dimensions, as shown in Figure 2.3.1. The water-filled jar case is selected for simulation due to the challenges posed by high losses. The simulations are performed at a frequency of 2.5 GHz, which represents the center frequency within the chosen bandwidth for testing water samples. The definition of E-field spatial coverage is given as follows:

$$C_E^{\alpha}(\mathbf{r}, f) = \frac{\sum_{n=1}^{T} \mid \mathbf{E}_n^{\alpha}(\mathbf{r}, f) \mid}{\max \sum_{n=1}^{T} \mid \mathbf{E}_n^{\alpha}(\mathbf{r}, f) \mid}, \tag{2.3.2}$$

where $\mathbf{r}$ denotes the position vector, T represents the total number of antennas, and $\mathbf{E}_n^{\alpha}$, with $\alpha = i, t, s$, corresponds to the incident, total, and scattered E-fields, respectively. Each $\mathbf{E}_n^{i}$ is obtained when the n-th antenna radiates with the jar filled only with water. Conversely, $\mathbf{E}_n^{t}$ represents the E-field radiated by the n-th antenna when contaminants are present inside the filled jar. Finally, $\mathbf{E}_n^{s} = \mathbf{E}_n^{t} - \mathbf{E}_n^{i}$ describes the E-field scattered by the contaminants. When the n-th antenna is radiating, all other antennas are are matched to a 50 Ω. Therefore, T = 6 different simulations are conducted to evaluate the E-field spatial coverage, with each time a different radiating antenna.

Figure 2.3.8(a) presents the $C_E^{i}(\mathbf{r})$, clearly showing that the E-field coverage is at its lowest levels at the bottom of the jar. To account for the worst-case scenario, five plastic spheres, each with a diameter of 2 mm, are positioned at the bottom of the jar as contaminants. Subsequently, Figure 2.3.8(b) illustrates $C_E^{t}(\mathbf{r})$, which represents the coverage when the contaminants are introduced. The total coverage appears very similar to the incident field. However, Figure 2.3.8(c), showing the scattered coverage, distinctly

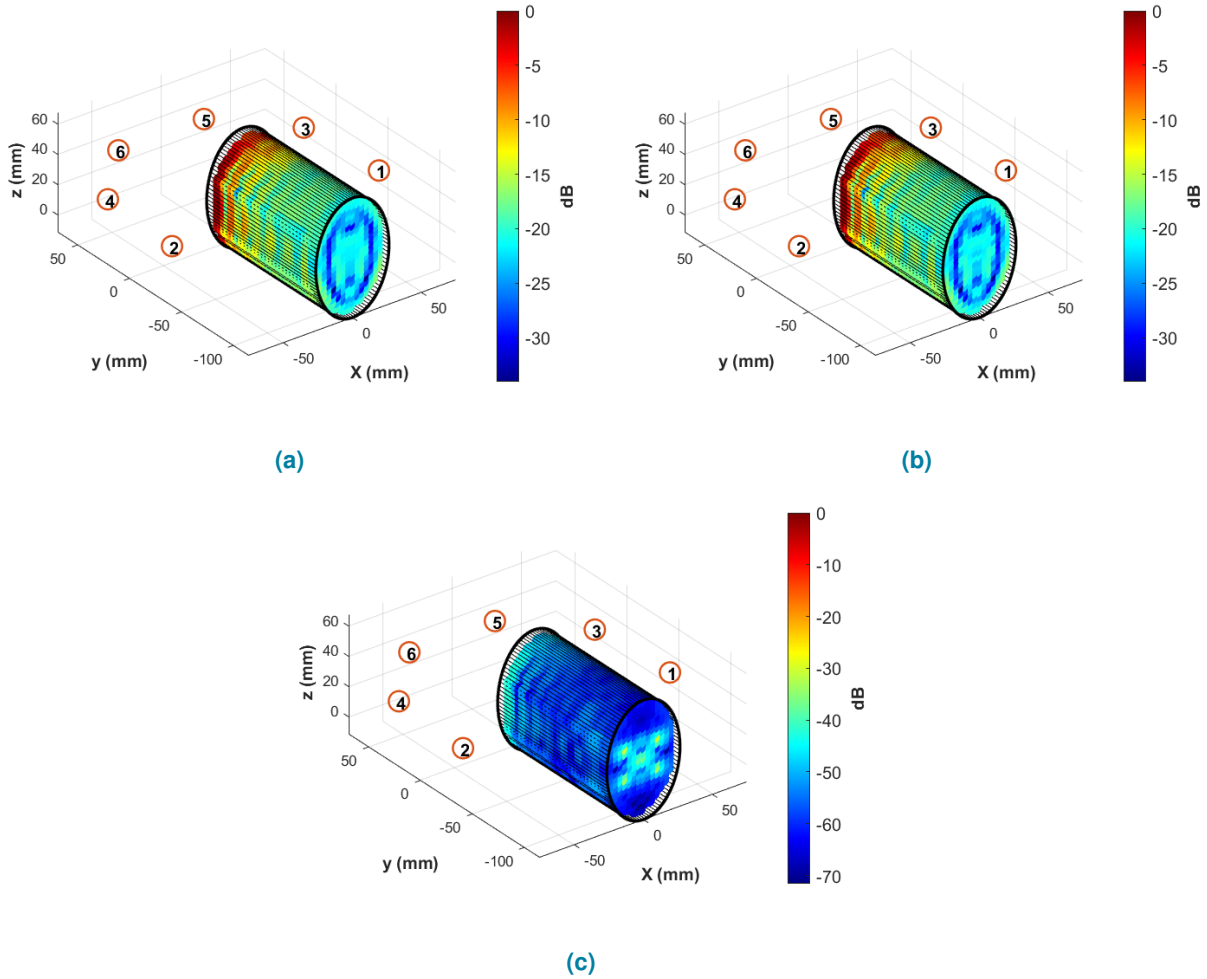

Figure 2.3.8: E-field spatial coverage at 2.5 GHz within the water-filled jar [111]: (a) incident field, (b) total field, and (c) scattered field.

reveals the presence and precise location of the contaminants, making them clearly distinguishable.

2.4 Time-Domain Reflectometry

Time-Domain Reflectometry (TDR) is an electromagnetic technique in which a pulse emitted by a transmitter reflects off an object of interest and returns to the receiver. The travel time and velocity of the pulse are used to calculate the distance to the object [121]. In TDR, a pulse generator sends electrical pulses along a transmission line, and when a pulse encounters a change in the medium's electrical properties, a portion of it is reflected back to the generator [122]. The elapsed time between the pulse's emission and the reception of its reflection can be used for two purposes: (1) identifying the location where the medium's electrical properties have changed, or (2) determining the speed of the pulse. Fault or level detection along the transmission line involves identifying alterations in its electrical properties. In such cases, the pulse's speed is influenced by the electrical characteristics of the transmission line, and the round-trip travel time is used to infer the location of these changes.

TDR is a widely used technique in non-destructive evaluation, leveraging the phase of the reflection

coefficient to gain valuable insights into the object under test. In this context, we apply TDR to analyze both our simulated and measured data. The goal of examining the TDR of reflection coefficient parameters, derived from these simulations and measurements, is to identify signal reflections originating from the radiated region. This analysis can be conducted either through direct time-domain measurements or by performing frequency-domain measurements followed by applying the Inverse Fast Fourier Transform (IFFT). To identify discontinuities within the system, it is crucial to utilize a broad time-domain observation window with fine intervals. Reflection coefficients are measured over a frequency range of 2 GHz to 12 GHz, with 10 MHz intervals for both simulations and measurements. By comparing the electrical distances obtained from simulations and measurements across different media and analyzing the maximum measurable distance (x_{max}) obtained in 2.4.1, we can detect the key reflection points in the system. These points include the antenna's feed port, its phase center, the jar filled with water, and the contaminant within the jar.

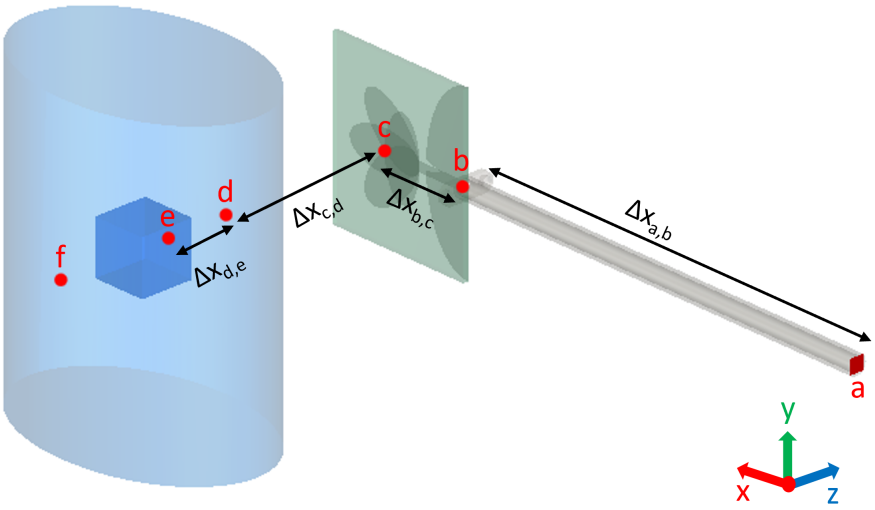

Figure 2.4.1: The simulation setup is the same as the measurement system but without the foreign body [111].

In Figure 2.4.1, we present the simulation setup for TDR analysis. The labels (a) through (f) indicate the following key points: (a) the waveguide port, (b) the feeding port of the antenna, (c) the center of the antenna structure, (d) the center of the water jar's face opposite the antenna, (e) the position of the contaminant within the water, and (f) the edge of the jar on the opposite side. Four simulations were performed to examine the time-domain behavior under different conditions. The first simulation used as a reference, with a jar filled only with water and no contaminants. In two of the other simulations, a plastic cube contaminant is introduced, each placed in a different position within the jar. The final simulation replaces the plastic contaminant with a metallic (copper) material. The Inverse Fast Fourier Transform (IFFT) is applied to the simulated reflection coefficient data, and the maximum distance x_{max}, is determined using:

$$x_{max} = \frac{c \cdot T_{max}}{2}, \quad T_{max} = \frac{1}{df}, \tag{2.4.1}$$

where x_{max} denotes maximum measurable distance in centimeters, c is the speed of light in free space,

T_{max} is the maximum time window available for analysis, and df is the frequency resolution.

To ensure precise calculations, it is important to consider the range resolution, which refers to the antenna's ability to differentiate between closely spaced targets. Discussing range resolution is essential when addressing discontinuities in the antenna and the system. For instance, to accurately identify the reflection points, the range resolution must be smaller than the distance between any two consecutive points in Figure 2.4.1. Thus, the range resolution must be inserted into the calculations to determine the positions of these discontinuity points accurately. The range resolution is expressed as:

$$\Delta R = \frac{c}{2 \cdot BW}, \tag{2.4.2}$$

Here, ΔR represents the range resolution, and BW = 10 GHz denotes the bandwidth used in the simulations and measurements. Based on Equation 2.4.2, the calculated range resolution is 1.5 cm.

Table 2.4.1: The analysis of the distance ΔX is presented in Figure 2.4.2. The second column indicates the relative permittivity of the medium along the specified distance. The third column provides the corresponding geometrical distance, while the fourth column represents the theoretical electrical distance. Lastly, the fifth column shows the simulated electrical distance as obtained and shown in Figure 2.4.2(a,b).

	ϵ_r	Geometrical distance (cm)	Electrical distance theoretical (cm)	Electrical distance simulation (cm)
$\Delta X_{a,b}$	2.1	13.5	19.6	18 ± 1.5
$\Delta X_{b,c}$	4.3	2.7	5.6	6 ± 1.5
$\Delta X_{c,d}$	1	5.1	5.1	3 ± 1.5
$\Delta X_{d,e}$	78	1.85	16.3	16.4 ± 1.5
$\Delta X_{a,e}$	-	$\sum \Delta X$(geometrical) = 23.15	$\sum \Delta X$(electrical) = 44.6	46.5 ± 1.5

Figure 2.4.2(a) presents the IFFT results for the simulated reflection coefficients measured at point (a) in Figure 2.4.1. The labels (1), (2), and (3) in this subfigure correspond to the reflection points (b), (c), and (e) from Figure 2.4.1, respectively. The positions of the peaks in the IFFT plots are determined by calculating the electrical distance, which is obtained by multiplying the geometrical distance (from the simulated design or measurement system) by the square root of the relative permittivity of the propagating medium, as shown in Table 2.4.1. This method helps identify which part of the simulation or real measurements corresponds to each peak in the IFFT plot. In Figure 2.4.2(a), the contaminant inside the jar is not detected, as the plots overlap with the reference curve (without the contaminant). To resolve this, we propose to subtract the reflection coefficients recorded in the presence of the contaminant from those obtained in the reference simulation and then perform the IFFT on the remaining values. The results of this process are shown in Figure 2.4.2(b), where a peak at x = 46.5, cm is clearly associated with the presence of the contaminant inside the water. This peak is more pronounced when the contaminant is metallic. The contaminant's position within the jar affects the reflection point at x = 61.4, cm, and the peak at x = 77.9, cm is due to the reflection from the rear side of the jar. This shift in the reflection points is caused by the contaminant's impact on the wave propagation within the water, which leads to the observed difference in the third peak of Figure 2.4.2(b) compared to the reference scenario without the contaminant.

A comparison of the data in the final two columns of Table 2.4.1 shows good agreement between the theoretically estimated positions of the reflection points and those observed in the IFFT plot in Figure 2.4.2(a,b), when considering the range resolution. The error observed in ($\Delta X_{c,d}$) can be attributed

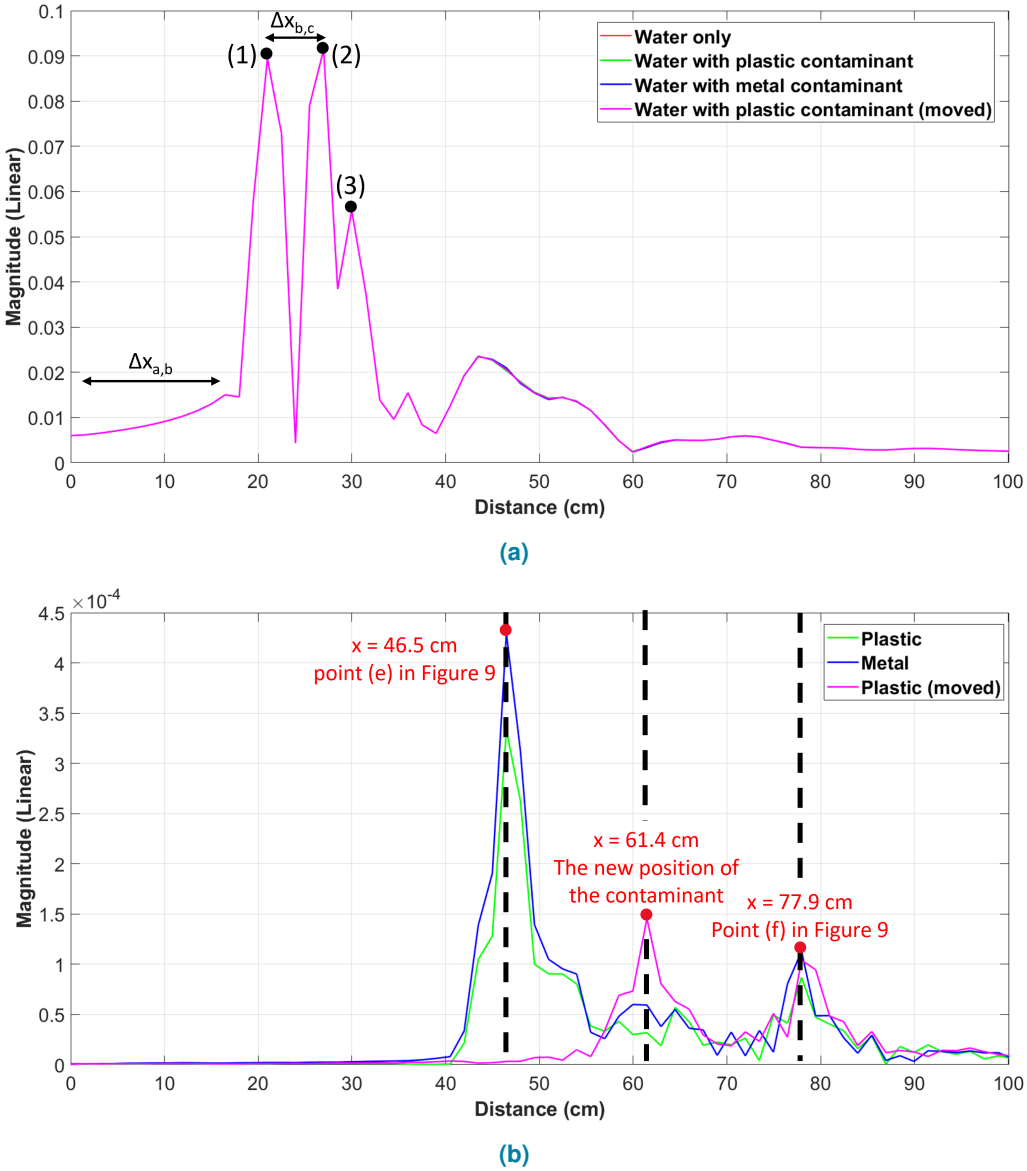

Figure 2.4.2: [111]: (a) IFFT of the reflection coefficients of the simulated antenna. (b) IFFT of the difference in reflection coefficients (simulation) between each distinct scenario and the reference case with only water (no contaminants present).

to the assumption of the antenna's phase center being at the exact position of point c, as shown in Figure 2.4.1.

To further assess the system's ability to detect changes in the reflection coefficients based on the contents of the jar, we record the antenna's reflection coefficient parameters using the same setup as in the near-field study (Figure 2.3.2). We examine three scenarios: one without a jar, one with a jar filled with oil, and another with the same jar filled with water. In Figure 2.4.3, the labels on the curve indicate the estimated reflection points. The peaks marked (1) and (2) correspond to the feeding port and the antenna's phase center, respectively. The three curves overlap until reaching the peak at point (3), which represents the reflection from both the support holding the jar and the jar itself, as shown in Figure 2.3.2.

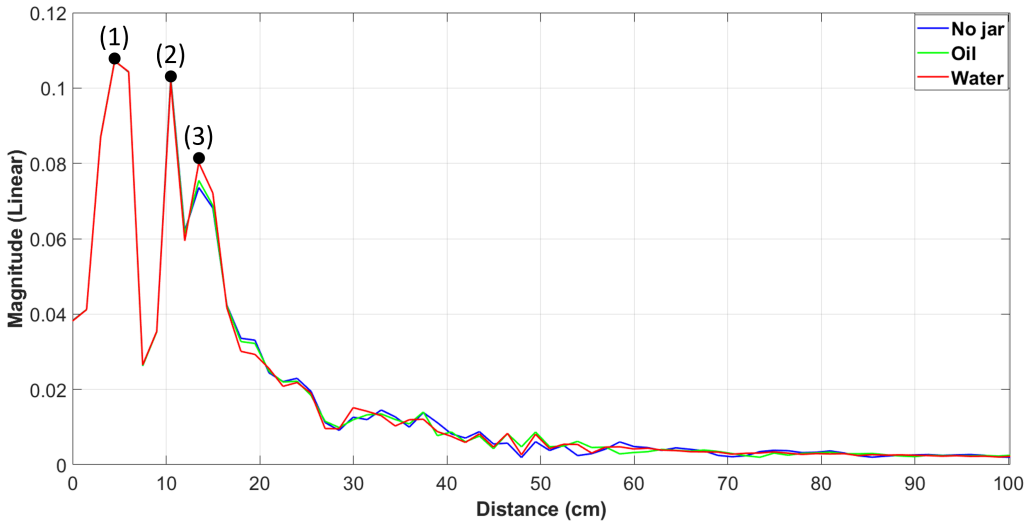

Figure 2.4.3: The amplitude of the IFFT results obtained from the measured reflection coefficients [111].

The reflections at this point clearly show the effect of the medium inside the jar on the reflection intensity, with the effect being more pronounced when the jar is filled with water (red curve) compared to when it contains oil (green curve) or when there is no jar (blue curve).

It is also worth noting the consistency of the three peaks (1), (2), and (3) across both the simulation results in Figure 2.4.2(a) and the measurements in Figure 2.4.3. However, the positions of these peaks are shifted by the length of the coaxial cable ($\Delta X_{a,b}$) in Figure 2.4.2(a).

3 Classification Methods

In the first chapter, we introduced the primary focus of this thesis: detecting physical contaminants in packaged food and beverage products, as well as identifying defects in the agricultural industry. The integration of microwave sensing systems with machine learning (ML) tools offers a solution by enabling real-time scanning in an inline production process. This approach is both cost-effective and efficient, as it reduces processing time and expenses. Additionally, it can manage diverse types of databases, eliminating the need for multiple systems to handle different materials or defect types.

In general, ML models often utilize concepts such as probability, regression, classification, clustering, and other statistical techniques to analyze and interpret data. These tools are designed to identify patterns, features, and trends within the data and to make predictions or decisions based on these insights. In our study, we apply ML classification tools to data such as the scattering matrices obtained from food product samples under test. The main difference between these samples lies in the presence or absence of contaminants and defects. These ML techniques focus on detecting the impact of this difference directly from scattering parameters, such as reflection or transmission coefficients.

In this chapter, we will introduce two types of machine learning classification algorithms: Support Vector Machine (SVM) and Multilayer Perceptron Neural Network (MLP). Additionally, we will highlight the importance of Principal Component Analysis (PCA) for database visualization. Furthermore, we will discuss the Grey Wolf Optimization (GWO) method, which was employed to enhance the performance and accuracy of the aforementioned classifiers.

3.1 Main Learning Paradigms in ML

Supervised learning

Supervised learning is a fundamental approach in machine learning where the algorithm is trained on a labeled dataset, meaning that each input observation is paired with a corresponding output label. The primary objective is to learn a mapping function that associates input data with the correct output. During the training process, the algorithm algorithm processes each data point or sample in the training dataset, makes predictions, and compares these predictions to the actual labels, known as the ground truth. Based on this comparison, the model's performance is evaluated, and its parameters are adjusted iteratively to minimize errors and improve accuracy. Supervised learning is extensively used in a variety of real-world applications. In regression tasks, it predicts continuous outcomes, such as estimating house prices, forecasting weather conditions, or determining stock market trends. In classification tasks, it assigns discrete labels to inputs, such as identifying whether an email is spam or not [123],

recognizing handwritten digits in images [124], diagnosing diseases from medical images [125], or categorizing customer feedback into sentiment classes [126]. The versatility of supervised learning also makes it indispensable in tasks like speech recognition [127], language translation [128], and facial recognition [129]. By leveraging high-quality labeled data, supervised learning empowers systems to make accurate predictions and informed decisions across numerous domains.

Unsupervised learning

Unsupervised learning is a machine learning approach where the dataset lacks labels, requiring the algorithm to independently identify patterns or structures within the data. This method is particularly useful in scenarios where labeled data is sparce, expensive, or difficult to obtain. Common applications include clustering for customer segmentation [130], document categorization [131], and image segmentation [132]; anomaly detection for fraud prevention, fault detection [133], and cybersecurity [134]. Other notable uses include autoencoders for data compression and image denoising [135], genomics for understanding genetic relationships [136], social network analysis for community detection [137]. Unsupervised learning enables organizations across various industries to derive insights and optimize processes using large volumes of unlabeled data.

In classification applications, handling large datasets poses a significant challenge in supervised learning. However, the results are more accurate and reliable, as the model learns from labeled data and follows a structured approach. On the other hand, unsupervised learning is capable of processing large volumes of data in real time but often lacks transparency in how the data is clustered, leading to a higher risk of inaccurate outcomes. The ability to obtain labels for each sample makes supervised learning approaches the best choice for our application. This is because it allows for measurements to be taken on different types of samples with prior knowledge of their condition, such as whether they are contaminated or not in the case of food packaging classification. The dataset can then be prepared by assigning the correct label to each observation.

3.2 Support Vector Machine (SVM)

The Support Vector Machine (SVM), introduced in 1995 in [138], is a supervised learning method commonly utilized for binary classification tasks. SVM is based on the concept of decision boundaries by finding the optimal separation between classes through support vectors, which are the data points closest to the decision boundary, or hyperplane. This capability makes SVM a practical choice for applications with limited data, as seen in our study. SVM can be categorized into two primary types: linear and non-linear. Linear SVM is suitable for simple classification tasks where the data from both classes can be separated by a straight line, while non-linear SVM is better suited for complex scenarios where the data are non-linearly separable and exhibit correlations.

Linear SVM

A linear SVM is applied when the training data is linearly separable in the data space, as illustrated in Figure 3.2.1. Consider a training dataset consisting of N labeled samples (x_i, y_i), where x_i represents the i-th sample and y_i represents the label of the i-th sample, with $x_i \in \mathbb{R}$ and $y_i \in \{-1, 1\}$. The hyperplane

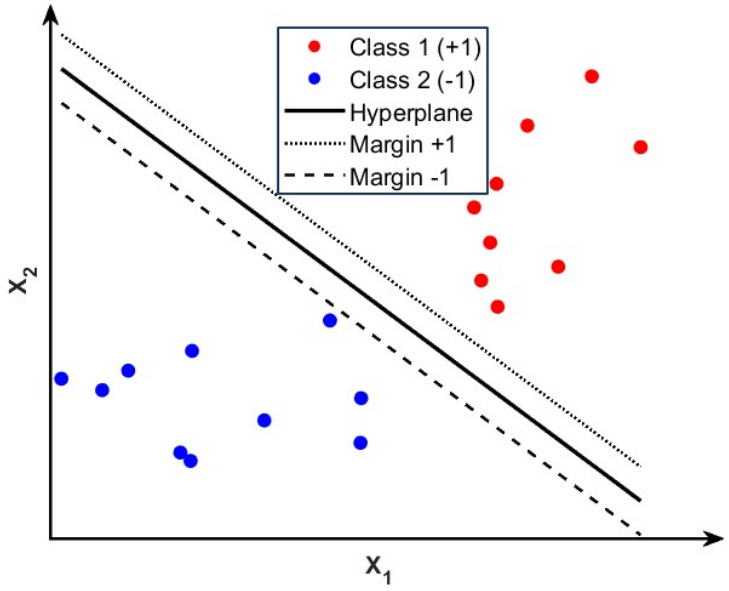

Figure 3.2.1: Visualization of a linear SVM showing two classes of data, the optimal separating hyperplane, margins, and support vectors.

that separates the samples of the two classes (positive and negative classes) is defined by the following equation:

$$p(x) = (w^T x + b) = 0 \tag{3.2.1}$$

where w is the vector normal to the hyperplane and b is a constant bias parameter. During the training phase, the optimal hyperplane is found with a maximum margin that separates the samples from the two classes. That is, at the end of the training phase, the parameter vector w and the constant b are determined, and the decision function is defined by Equation 3.2.2:

$$d(x) = \text{sign}(w^T x + b) \tag{3.2.2}$$

If $d(x_i) \geq 0$, the label assigned to sample x_i is $y_i = +1$; if $d(x_i) \leq 0$, then $y_i = -1$. The decision function serves as the perpendicular distance of a generic point x from a hyperplane defined by $p(x) = 0$ is given by $\frac{|p(x)|}{\|w\|}$, the distance of the n-th sample x_n to the decision surface is:

$$\frac{y_n p(x_n)}{\|w\|} = \frac{y_n (w^T x + b)}{\|w\|} \tag{3.2.3}$$

In this case, $p(x_n)$ has been replaced with its full expression from Equation 3.2.1. If x_n is the closest point to the decision boundary, the perpendicular distance ($\frac{1}{\|w\|}$) described in Equation 3.2.3 represents the margin. Therefore, maximizing the margin requires maximizing Equation 3.2.3. This optimization problem can be simplified through rescaling, where we set the numerator to satisfy $y_n(w^T x + b) = 1$. Under this scaling, maximizing the margin ($\frac{1}{\|w\|}$) is equivalent to minimizing ($\|w\|$). For simplicity and mathematical convenience, $\|w\|$ is replaced by $\|w\|^2$, the squared norm, which avoids the square root operation. Additionally, a scaling factor of $\frac{1}{2}$ is introduced to simplify differentiation in convex optimization

problems. As a result, the optimization problem becomes:

$$\arg\min_{w,b} \frac{1}{2}\|w\|^2 \tag{3.2.4}$$

which means finding the optimal values of w and b that minimize the squared norm of the weight vector. This is equivalent to maximizing the margin $\|w\|^{-1}$ (the distance between the hyperplane and the nearest data points on either side, also known as support vectors). With this simplification, the canonical representation of the decision hyperplane can also be expressed, which all training samples must satisfy:

$$y_n(w^T x_n + b) \geq 1, \quad n = 1, 2, \ldots, \mathrm{N} \tag{3.2.5}$$

Up to this point, it has been assumed that the final result would be a perfectly separating hyperplane. However, achieving exact separation of the training data can often result in poor generalization. To address this, a controlled allowance for some misclassified training points is introduced. Consequently, the training process must simultaneously maximize the margin and minimize the number of errors. Therefore, a penalty, referred to as the slack variable $\xi_n \geq 0$, is associated with each n-th data point. This depends on the position and distance of each sample relative to the decision boundary:

- $\xi_n = 0$: The sample is correctly classified, meaning it lies on the correct side of the decision boundary and outside the margin.
- $0 < \xi_n \leq 1$: The sample is within the margin, even though it remains on the correct side of the decision boundary.
- $\xi_n > 1$: The sample is misclassified, as it lies on the wrong side of the decision boundary.

As a result, the classification constraints in Equation 3.2.5 are replaced with:

$$y_n(w^T x_n + b) \geq 1 - \xi_n, \quad n = 1, 2, \ldots, \mathrm{N} \tag{3.2.6}$$

This implies that the previously defined exact margin is now transformed into a soft margin. The second consequence is that the minimization problem in Equation 3.2.4 is transformed from a more rigid, exact form to a more flexible form.

$$\arg\min_{w,b} \left(\mathrm{C} \sum_{n=1}^{\mathrm{N}} \xi_n + \frac{1}{2}\|w\|^2 \right) \tag{3.2.7}$$

Where $\mathrm{C} > 0$ is a regularization hyperparameter that controls the trade-off between minimizing training errors and model complexity. Since the term $\mathrm{C}\sum_{\mathrm{n}=1}^{\mathrm{N}} \xi_{\mathrm{n}}$ is fixed, a larger value of C results in a more complex decision boundary, as the minimization in Equation 3.2.7 requires more effort. In other words, a smaller value of C leads to a smoother decision surface, while a larger value of C aims to classify all training samples correctly, making the decision surface more complex. C must be optimized as it establishes a trade-off between the margin width, regularization, and the number of misclassified samples.

- **Case 1:** The larger the value of C, the smaller the margin, resulting in lower classification error.
- **Case 2:** The smaller the value of C, the larger the margin, but with an increased classification error.

The optimization problem (the quadratic programming problem presented in Equation 3.2.7) is solved by maximizing the dual form of the Lagrangian function:

$$\max L(a) = \sum_{i=1}^{N} a_i - \frac{1}{2} \sum_{i=1}^{N} \sum_{j=1}^{N} y_i y_j a_i a_j x_i^T x_j \tag{3.2.8}$$

Here a is the set of Lagrange multipliers. and (a_i, a_j) are specific Lagrange multipliers for individual training points.

subject to the constraints:

$$0 \leq a_i \leq C \quad \text{for} \quad i = 1, 2, \ldots, N \tag{3.2.9}$$

and

$$\sum_{i=1}^{N} a_i y_i = 0 \quad i = 1, 2, \ldots, N \tag{3.2.10}$$

An important property of SVMs is that determining the model parameters involves solving a convex optimization problem, ensuring that any local solution is also the global optimum.

The solution yields a, which is then used to compute w^* and b^*:

$$w^* = \sum_{i=1}^{SV} a_i y_i x_i \tag{3.2.11}$$

$$b^* = y_i - w^{*T} x_i \tag{3.2.12}$$

Here, SV represents the number of support vectors, as only the support vectors contribute to the summation (those for which $a_i \neq 0$).

After the training process, when the minimization problem has been solved, the classification of a new data point $\mathbf{x}_{\text{new}}$ can be performed by evaluating Equation 3.2.1, since w^* and b^* are now known:

$$d(x_{new}) = \text{sign} \left(\sum_{i=1}^{SV} w^{*T} x_{new} + b^* \right) \tag{3.2.13}$$

Non-Linear SVM

In most real-world classification problems, the training data cannot be linearly separated in the original feature space. To address this, the input space is mapped to a higher-dimensional space where linear separation becomes possible. This transformation is achieved using a suitable nonlinear mapping function, (ϕ), applied to data (x). Consequently, the decision function of a non-linear SVM can be expressed as:

$$d(x) = \text{sign} \left(\sum_{i=1}^{SV} a_i y_i \phi(x_i)^T \phi(x) + b \right) = \text{sign} \left(\sum_{i=1}^{SV} a_i y_i K(x_i, x) + b \right) \tag{3.2.14}$$

with

$$b = y_i - \sum_{i=1}^{SV} a_i y_i K(x_i, x) \tag{3.2.15}$$

In this context, $K(x_i, x) = \phi(x_i)^T \phi(x)$ is referred to as the kernel function. Some of the most commonly used kernel functions are as follows:

- **Polynomial**: $(\gamma\langle x_i, x\rangle + r)^d$
- **Sigmoid**: $tanh(\gamma\langle x_i, x\rangle + r)$
- **Gaussian Radial Basis Function (RBF)**: $e^{-\gamma||x_i - x||^2}$

Here, $\langle\cdot,\cdot\rangle$ represents the inner product, and $||\cdot||^2$ denotes the L2-norm.

The Radial Basis Function (RBF) kernel is commonly used because it maps data into a high-dimensional feature space where non-linear relationships can be captured. In this thesis, RBF kernel is applied. This type of SVM requires tuning two hyperparameters: the regularization parameter C and the kernel-specific parameter γ. The regularization parameter C as discussed before controls the trade-off between achieving a larger margin (simpler model with potential classification errors) and minimizing misclassification on the training data (more complex model that risks overfitting). The parameter γ defines the inverse of the radius of influence of the support vectors (SVs) selected during training. It determines how far a single support vector's influence extends in the feature space.

To understand γ, consider two extreme scenarios:

- **High γ:** When γ is too large, the influence of a single SV becomes highly localized. This creates a very tight decision boundary around specific data points, leading to overfitting, as the model captures even minor variations in the training data. Even reducing C cannot fully counteract this overfitting.
- **Low γ:** When γ is too small, the influence of each SV becomes so broad that it spans the entire training set. As a result, the model behaves like a linear classifier, using a simple hyperplane to separate the data, which may lead to underfitting.

The optimal value of γ lies between these two extremes. A well-tuned γ ensures that the model strikes a balance between capturing complex patterns in the data and maintaining generalization ability to unseen data.

The combination of SVM and microwave technology has been successfully applied to various fields, demonstrating its effectiveness and robustness. For example, in medical applications, it has been used for breast cancer detection and classification with microwave imaging devices [139], as well as for brain stroke classification using microwave imaging systems [90]. Additionally, SVM has been employed for sorting damaged apples [103, 104] and for classifying archaeological shards using mmW imaging systems [140].

Multiclass SVM

SVM was originally developed for binary classification, meaning it can distinguish between two distinct classes. To extend its use to multiclass classification as the example shown in Figure 3.2.2, the problem

is typically divided into multiple binary classification tasks. One common approach is the One-vs-One (OvO) method, where data points are mapped to a higher-dimensional space to achieve linear separation between each pair of classes. This approach creates a separate binary classifier for every pair of classes. Another method is the One-vs-Rest (OvR) approach, where a binary classifier is trained for each class against all other classes combined. This allows the model to determine whether a data point belongs to a specific class or not.

Thus, based on the two approaches, for a dataset with m classes:

- In the OvO approach, the classifier utilizes $\frac{m(m-1)}{2}$ SVMs, each distinguishing between a pair of classes.
- In the OvR approach, the classifier requires m SVMs, where each SVM determines whether a data point belongs to a specific class or not.

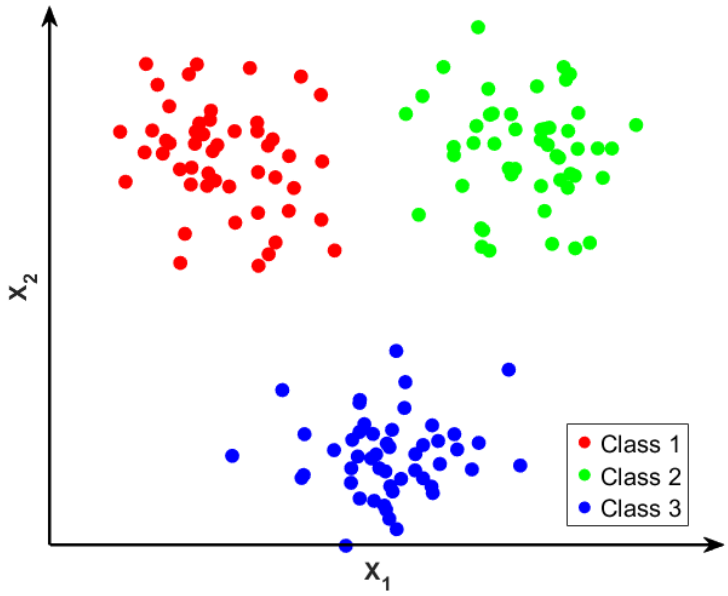

Figure 3.2.2: Visualization of three different classes in a multiclass classification scenario.

In this thesis, we use the sklearn.svm.SVC [141] library to implement SVM in Python, which defaults to the One-vs-One (OvO) multiclass strategy. We explore multiclass classification to differentiate between various types of contaminants. This is particularly relevant to the food industry, as identifying these contaminants can help pinpoint the stage at which contamination occurs, allowing for targeted efforts to minimize its impact during the production chain. However, as mentioned earlier in this subsection, SVM classifiers are primarily designed for binary classification problems. Therefore, it is important to consider other machine learning classifiers capable of handling multiclass classification, such as the Multi-Layer Perceptron (MLP) Neural Network.

3.3 Multi-Layer Perceptron (MLP) Neural Network

Multilayer Perceptron (MLP) is a supervised learning model that map a function $f(\cdot) : \mathbb{R}^m \rightarrow \mathbb{R}^o$ by training on a dataset. Here, m represents the number of input features, while o denotes the number of output dimensions. MLPs can be used as non-linear function approximators for classification or regression machine learning applications. They are an adaptation of the first Perceptron model, which Rosenblatt put forth in 1958 [142]. The analysis that follows is sourced from [143]. The MLP architecture follows a fully connected design and is organized into layers, each consisting of a series of neurons, also referred to as nodes or units. An activation function, a non-linear function $g(\cdot) : \mathbb{R} \rightarrow \mathbb{R}$, is implemented inside a j-th neuron of a generic hidden layer. This function transforms the input vector x from the previous layer using a weighted linear summation:

$$z_j' = g\left(\sum_{i=1}^{n} w_i x_i + b_j\right) \tag{3.3.1}$$

where w_i is the current layer's i-th weight, b_j is the j-th neuron's bias, z_j' is its output, and n is the number of nodes in the preceding layer. In case of multi-layer construction, z_j' then becomes the x_j of the subsequent layer, and so on. An illustration of an MLP with a single hidden layer can be found in Figure 3.3.1. The minimal number of layers in an MLP is three, with the left layer referred to as the input layer, the output layer at the right, and all additional layers between these two being the hidden layers. In this basic scenario, the non-linear function represented by the hidden layer is expressed in vector notation as:

$$z(x) = w_2\, g\left(w_1^T x + b_1\right) + b_2 \tag{3.3.2}$$

where w_1 and w_2 are the weight vectors of the input layer and hidden layer, respectively; b_1 and b_2 represent the biases applied to all the nodes of the hidden layer and output layer, respectively; $g(\cdot)$ is the activation function of the neurons in the hidden layer; and $z(x)$ is the hidden layer's output.

The input layer's depth is equivalent to $n_{features}$. Instead, except in the binary case, where one output neuron is sufficient, the number of output nodes $n_{outputs}$ in an MLP employed for classification purposes corresponds to the number of classes $n_{classes}$ that the model must categorize.

The parameters that the model must acquire during training are the vectors of the weights (w) and the biases (b) in Equation 3.3.2. A common approach to determine them is by minimizing the training error, which involves optimizing the Loss Function. Various loss functions are available depending on the type of problem. For classification tasks, Cross-Entropy is commonly used, which simplifies to Binary Cross-Entropy in the case of binary classification:

$$loss(\hat{y}, y, w) = -y \ln \hat{y} - (1 - y) \ln(1 - \hat{y}) + \alpha R(w) \tag{3.3.3}$$

where R is a regularization term that penalizes model complexity, y is the label associated with the input sample that the MLP processes, $\hat{y}$ is the predicted label, and $\alpha > 0$ is a hyper-parameter that regulates the severity of the penalty (also known as the Weight Regularization Parameter). The following are typical selections for the regularization term R:

- **L2 norm:** $R(w) = \frac{1}{2} \sum_{i=1}^{n} w_i^2$.

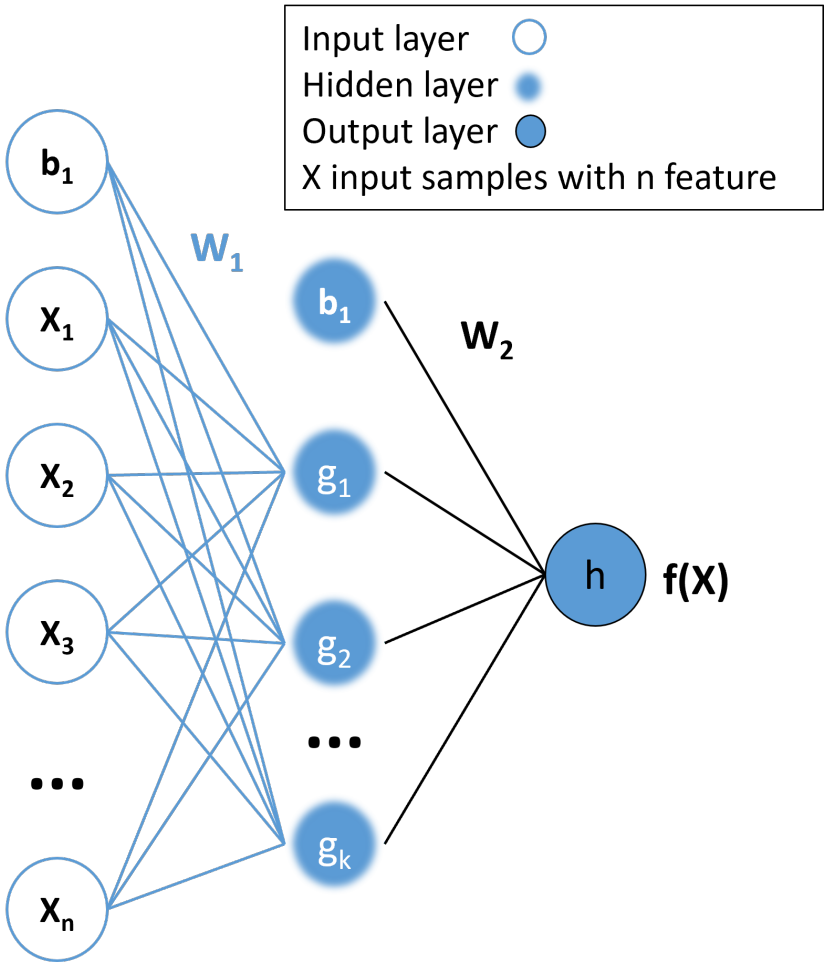

Figure 3.3.1: Example of MLP with one hidden layer.

- **L1 norm:** $R(w) = \sum_{i=1}^{n} |w_i|$.
- **Elastic Net:** $R(w) = \rho \frac{1}{2} \sum_{i=1}^{n} {w_i}^2 + (1-\rho) \sum_{i=1}^{n} |w_i|$, where ρ governs the combination of L2 and L1 norms.

Various optimization strategies, commonly referred to as optimizers in open-source Python libraries, are available to minimize the Loss Function. Among the most well-known are Adaptive Moment Estimation (Adam) [144], Stochastic Gradient Descent (SGD) [143], and the Limited-memory Broyden–Fletcher–Goldfarb–Shanno (L-BFGS) algorithm [145].

The SGD iterates through the training samples, updating the model parameters for each one by the update rule that follows:

$$w^{i+1} = w^{i} - \eta \nabla Loss(\hat{y}, y, w^{i}) \tag{3.3.4}$$

in which i is the iteration step, $\nabla Loss(\cdot)$ is the gradient of the loss concerning the weights w, and $\eta > 0$ is the learning rate, which regulates the step size of the parameter update. The bias parameters b are updated similarly; however, they are not subject to weight regularization.

Although η is a hyperparameter in SGD, Adam does not use it. An intriguing feature of Adam is its

capacity to automatically adjust the learning rate η and decrease it as training time increases [144]. This helps to remove the learning rate from the list of hyperparameters that need to be adjusted manually.

L-BFGS algorithm is a member of the Quasi-Newton family. These methods aim to find the local minima of functions by relying on Newton's method to determine the stationary points of functions. The L-BFGS algorithm performs well on large training datasets while requiring very little computational memory [146].

It is clear from Equation 3.3.4 that the weights must be initialized to compute the first iteration. Different random weight initializations may result in varying validation accuracy since the MLP has a non-convex loss function with many local minima [143]. Weights can be initialized using zeros, ones, a single constant for all weights, or random values from a normal distribution. In the literature, more advanced initializers have proven to be more effective. He Normal and LeCun Normal, in particular, perform very well. This is because they mitigate learning slowdowns by scaling the standard deviation of the Gaussian distribution used for weight initialization [147].

In conclusion, following weight initialization, the MLP for the binary case minimizes the Binary Cross-Entropy loss function (Equation 3.3.3) by iteratively updating the weights using Equation 3.3.4, assuming Stochastic Gradient Descent (SGD) is employed. Once the loss is computed, a backward pass propagates the error from the output layer to the preceding layers, adjusting each weight proportionally to the error at the output. The primary objective is to reduce the loss in subsequent iterations. The calculation of gradients and error propagation for weight updates is performed using an algorithm known as Back-propagation [147]. In the final section we provide a brief description of the remaining hyperparameters often considered when training an MLP:

- **Number of neurons and hidden layers:** Designing the architecture of an MLP primarily involves deciding on the number of hidden layers and the number of neurons in each hidden layer, which are critical hyperparameters. However, selecting these parameters is challenging due to the abundance of rules of thumb in the literature, often based more on practical experience than on theoretical principles. Guidelines vary across resources; for instance, [148] suggests that three layers are sufficient to approximate any arbitrary function, with additional layers only needed under specific conditions or requirements. That said, networks with multiple hidden layers are more vulnerable to issues like unwanted local minima. As a common starting point, practitioners often begin with a single hidden layer when addressing a new ML problem. Since every problem has unique characteristics, there is no universally optimal solution. Experimentation, supported by systematic hyperparameter tuning methods such as Bayesian Optimization [149], is a reliable approach to identifying the best configuration.

- **Activation functions:** In artificial neural networks, activation functions play a crucial role in converting input signals into corresponding output signals. In MLP, neurons can use different activation functions as long as they are non-linear. Here are he most common activation functions in MLP according to [150]:

  1. **Rectified Linear Unit (ReLU):** ReLU is computationally simple and efficient, allowing for faster training times compared to other activation functions due to its linear nature for positive inputs. It introduces sparsity in the network by activating only a subset of neurons at a time, which can lead

to improved performance and reduced overfitting [150, 151]. It can be defined as:

$$g(x) = max(x, 0), \tag{3.3.5}$$

2. **Exponential Linear Unit (ELU):** ELU speeds up the learning process in deep neural networks and enhances classification accuracy by pushing the mean activation closer to zero, reducing bias shifts during training [150, 151]. Mathematically, it can be expressed as:

$$g(x) = \begin{cases} x & \text{if } x > 0, \\ \alpha e^x - 1 & \text{if } x < 0, \end{cases} \tag{3.3.6}$$

3. **Scaled Exponential Linear Unit (SELU):** SELU automatically normalizes outputs to zero mean and unit variance when used with appropriate initializations, making it particularly effective for self-normalizing networks. The self-normalizing property helps maintain stability in the presence of noise and disturbances, improving overall network performance [150, 152]. It is defined as:

$$g(x) = k \cdot \textbf{ELU}(x, \alpha), \tag{3.3.7}$$

4. **Hyperbolic Tangent (Tanh):** Tanh outputs values between -1 and 1, making it zero-centered. This property helps in faster convergence during training as it mitigates issues related to bias shifts [153]. It is expressed as:

$$g(x) = \frac{e^x - e^{-x}}{e^x + e^{-x}}, \tag{3.3.8}$$

5. **Softsign:** Softsign is a smooth approximation of the sigmoid function and provides output values between -1 and 1. Its slopes help reduce issues like vanishing gradients compared to steeper activation functions. The smoothness of Softsign allows for better gradient flow during backpropagation (the method by which the network learns by adjusting the weights during training), which can enhance learning stability in certain scenarios [153]. It is defined mathematically as:

$$g(x) = \frac{x}{|x| + 1}, \tag{3.3.9}$$

k and α are scaling and shaping parameters, respectively.

- **Dropout rate:** Dropout is a method used to combat overfitting in neural networks. It works by randomly deactivating a subset of neurons in a given layer during training. This forces the network to learn more robust features, as it cannot rely on any single neuron.

- **Batch size:** is the number of samples processed together in a single iteration of model training. In other words, it defines how many samples the network evaluates before updating its weights.

3.4 Metrics for Classification Models

In classification problems, several key metrics are used to evaluate model performance, the confusion matrix, accuracy, sensitivity (Sens), and specificity (Spec) being among the most common.

- **The confusion matrix**: It summarizes the outcomes of a classification task and is defined in Table 3.4.1. The matrix includes the following components:
  - **True Positive (TP):** Uncontaminated cases correctly identified as uncontaminated.
  - **False Positive (FP):** Uncontaminated cases incorrectly classified as contaminated.
  - **False Negative (FN):** Contaminated cases incorrectly classified as uncontaminated.
  - **True Negative (TN):** Contaminated cases correctly identified as contaminated.

  In the case of classification between contaminated and uncontaminated food samples, the False Negative (FN) count is particularly significant, as it reflects failures in contaminant detection, which is a critical aspect of the system's performance.

Table 3.4.1: The confusion matrix.

	Positive	Negative
Positive	TP	FP
Negative	FN	TN

- **Accuracy**: Is defined as the percentage of correct predictions (TN and TP) out of all predictions. It is calculated using the following formula:

$$\text{Accuracy} = \frac{\text{TP} + \text{TN}}{\text{TP} + \text{TN} + \text{FP} + \text{FN}} \cdot 100 \tag{3.4.1}$$

- **Sensitivity**: Also known as the true positive rate, it is defined as the proportion of TP predictions out of all actual positive instances (TP and FN). It is particularly important when the FN is more critical, as in our application. Sensitivity is calculated as follows:

$$\text{Sensitivity} = \frac{\text{TP}}{\text{TP} + \text{FN}} \tag{3.4.2}$$

- **Specificity**: Also known as the true negative rate, it measures the proportion of actual negatives correctly identified, emphasizing the model's ability to avoid false positives. It is calculated as follows:

$$\text{Specificity} = \frac{\text{TN}}{\text{TN} + \text{FP}} \tag{3.4.3}$$

3.5 Principal Component Analysis (PCA)

Principal Component Analysis (PCA) [154] is a dimensionality reduction technique that provides valuable insights into the distribution and structure of a dataset. By transforming the original features into a new set of orthogonal components, PCA captures the maximum variance in the data using a smaller number of dimensions. This approach not only simplifies data visualization in lower-dimensional spaces but also highlights the most influential features in the dataset, represented by the principal eigenvectors [155]. In our application, PCA is not used for dimensionality reduction because we aim to train the ML algorithms on scattering parameters, including noise. Since our system is designed for

an industrial environment where noise cannot be controlled, preserving it is crucial. Instead, we utilize PCA to analyze and visualize the dataset's inherent structure, enabling better interpretation and guiding subsequent processing steps.

Consider a dataset M structured as a matrix with dimensions ($n_{samples}, n_{features}$), where each sample x is a vector of length $n_{features}$, representing the number of dimensions. Performing PCA involves four essential steps, as outlined in [156].

1. **Centering the data by subtracting the mean**: For each feature in every sample, subtract the mean of that feature across all samples in the dataset. The mean, denoted by μ_j, is computed for each feature j across all samples in the dataset M. This step transforms the dataset into a mean-centered version, denoted M′. Mathematically, this is expressed as:

$$x_{i,j} = x_{i,j} - \mu_j \quad \forall \mathrm{i} \in 1, 2, ..., n_{samples}, \quad \forall \mathrm{j} \in 1, 2, ..., n_{features} \tag{3.5.1}$$

where $x_{i,j}$ represents the j-th feature of the i-th sample, and $x_{i,j}$ is the j-th feature of the transformed i-th sample.

2. **Computing the covariance matrix**: If the dataset has more than two dimensions ($n_{features} \geq 2$), multiple covariance values are computed. These covariance values are organized into a matrix, where each entry (p, q) represents the covariance between dimensions p and q. This matrix is called the covariance matrix. The entry for a general dataset with $n_{features}$ dimensions is given by:

$$c_{p,q} = \mathrm{cov}(M_p, M_q) \quad \forall p, q \in 1, 2, ..., n_{features} \tag{3.5.2}$$

where M_p and M_q are the p-th and q-th column vectors of the dataset M, each with length equal to $n_{samples}$. The covariance between two dimensions is computed as:

$$\mathrm{cov}(M_p, M_q) = \frac{1}{n_{samples} - 1} \sum_{i=1}^{n_{samples}} \left(M_p - \overline{M_p}\right)\left(M_q - \overline{M_q}\right) \tag{3.5.3}$$

where $\overline{M_p}$ and $\overline{M_q}$ are the mean values of the respective columns.

3. **Construct the feature vector**: The eigenvectors and eigenvalues of the covariance matrix are computed. These eigenvectors are then sorted in descending order based on their corresponding eigenvalues. The sorted eigenvectors are arranged into a matrix, referred to as the feature vector ($\mathrm{F_V}$):

$$\mathrm{F_V} = (\mathrm{eig}_1, \mathrm{eig}_2, ..., \mathrm{eig}_{n_{features}}) \tag{3.5.4}$$

To reduce the dimensionality of the dataset, only the eigenvectors corresponding to the largest eigenvalues are retained. These eigenvectors are known as the principal components, as they capture the majority of the dataset's information. Although this process results in some information loss, the smaller the eigenvalues of the discarded eigenvectors, the less information is lost. Therefore, the resulting feature vector is:

$$\mathrm{F'_V} = (\mathrm{eig}_1, \mathrm{eig}_2, ..., \mathrm{eig}_{n_{principal\ components}}) \tag{3.5.5}$$

where $n_{principal\ components} \leq n_{features}$.

4. **Obtain the reduced dataset**: The centered dataset M′ (with dimensions $n_{samples}, n_{features}$) is

projected onto a lower-dimensional space M″ (with dimensions $n_{samples}$, $n_{principal\ components}$) using the following truncated transformation:

$$M'' = M' \cdot F'_V \tag{3.5.6}$$

The principal components become the axes of the new dataset, ensuring they are uncorrelated with the original dimensions. In this study, PCA is utilized to visualize high-dimensional data in a 3D space by selecting only the first three principal components. Examples of these representations will be presented in the results chapter.

3.6 Grey-Wolf Optimization (GWO) Method

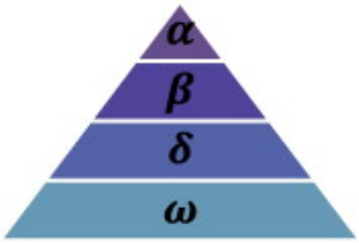

Figure 3.6.1: Grey wolf hierarchy (dominance decreases from top to bottom) [157].

The performance of SVM and MLP algorithms in machine learning applications relies on properly tuning their hyperparameters. Manually searching for optimal values is time-consuming, as it requires repeatedly adjusting parameters such as (C^*, γ^*) in SVM or the number of neurons in MLP while evaluating the results. Therefore, employing optimization methods is essential. In this thesis, the Grey Wolf Optimizer (GWO) is used to optimize the hyperparameters of SVM and MLP. The objective is to minimize the validation error and improve classification accuracy on the test set. For SVM, the optimization targets the hyperparameter pair (C^* and γ^*), while for MLP, it focuses on determining the optimal number of neurons in the hidden layers.

The Grey Wolf Optimizer (GWO) [157] is a bio-inspired optimization algorithm modeled on the social behavior of grey wolves during hunting. Grey wolves typically live in packs of 5 to 12 individuals, characterized by a strict social hierarchy, as illustrated in Figure 3.6.1. The leaders, referred to as alphas (α), can be either male or female. The alpha is responsible for the pack, making major decisions on matters such as hunting, sleeping locations, and wake-up times. While the alpha is not necessarily the strongest wolf, it is the one that leads and guides the pack. The beta (β) wolf serves as the second-in-command, subordinate to the alpha. Its role is to support and reinforce the alpha's decisions while also providing advice. The beta is usually the successor to the alpha when the latter dies or grows old. The beta must respect the alpha while also managing wolves of lower ranks.

At the lowest rank are the omega (ω) wolves. Omegas are submissive to all higher-ranking wolves but play an important role in the pack. They contribute by monitoring and protecting the pack, particularly during attacks. Wolves that are neither α, β, nor omegas ω are called deltas (δ). These wolves are subordinate to the alphas and betas but hold dominance over the omegas. The delta group includes different roles essential to the pack's survival and organization. Scouts monitor the territory's boundaries

and alert the pack to potential dangers, while sentinels protect and ensure the pack's safety. Elders, often experienced wolves who were once alphas or betas, contribute their knowledge to the group. Hunters support the alphas and betas by assisting in hunting and providing food for the pack, and caretakers look after the weaker, sick, and injured wolves, ensuring the well-being of all members.

Figure 3.6.2: Wolves' behavior during hunting [157]: A. Chasing and closing in on the prey. B – D. Surrounding the prey. E. Attacking stage.

The GWO method is inspired by the hunting behavior of grey wolves, which consists of three stages, as illustrated in Figure 3.6.2: chasing and approaching the prey, surrounding the prey, and finally attacking the prey. In this context, the prey are the global minimum or maximum. These stages are divided into two primary phases: the exploration phase (stage 1) and the exploitation phase (stages 2 and 3). Let us consider a scenario where P parameters, denoted as $K_1, K_2, \ldots, K_P$, need to be optimized, with $P \geq 1$. The following notations are defined for clarity:

- P: the total number of parameters to be optimized.
- t: the current iteration, and T_{max} represents the maximum number of iterations.
- $f()$: denotes the objective function to be minimized, which is dependent on P.
- $x_q(t)$: the position of a search agent (wolf) at iteration t.
- $x_\alpha(t), x_\beta(t), x_\delta(t)$: the positions of the alpha (α), beta (β), and delta (δ) wolves, respectively, at iteration t.

This notation establishes the foundation for describing the optimization process in the GWO algorithm. In the mathematical representation, the alpha wolf (α) corresponds to the best solution found so far, while the beta wolf (β) and delta wolf (δ) represent the second- and third-best solutions, respectively. During the hunting process, the wolves are directed by the alpha wolf (α) to locate the prey. To mathematically model the behavior of grey wolves during hunting, the positions of α, β, and δ being the best solutions, are used to guide the remaining wolves (the ωs). The omega wolves update their positions based on the locations of the leaders. The position of a search agent at iteration $(t + 1)$ is computed as follows:

$$x_q(t+1) = \frac{1}{3}\left(y_\alpha(t) + y_\beta(t) + y_\delta(t)\right), \tag{3.6.1}$$

where Equation 3.6.1 represents the combined effect of the positions of the alpha, beta, and delta wolves on the position of the search agent x_q. The contributions of each leader, $l \in \{\alpha, \beta, \delta\}$, are calculated at each iteration as:

$$y_l(t) = x_l(t) - bd_l, \tag{3.6.2}$$

where $d_l = \left|cx_l(t) - x_q(t)\right|$, and $|\cdot|$ denotes the absolute value. The vectors b and c are defined as: $b = 2ar_1 - a$, and $c = 2r_2$.

In these expressions, r_1 and r_2 are vectors with randomly generated components within the range $[0, 1]$, and a is a key parameter defined in Equation 3.6.6. For the i-th parameter ($i = 1, \ldots, P$): the i-th component of b is given by:

$$b^i = 2ar_1 - a \tag{3.6.3}$$

while the i-th component of $d_l(t)$ is given by:

$$d_l^i(t) = \left|2r_2 x_l^i - x_q^i(t)\right|, \tag{3.6.4}$$

where $x_q^i(t)$ represents the i-th component of agent q at iteration t, and x_l^i denotes the i-th component of the leader l.

The i-th component of $y_l(t)$ is computed as:

$$y_l^i(t) = x_l^i - b^i d_l^i(t), \tag{3.6.5}$$

where b^i is the i-th power component of vector b, and $d_l^i(t)$ is the i-th power component of $d_l(t)$.

The value of a, defined as:

$$a = 2\left(1 - \frac{\mathrm{t}}{T_{\max}}\right), \tag{3.6.6}$$

is a critical parameter in the GWO algorithm. It regulates the transition between exploration ($a \geq 1$) and exploitation ($a \leq 1$). During exploration, wolves disperse and search the solution space, while during exploitation, they converge toward the prey (global optimum). Figure 3.6.3 illustrates the updates in the positions of the leaders α, β, and δ within a 2D search space.

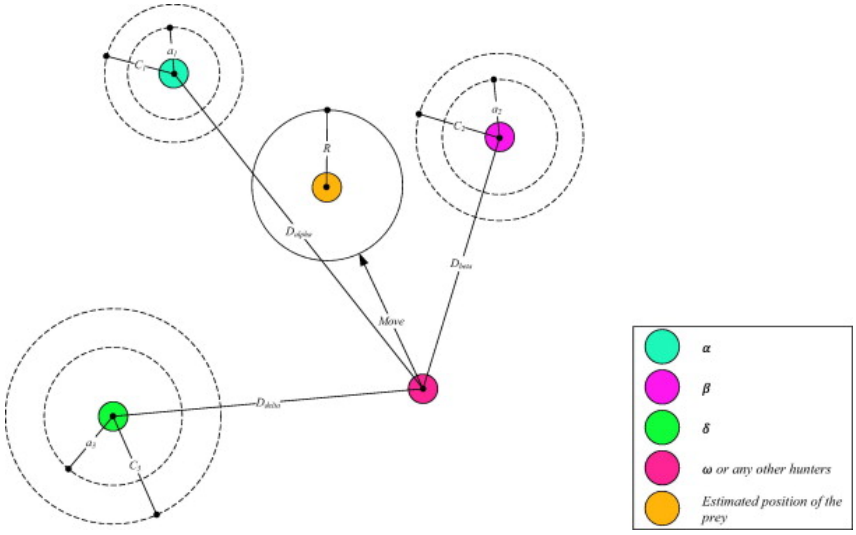

Figure 3.6.3: Positions updating of the search agents [157]

GWO is used to optimize the hyperparameters of SVM and MLP in similar applications, as demonstrated in [103, 104] for SVM and in [140] for MLP. These studies show successful results, which is why we choose to apply GWO in our work. The optimized parameter values, along with their corresponding validation results, will be presented in the results chapter. Additionally, the implementation details of the GWO method are discussed following the procedures outlined in [140, 158].

4 Experimental Results

4.1 The measurement procedure

In Chapter 2, we provided a detailed overview of the system. In this section, we will focus on the measurement procedure using the MW sensing system. For the measurements, we use food jars that are made of plastic and have the same dimensions as those described in Chapter 2. As mentioned earlier, the jars are standard commercial products with an elliptical cylindrical shape, as shown in Figure 4.1.1(a), with a minor axis of 6.6 cm, a major axis of 7.5 cm, and a height of 10.5 cm. The contaminants, on the other hand, are spherical with a diameter of 4 mm, as illustrated in Figure 4.1.1(b). We focus on using plastic and glass as contaminants, as they are the most commonly used materials during various production stages. Moreover, these materials are particularly relevant because they are the same as packaging materials, plastic and glass being the most widely used in the food industry, and are especially challenging to detect with other systems.

We adopt similar methodology for conducting measurements across all subsequent results. Four plastic jars, identical in shape and dimensions to the one shown in Figure 4.1.1(a), are used. Among these, two jars are randomly selected to be used as uncontaminated samples, while the other two are deliberately contaminated with different materials. The measurement process begins as a jar, transported by the conveyor belt, enters the active zone of the antenna array. The antennas sequentially emit signals while simultaneously receiving scattered signals as the jar moves. This setup facilitates the acquisition of data from multiple positions of the jar across various frequency points.

4.2 Measurement Settings

Once the operating frequency bands of interest are identified, the next step involves defining the number of frequency points within these bands. Taking into account the conveyor belt speed of 33 cm/s and the maximum allowable acquisition time for measuring a single food sample, which is approximately 50 ms, denoted as Δt_{total} in Figure 4.2.1, the number of frequency points are determined. The total acquisition time, represented as Δt_{total} in Figure 4.2.1, is the period required by the MW sensing system, specifically the VNA to generate and collect back the data through the arc shaped six antennas from testing a single sample. This period includes the measurement initiation time and six frequency ramp Δt_f periods. Each Δt_f period represents the time required for the frequency to gradually increase from the minimum to the maximum within the selected frequency band. In addition, it includes five Δt_{switch} periods, corresponding to the switching time between the six transmitting antennas, as well as the time allocated

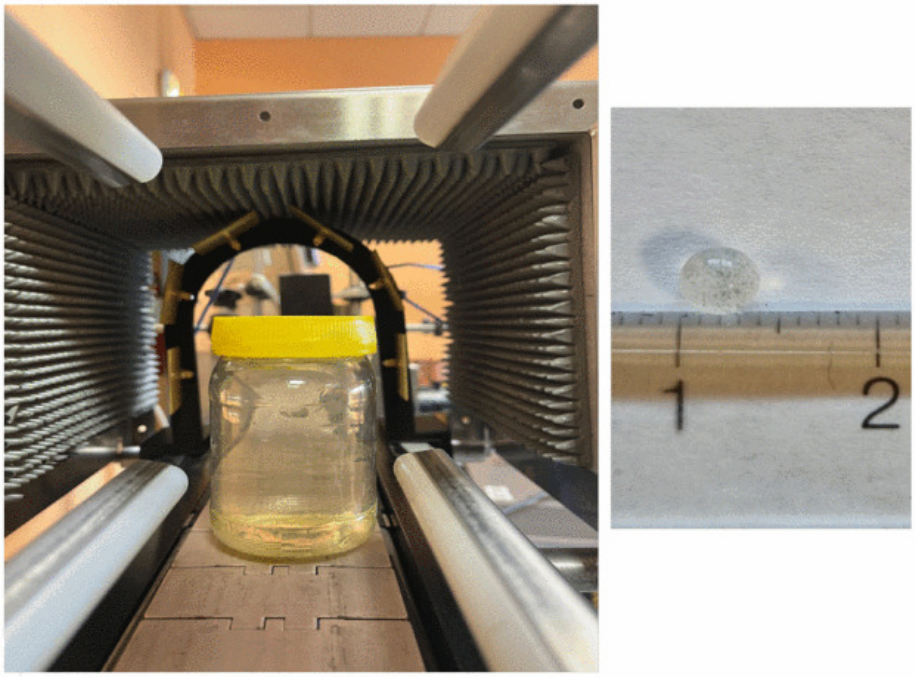

Figure 4.1.1: (a) The MW sensing system setup, (b) Dimensions of the contaminants used [159].

for data collection. In this context, selecting the number of frequency points involves balancing the need for frequency diversity in the measurements with the time constraints imposed by the moving jar on the conveyor belt. Increasing the number of frequency points offers more detailed information but may extend the measurement time, potentially rendering the process impractical. The value of Δt_f is defined as:

$$\Delta t_f = N_f \cdot t_{IF}, \tag{4.2.1}$$

Here, N_f represents the number of frequency points, while t_{IF} denotes the time required by the VNA to sweep through the specified frequency range and collect data at each frequency point. t_{IF}, is inversely proportional to the Intermediate Frequency (IF) filter setting of the VNA. A smaller IF value is desirable for achieving low-noise measurements. However, reducing IF increases t_{IF}, necessitating a smaller number of frequency points (N_f) to maintain feasible measurement times. Based on this analysis, we determined that recording data at N_f = 11 frequency points across the two frequency bands with IF = 1 kHz meets our requirements effectively.

In our application, as discussed in Chapter 2, we have selected two frequency bands to address two types of food and beverage products: oil-based products (from 6 to 10 GHz) and water-based products (from 1.5 to 3.5 GHz). To obtain 11 frequency points across these two bands, the frequency step must be defined for each. A 200 MHz step is applied in the 1.5 GHz to 3.5 GHz range, while a 400 MHz step is used in the 6 GHz to 10 GHz range.

In Figure 4.2.1, the transition between antennas (Tx_i), with i representing the antenna index, occurs after the preceding antenna has completed its operation across the 11 frequencies within the bands.

Each time an antenna radiates, the remaining five antennas, along with the radiating antenna, receive the scattered waves. After each acquisition, we obtain a set of 11 matrices, corresponding to the 11 frequency points, each containing 36 scattering parameters. These matrices provide important information about the condition of the food product being tested. Additionally, it is important to note that during the measurements, the jar is in motion as the antenna transitions and frequency sweeping occurs. Consequently, the resulting matrices are not symmetrical, as the jar's dynamic movement causes variations in the scattering behavior of the microwaves.

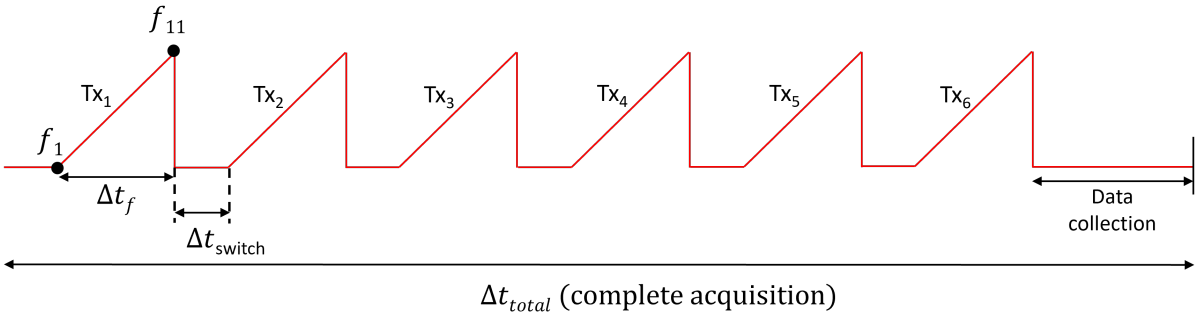

Figure 4.2.1: Time frame for a complete data acquisition (single measurement) [111].

4.3 Dataset Construction

To generate the datasets, we conduct multiple measurement repetitions, as detailed in Table 4.3.1, totaling hundreds of reading for each specific case. To enhance the robustness of our results, we employ various data collection scenarios, including performing measurements on different days, alternating between contaminated and uncontaminated jars, and slightly rotating the jar before each measurement. These conditions are considered to simulate real-world scenarios, where product samples are tested in-line in an industrial environment.

Scenarios	Water jar	Oil jar
No contaminants	300	230
PTFE	100	130
SLG	100	130

Table 4.3.1: The number of measurements performed on oil and water jar samples with different types of contaminants.

We implement an externally triggered script to regulate the parameters required for our measurements, such as the frequency bands, the number of frequency points, the number of measurements, the spacing between the initial position of the jar and the antenna array, and the Intermediate Frequency (IF) of the VNA. This configuration facilitates the continuous execution of hundreds of measurements without any interruption while sequentially capturing the scattering matrices. The measurement process begins when the jar interrupts the light reaching a photocell positioned alongside the conveyor belt. This photocell acts as a trigger, signaling the start of measurements as the jar enters the effective radiated region of the antenna array. Each measurement produces one matrix per frequency point, with dimensions 6×6. Data

are then reorganized into 2D matrices of size 36×11, , where each column contains the unwrapped 6×6 matrix of S-parameters measured at a single frequency. The 2D matrices are represented as follows:

$$[S_n^{\mathbb{C}}] = \begin{bmatrix} S_{11,n}^{f_1} & S_{11,n}^{f_2} & \cdots & \cdots & S_{11,n}^{f_{10}} & S_{11,n}^{f_{11}} \\ S_{12,n}^{f_1} & S_{12,n}^{f_2} & \cdots & \cdots & S_{12,n}^{f_{10}} & S_{12,n}^{f_{11}} \\ \vdots & \vdots & \vdots & \vdots & \vdots & \vdots \\ S_{16,n}^{f_1} & S_{16,n}^{f_2} & \cdots & \cdots & S_{16,n}^{f_{10}} & S_{16,n}^{f_{11}} \\ S_{21,n}^{f_1} & S_{21,n}^{f_2} & \cdots & \cdots & S_{21,n}^{f_{10}} & S_{21,n}^{f_{11}} \\ \vdots & \vdots & \vdots & \vdots & \vdots & \vdots \\ S_{26,n}^{f_1} & S_{26,n}^{f_2} & \cdots & \cdots & S_{26,n}^{f_{10}} & S_{26,n}^{f_{11}} \\ \vdots & \vdots & \vdots & \vdots & \vdots & \vdots \\ \vdots & \vdots & \vdots & \vdots & \vdots & \vdots \\ S_{66,n}^{f_1} & S_{66,n}^{f_2} & \cdots & \cdots & S_{11,n}^{f_{10}} & S_{66,n}^{f_{11}} \end{bmatrix} \tag{4.3.1}$$

Each element $S_{ij,n}^{f_m}$ represents a complex number, where n indicates the index of the measurement sample, i and j correspond to the receiving and radiating antennas, respectively, and f_m (with $m = 1, \ldots, 11$) represents the 11 frequency points. Based on Equation 4.3.1, the following vectors are derived for each frequency f_m:

$$[S_n^{A,f_m}] = \left[|S_{11,n}^{f_m}| \quad \cdots \quad |S_{16,n}^{f_m}| \quad |S_{21,n}^{f_m}| \quad \cdots \quad |S_{26,n}^{f_m}| \quad \cdots \quad \cdots \quad |S_{61,n}^{f_m}| \quad |S_{66,n}^{f_m}| \right]^T \tag{4.3.2}$$

$$[S_n^{f_m}] = \left[\mathcal{R}(S_{11,n}^{f_m})\mathcal{I}(S_{11,n}^{f_m}) \cdots \mathcal{R}(S_{16,n}^{f_m})\mathcal{I}(S_{16,n}^{f_m}) \cdots \mathcal{R}(S_{61,n}^{f_m})\mathcal{I}(S_{61,n}^{f_m}) \cdots \mathcal{R}(S_{66,n}^{f_m})\mathcal{I}(S_{66,n}^{f_m}) \right]^T \tag{4.3.3}$$

In Equation 4.3.2, A represents the amplitude of the measured scattering parameters, while Equation 4.3.3 separates these parameters into their real and imaginary components. By combining the 11 vectors corresponding to the 11 frequency points, we derive the following vectors:

$$[S_n^A] = \left[[S_n^{A,f_1}] \quad [S_n^{A,f_2}] \quad \cdots \quad \cdots \quad \cdots \quad [S_n^{A,f_{11}}] \right]^T \tag{4.3.4}$$

$$[S_n] = \left[[S_n^{f_1}] \quad [S_n^{f_2}] \quad \cdots \quad \cdots \quad \cdots \quad [S_n^{f_{11}}] \right]^T \tag{4.3.5}$$

These vectors include all the extracted scattering parameters for a sample under test. Each vector contains either 396 entries for amplitude-only data or 792 entries when incorporating the real and imaginary parts of the scattering parameters. Using these vectors, we construct the necessary datasets for both training and testing by compiling the complete set of vectors corresponding to all measurement samples, as outlined below:

$$[S^A] = \left[[S_1^A] \quad [S_2^A] \quad \cdots \quad \cdots \quad \cdots \quad [S_N^A] \right] \tag{4.3.6}$$

$$[S] = \left[[S_1] \quad [S_2] \quad \cdots \quad \cdots \quad \cdots \quad [S_N] \right] \tag{4.3.7}$$

Here, N denotes the total number of measurements performed.

4.4 First Contribution

In this contribution, we utilize the measurement data from [160] to classify oil-based food jars as either contaminated or uncontaminated, incorporating several enhancements and modifications to the methodology presented in [160]. In the original work, the author uses an MLP classifier alongside a microwave sensing system, shown in Figure 4.4.1, to detect contamination in jars filled with oil. Building on this foundation, we aim to enhance the results in three key ways. First, we investigate the use of the SVM algorithm as an alternative to MLP. Second, we optimize the performance of both classifiers using the Grey Wolf Optimizer (GWO). Lastly, we construct different types of datasets—one using the complex numbers of the scattering parameters and another using amplitude-only data of the same scattering parameters and retrain both machine learning algorithms on these datasets to improve their effectiveness. The amplitude-only [161] approach is particularly practical, as capturing only the magnitude simplifies the measurement setup, potentially making the system more compact and suitable for industrial applications.

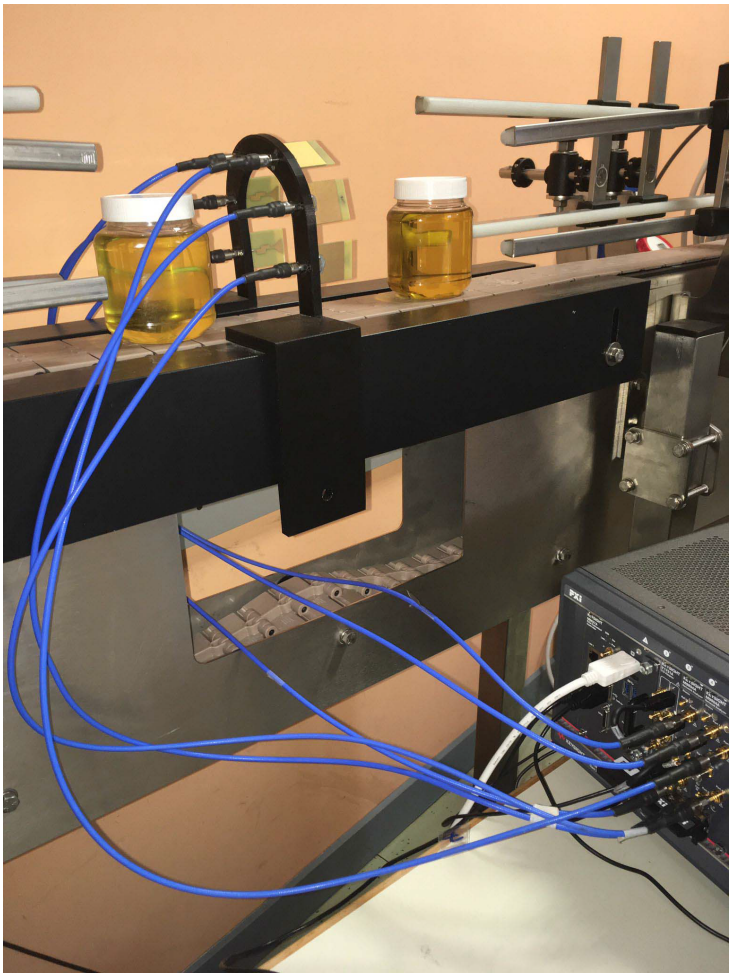

Figure 4.4.1: Microwave sensing system used in [160]

The measurement system used to collect data for this study is detailed in [160]. It represents an

earlier version of the system introduced in Chapter 2 of this thesis and is shown in Figure 4.4.1. These antennas are set to operate within a frequency range of 9 to 11 GHz, with the frequency of interest centered at 10 GHz. Measurements are conducted across this frequency range using a step size of 200 MHz, resulting in 11 frequency points. The measurements follow the same procedure outlined in the measurement procedure section of this chapter. However, beyond PTFE and SLG, the authors expand the scope of contaminants to include additional materials, such as glass fragments, wood, plastic, and metals, providing a broader dataset for analysis. A set of jars filled with oil is prepared, some containing contaminants and others without.

In this study, the datasets are constructed in the same way as described in the dataset construction section of the current chapter. The only difference is the exclusion of the reflection coefficients (S_{ii}), ensuring consistency with the data type used in [160] for comparison purposes. By excluding the S_{ii}, the resulting dataset consists of matrices with dimensions 30×11 for the amplitude-only data and $30 \times 11 \times 2$ for the real-imaginary data for each sample under test.

Before analyzing the classification results, it is essential to examine the type of data being used in the datasets construction. To do this, we created two images based on the magnitude of the retrieved S-parameters for various samples exposed to the microwave sensing system in this study. Figure 4.4.2 displays the plots of the complete elements of matrices, each with dimensions 30×11, representing the amplitude-only data from the measurements. The two images correspond to two jar samples: one uncontaminated and the other contaminated. A variation in amplitude values between the two cases can be observed at different frequencies, highlighted by the black circles in Figure 4.4.2. While the images contain valuable information, it is insufficient for humans to reliably determine whether a sample is contaminated or uncontaminated just by looking to the image. Additionally, there is uncertainty in the scattering matrices due to the dynamic nature of the measurement conditions. This variability arises from four factors: the type, size, and position of the intrusion within the jar, as well as the movement of the jar on a conveyor belt. Given these challenges, using machine learning (ML) algorithms to automate the classification process is not only necessary but also highly effective for handling such dynamic and variable conditions.

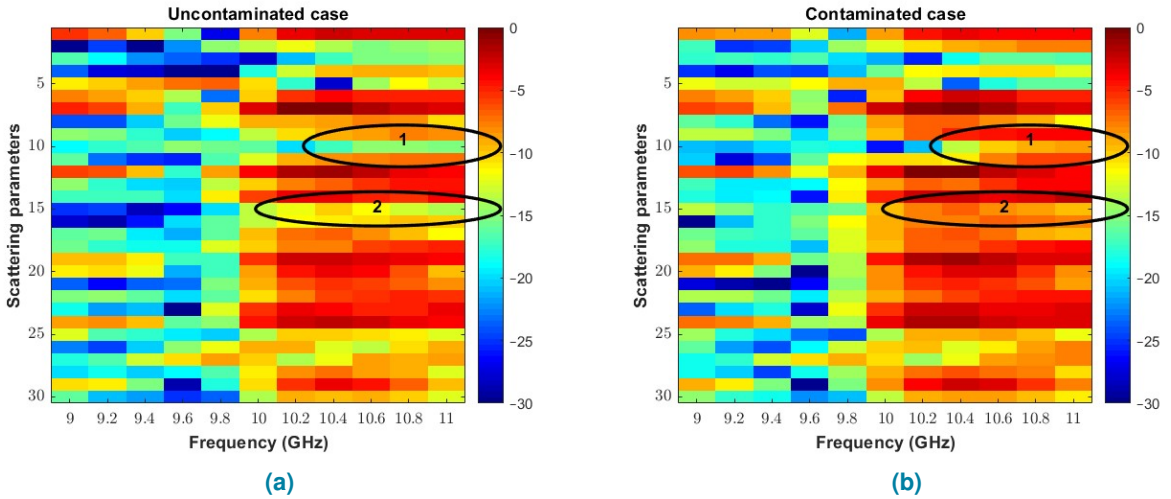

Figure 4.4.2: The normalized amplitude plots of the retrieved S-parameters for two test samples: (a) an uncontaminated jar sample; (b) a contaminated jar sample.

Another interesting analysis conducted on the training dataset is the Principal Component Analysis (PCA), which enables us to visualize the data distribution, as shown in Figure 4.4.3. The figures illustrate how the two constructed datasets are projected onto the three most significant eigenvectors. These three components capture 70% of the variance, effectively representing the main patterns in the data. The Red circles represent contaminated samples, while the green circles correspond to uncontaminated samples. The figures reveal that the data are overlapping and non-linearly separable in both datasets, making the choice of a non-linear ML model essential for effective class separation.

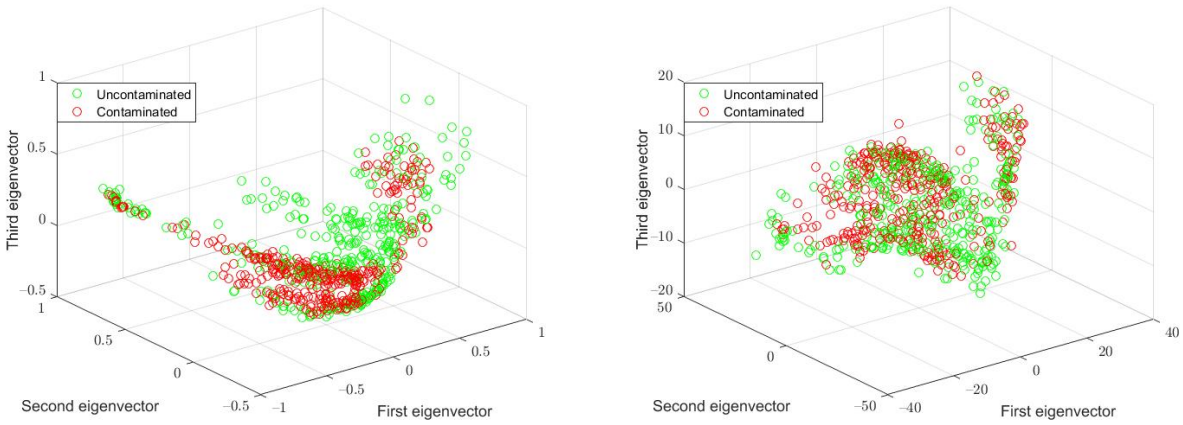

Figure 4.4.3: Data distribution projected onto the three most significant eigenvectors [162]: (a) Complex dataset with real and imaginary components, (b) Amplitude-only dataset.

4.4.1 Classification Results

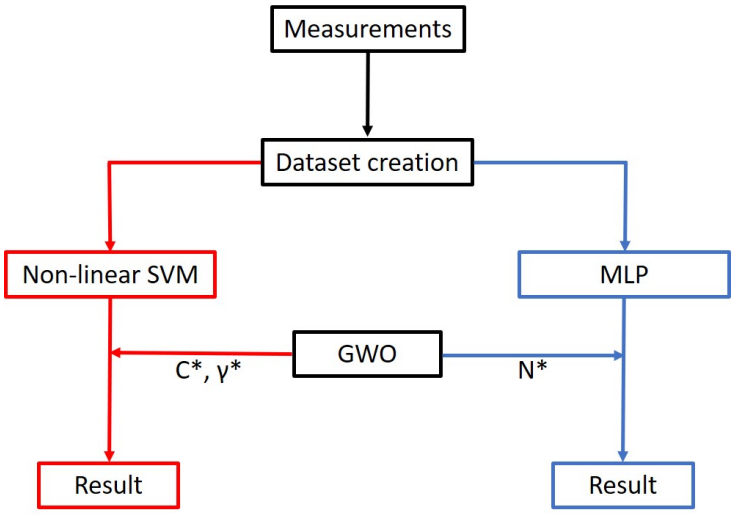

Figure 4.4.4: Workflow [162]

After completing the measurements, we follow the workflow shown in Figure 4.4.4 for classification. The complete dataset consists of 1240 samples, which are divided as follows: 58% (720 samples)

for the development set(training and validation) and 42% (520 samples) for the test set, as shown in Table 4.4.1. Maintaining a balanced number of contaminated and uncontaminated samples in the training set is necessary. Furthermore, the contaminated class should include an equal number of samples from each type of contamination. To construct our training dataset, we randomly select 360 samples from the uncontaminated class and 60 samples from each of the six contaminated classes, as outlined in Table 4.4.1. The training data are labeled as +1 for uncontaminated cases and -1 for contaminated cases. The development set is further divided into 90% (648 samples) for training and 10% (72 samples) for validation. This study aims to compare the accuracy of two different machine learning algorithms trained on two distinct types of datasets, as previously explained: dataset includes the real and imaginary components of the scattering parameters or their amplitude only. Additionally, using the Grey Wolf Optimizer (GWO) to determine the optimal number of neurons (N^*) for a single-hidden-layer MLP model in our approach allows us to compare its performance with that of an MLP model where the parameters are manually chosen in [160]. Consequently, each classifier produces two sets of results, one for each dataset type. With both classifiers implemented, we obtain four groups of results.

Table 4.4.1: The number of samples from each class used for the training and testing phases.

Classes	Number of samples used for training	Number of samples used for test
Uncontaminated	360	240
Contaminated with small splinter of Glass	60	60
Contaminated with Metal	60	40
Contaminated with small splinter of Plastic	60	60
Contaminated with PTFE (4 mm sphere)	60	40
Contaminated with SLG (4 mm sphere)	60	40
Contaminated with fragment of wood	60	40

We evaluate the performance of the classifiers based on two criteria. First, we ensure that the model's performance is independent of specific data subsets by varying the training and test samples. Second, we assess the stability of the model within each training, verifying whether it produces consistent results or fluctuates significantly across different runs. To achieve this, we train the two classifiers 10 times, randomly selecting new training and test samples for each run. The hyperparameters are optimized using the Grey Wolf Optimizer (GWO) only in the first training, and the same values are retained for all subsequent trainings. If the classifier model maintains consistent performance across multiple trainings with the same optimized hyperparameters, it indicates stability, good generalization, and low sensitivity to training data variations, suggesting well-tuned hyperparameters. Additionally, each trained model is tested 10 times to further verify stability, resulting in a total of 100 confusion matrices.

Classification Results for the Amplitude-Only Dataset

Table 4.4.2 presents the average validation results over 10 training runs for both classifiers on the amplitude-only dataset. It also includes the optimal parameter values for each algorithm, as determined by GWO for a single training. The validation accuracy reaches an ideal 100% with the non-linear SVM algorithm, while it is slightly lower with the MLP classifier, around 98.6%. This discrepancy between the two algorithms is expected due to the distinct mathematical approaches each employs to solve the

classification problem. It is worth noting that when repeating the training process with the MLP algorithm, the validation accuracy fluctuates between 98% and 100%. This variability arises because the MLP algorithm initializes with random weights connecting the layers during each run. In contrast, the SVM algorithm operates under more stable conditions, leading to consistent results across runs (iterations). Finally, another key aspect to consider is the training time, which highlights how long each algorithm takes to complete the training process and validate its performance on the training dataset.

Table 4.4.2: The optimum pair (C*,γ*) for the non-linear SVM and the optimal number of neurons (N*) for the single-hidden-layer MLP model, training times, confusion matrices, and the average validation accuracy for the two ML algorithms trained on the amplitude-only dataset.

Algorithm	Optimal Parameters	Training Time (s)	Confusion Matrix	Accuracy (%)
Non-linear SVM	(C^*, γ^*) $(2056177868, 2\times 10^{-4})$	0.01	$\begin{pmatrix} 38 & 0 \\ 0 & 34 \end{pmatrix}$	100
MLP	$(N^* = 11)$	0.2	$\begin{pmatrix} 37 & 1 \\ 0 & 34 \end{pmatrix}$	98.6

For each machine learning algorithm, the results are illustrated using three distinct curves. The first two curves show the correctly and incorrectly classified samples when all contaminated samples are grouped as a single class along with the uncontaminated ones (Figures 4.4.5 and 4.4.6). The third curve focuses on the misclassified samples for each contaminated class individually (Figures 4.4.7 and 4.4.8). Additionally, we calculate the average classification accuracy across the six contaminated classes and highlighted the most challenging cases encountered by each classifier. Certain test cases pose significant challenges, particularly those involving contaminants with dielectric properties closely matching the oil medium's permittivity.

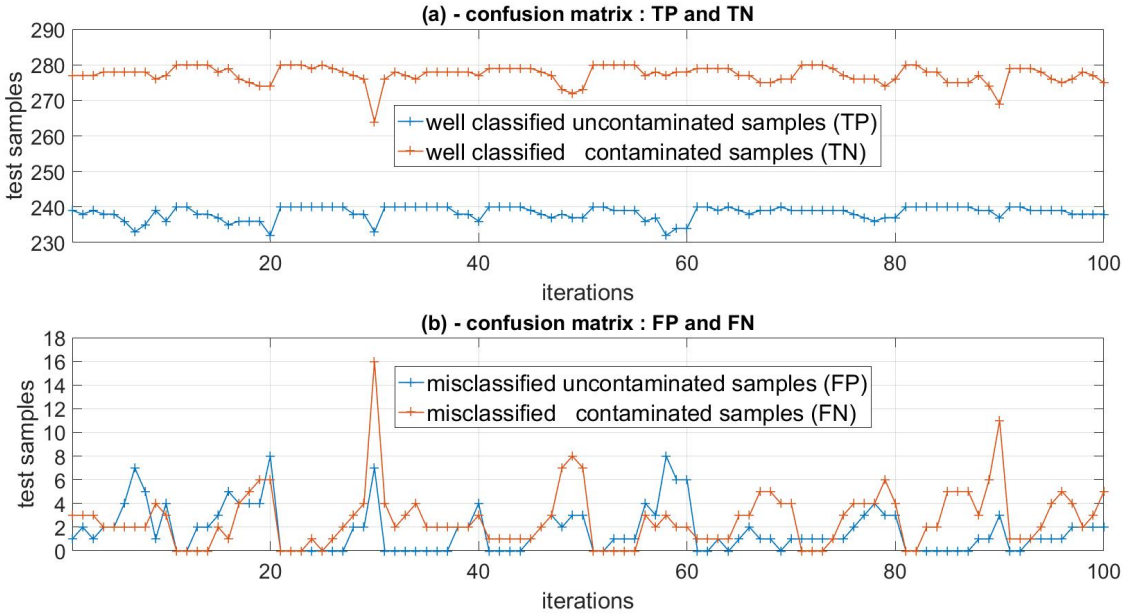

Figure 4.4.5: Confusion matrices from the non-linear SVM classifier trained on the Amplitude-only dataset: (a) displays the correctly classified terms (TP and TN), while (b) illustrates the misclassified terms (FP and FN) [162].

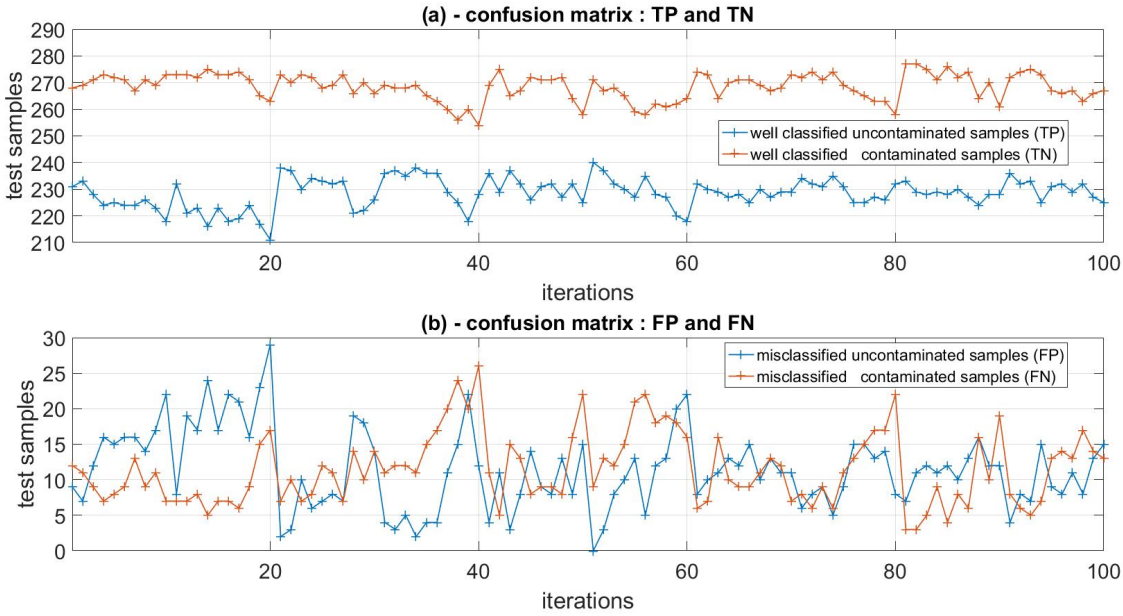

Figure 4.4.6: Confusion matrices from the MLP classifier trained on the Amplitude-only dataset: (a) depicts the correctly classified terms (TP and TN), while (b) represents the misclassified terms (FP and FN) [162].

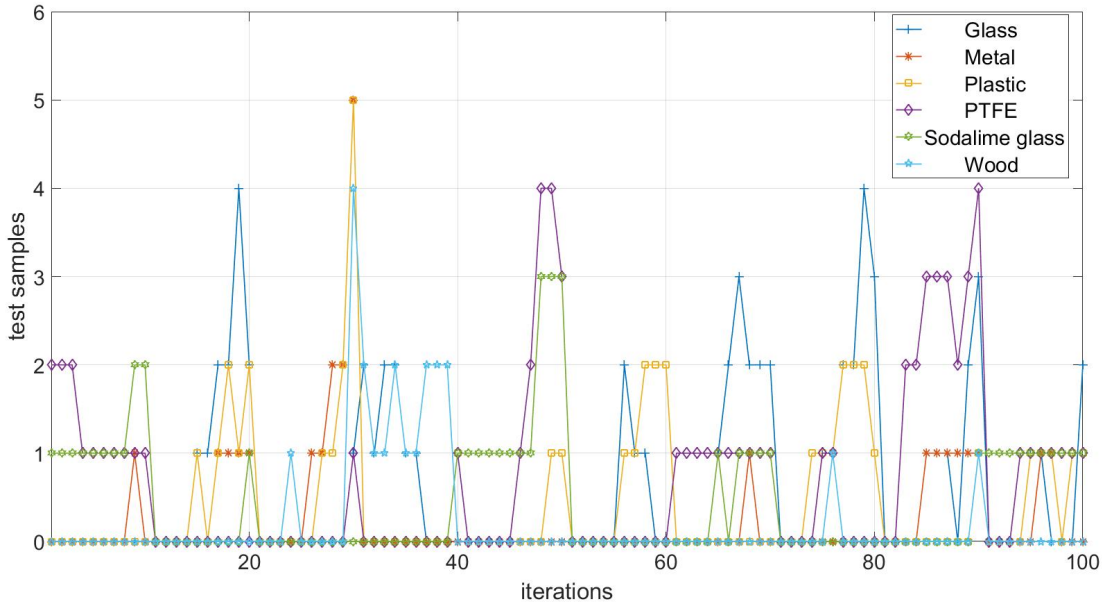

Figure 4.4.7: Plot of misclassified terms (FP and FN) from the confusion matrices for each contaminated class, based on the results obtained from the non-linear SVM algorithm trained on the Magnitude-only dataset [162].

The classification results for both machine learning algorithms are highly satisfactory, with the non-linear SVM classifier demonstrating a clear advantage. This superior performance is evident in the confusion matrix curves shown in Figures 4.4.5–4.4.8 and is summarized in Table 4.4.3. The overall

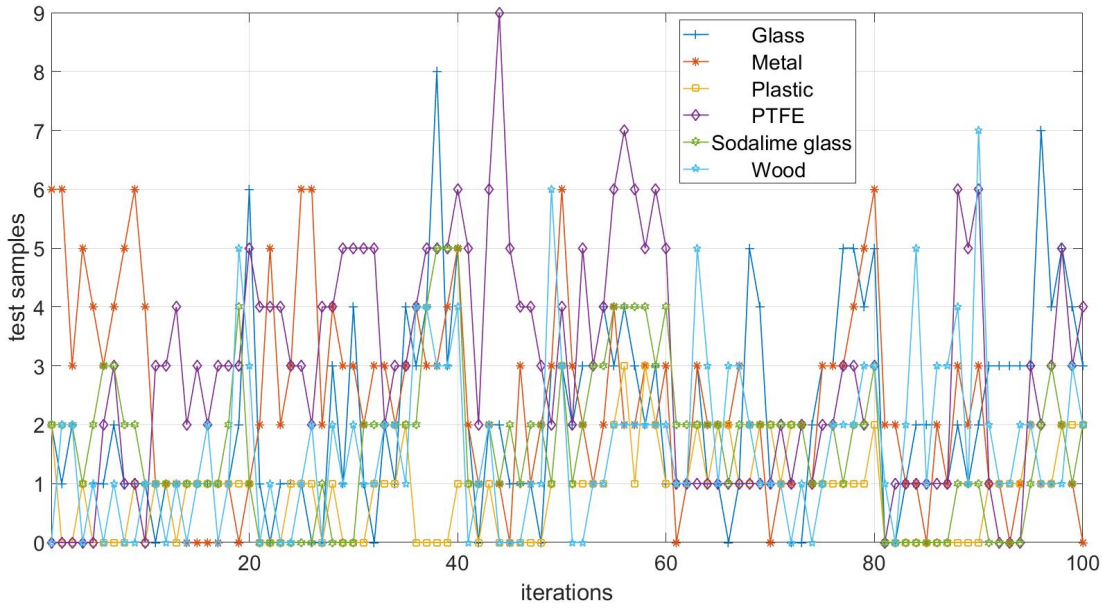

Figure 4.4.8: Plot of misclassified terms (FP and FN) from the confusion matrices for each contaminated class, based on the results obtained from the MLP algorithm trained on the Magnitude-only dataset [162].

accuracy achieved by the two algorithms was 95.6% for MLP and 99.2% for the non-linear SVM. While neural networks like MLP are effective for handling complex datasets, in this binary classification task with a relatively small training dataset, SVM proves to be a more suitable choice due to its strong generalization ability with limited data.

Table 4.4.3: Average classification accuracy per class for both classifiers on the magnitude-only dataset.

Classes	Accuracy with SVM (%)	Accuracy with MLP (%)
Uncontaminated	93.3	95.2
Contaminated with small splinter of Glass	99	96.5
Contaminated with Metal	99.3	94
Contaminated with small splinter of Plastic	99.3	98.5
Contaminated with PTFE (4 mm sphere)	98.2	92.8
Contaminated with SLG (4 mm sphere)	98.9	95.9
Contaminated with fragment of wood	99.5	96

In Table 4.4.3 and later in Table 4.4.5, we present the classification accuracy for each class for both classifiers. This is calculated by dividing the number of correctly classified samples within each class by the total number of samples in that class. As shown in Table 4.4.3, the highest error rate in the classification results occurred for jars contaminated with PTFE material, which consists of a small 4 mm diameter sphere that sinks to the bottom of the jar. To minimize classification errors across all classes, particularly for this critical case, we use the complex numbers dataset (real – imag), which contains comprehensive information about the samples under test. We anticipate that including both the real and imaginary components in the dataset will improve the results.

Classification Results for the Complex Numbers Dataset

Using a dataset that includes the real and the imaginary parts of the scattering parameters instead of the amplitude-only dataset is expected to improve classifier performance, as it provides additional information for training. Following the same approach used to present the results for the amplitude-only dataset, we will now detail the validation and test outcomes. Table 4.4.4 presents the GWO results, validation accuracy, and the training time required for each algorithm using the new dataset.

Table 4.4.4: The optimum pair (C*,γ*) for the non-linear SVM and the optimal number of neurons (N*) (optimal number of neurons) for the single-hidden-layer MLP model. Training time, confusion matrices, and accuracy obtained on the validation set for the two different ML algorithms trained with the Complex nature dataset.

Algorithm	Optimal Parameters	Training Time (s)	Confusion Matrix	Accuracy (%)
Non-linear SVM	(C^*, γ^*) (3400529630, 3×10^{-4})	0.01	$\begin{pmatrix} 41 & 0 \\ 0 & 31 \end{pmatrix}$	100
MLP	(N^* = 11)	0.4	$\begin{pmatrix} 40 & 0 \\ 0 & 32 \end{pmatrix}$	100

Both algorithms achieved perfect validation results with zero errors. However, a clear difference is observed in training time, with MLP requiring considerably more time to train on the new dataset. The test classification results are depicted in Figures 4.4.9–4.4.12, highlighting the well-classified and misclassified samples using the same method as for the amplitude-only dataset. Furthermore, Table 4.4.5 provides a summary of the average accuracy performance for all contaminated and uncontaminated classes.

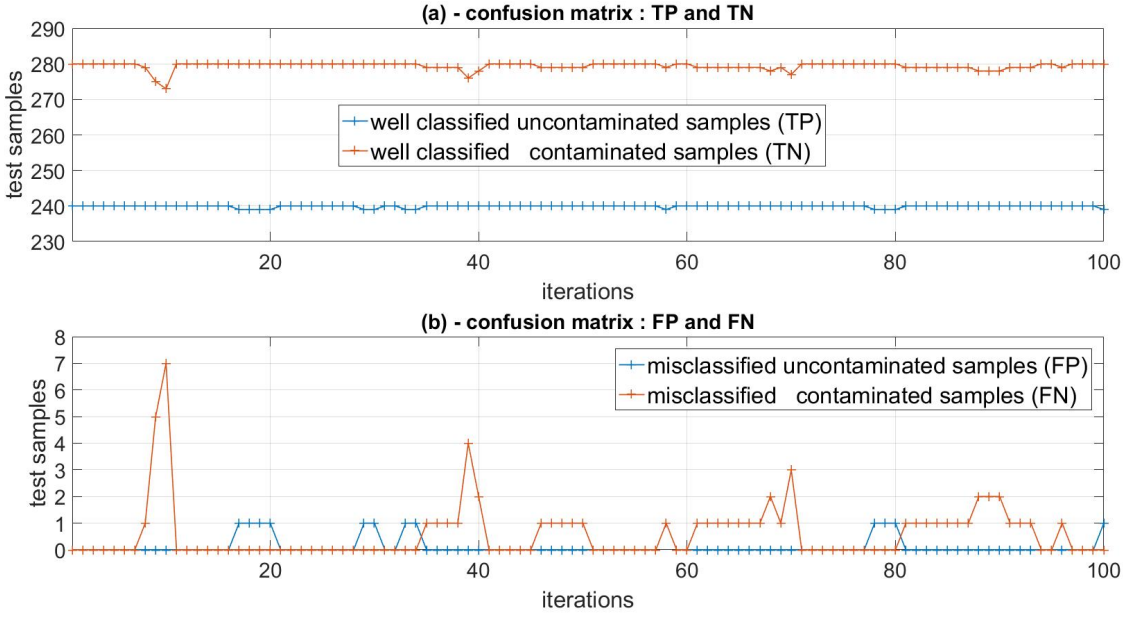

Figure 4.4.9: Confusion matrices obtained by the non-linear SVM classifier trained on the Complex nature dataset. Curve (**a**) shows the plot of the well-classified terms TP and TN, while curve (**b**) is the plot of the misclassified terms FP and FN.

The new dataset significantly improves classification outcomes, with the MLP algorithm achieving a notable accuracy of 99.3% as shown in Table 4.4.5. The non-linear SVM demonstrates even stronger

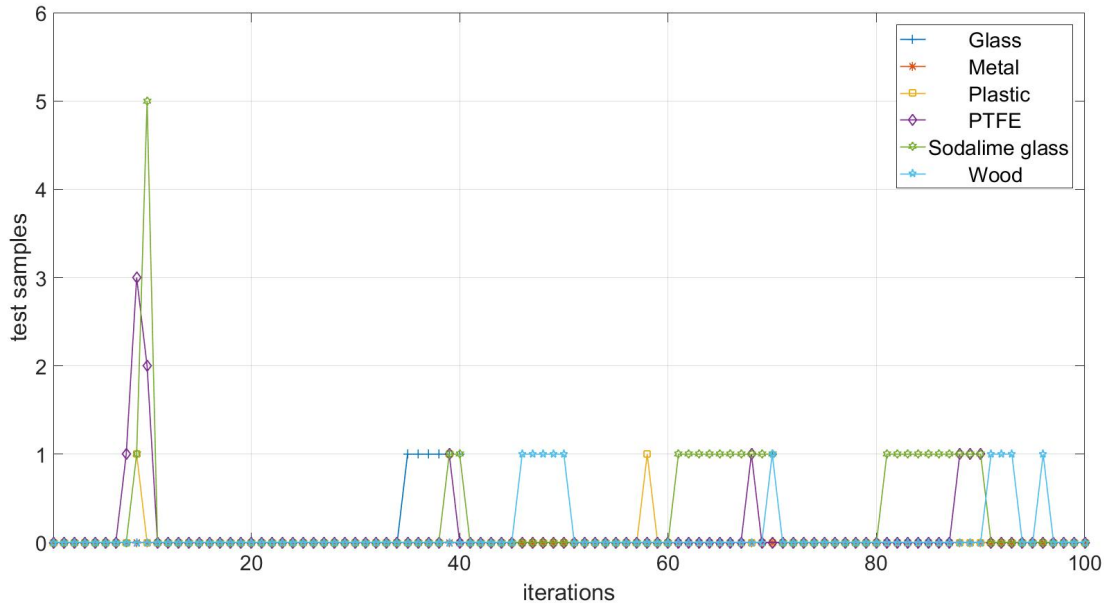

Figure 4.4.10: The plot of the misclassified terms FP and FN of the confusion matrices for each contaminated class alone. The results obtained by the non-linear SVM algorithm trained on the Complex nature dataset.

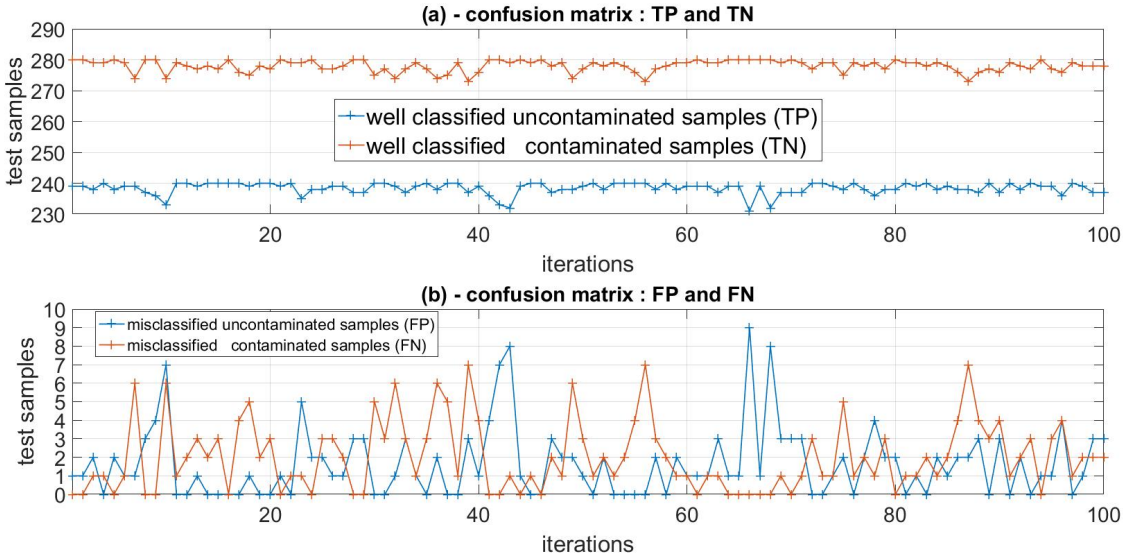

Figure 4.4.11: Confusion matrices obtained by the MLP classifier trained on the Complex nature dataset. Curve (**a**) shows the plot of the well-classified terms TP and TN ,while curve (**b**) is the plot of the misclassified terms FP and FN.

performance, attaining an average classification accuracy of 99.8% and approaching 100% accuracy for most classes, including 99.3% for the critical case. These results highlight the power of the non-linear SVM, not only in classification accuracy but also in training efficiency and the stability of its results across multiple test iterations.

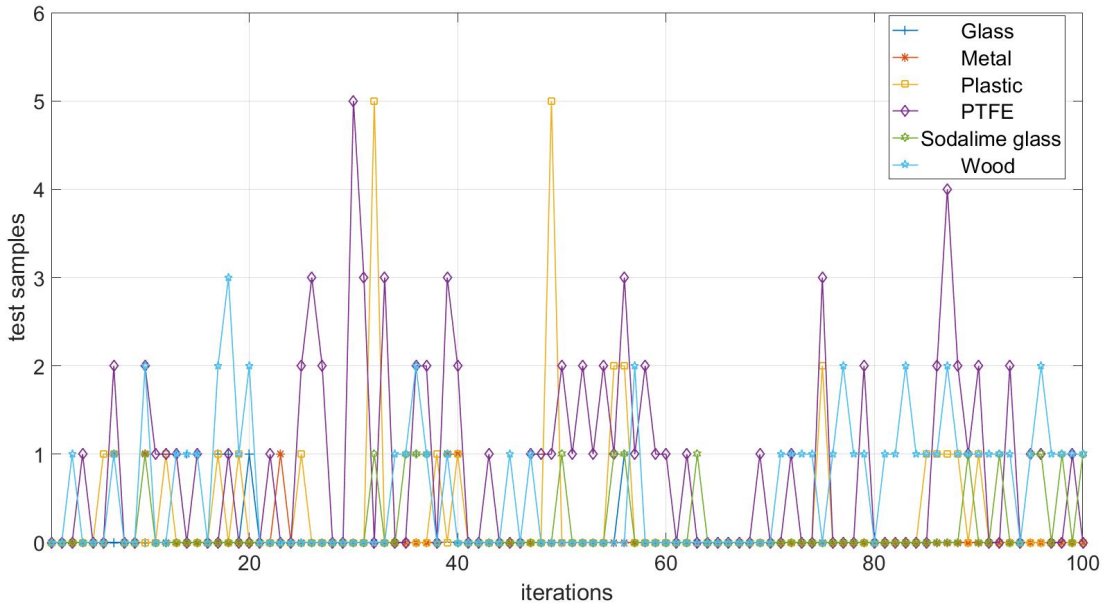

Figure 4.4.12: The plot of the misclassified terms FP and FN of the confusion matrices for each contaminated class alone. The results were obtained by the MLP algorithm trained on the Complex nature dataset.

Table 4.4.5: Average classification accuracy per class for both classifiers on the complex number-based dataset.

Classes	Accuracy with SVM (%)	Accuracy with MLP (%)
Uncontaminated	99.9	99.3
Contaminated with small splinter of Glass	99.9	99.8
Contaminated with Metal	100	99.9
Contaminated with small splinter of Plastic	100	99.5
Contaminated with PTFE (4 mm sphere)	99.7	98
Contaminated with SLG (4 mm sphere)	99.3	99.6
Contaminated with fragment of wood	99.8	98.6

To conclude the section presenting and discussing our results, it is important to compare them with those published in [160]. Table 4.4.6 below provides a summary of the conditions and outcomes of our study in comparison to the findings reported in [160].

Table 4.4.6 presents the performance accuracy of the classifiers on the test datasets under different conditions. The use of GWO with the MLP algorithm helps in determining the optimal number of neurons efficiently, requiring only about 50 seconds—a process that would take significantly longer if performed manually. One key factor influencing accuracy is the distribution of samples between the training and test sets. In our work, we reduce the size of the training dataset to allocate more samples for testing, splitting the data into 58% for training and 42% for testing. In contrast, the dataset in [160] is split into 70% for training and 30% for testing. Despite this difference, the resulting change in accuracy was minimal (approximately 0.05%), which is expected, as a larger test dataset typically leads to a slight increase in error.

Table 4.4.6: The average classification accuracy of both classifiers using the complex number-based dataset.

Conditions	[160]	This contribution	This contribution
Used classifier	MLP	MLP	Non-linear SVM
Dataset nature	Complex (Real-Imag)	Complex (Real-Imag)	Complex (Real-Imag)
Dataset split (Training set–Test set)	70%–30% (868–372 samples)	58%–42% (720–520 samples)	58%–42% (720–520 samples)
Optimization method	None -	GWO	GWO
Average accuracy	99.35%	99.3%	99.8%

4.5 Second Contribution

The second contribution originates directly from the microwave (MW) sensing system, which was thoroughly detailed in Chapter 2, including all associated measurements and simulation analyses. The data processing methodology for this contribution follows the same approach outlined earlier in this chapter, before presenting the first contribution. In the contribution published in [111] we focus on expanding the range of investigated food and beverage product ingredients. As water and oil are the primary components of many food products, we propose a methodology for testing items with high water content, a lossy medium, as well as those mainly composed of oil, a low-loss medium. To align with these objective, we build upon the system presented in [160, 162], replacing the antenna array elements with antennas that operate effectively across a broadband frequency range. This wide frequency range ensures compatibility with various material media, including oil and water. Chapter 2 elaborates on the steps taken to design and upgrade the new system. This contribution establishes a comprehensive measurement framework for binary and multiclass classification using SVM, enabling the differentiation of various contaminant types. It concludes with classification results obtained with the SVM algorithm, following an in-depth discussion of the most relevant training datasets for oil-based and water-based products.

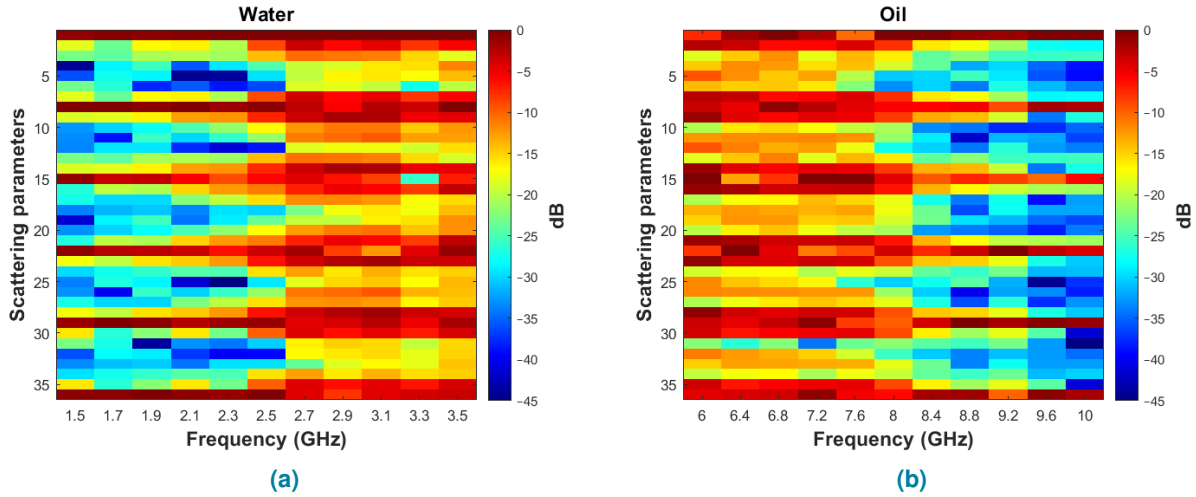

Figure 4.5.1: The normalized amplitude of the scattering matrix [S_n] for two uncontaminated samples under test [162]: (a) Water. (b) Oil.

Figure 4.5.1 presents the plots of two matrices in the same format as described in Equation 4.3.4 (the

amplitude-only representation of the scattering parameters, [S_n^A]), corresponding to different samples, with each matrix normalized to its respective maximum amplitude value. In subfigure 4.5.1a, the magnitude values reveal improved transmission performance of the antennas above 2.5 GHz for the water-based jar. This observation aligns with the antenna reflection coefficient behavior shown in Figure 2.3.3, where the antenna is poorly matched below 2.5 GHz. Conversely, in subfigure 4.5.1b, the values indicate good transmission performance between 6 GHz and 8 GHz, followed by a decline in the transmission coefficient magnitudes beyond this range. This decline corresponds to the near-field antenna behavior shown in Figure 2.3.4, which shows a noticeable reduction in radiated field strength above 8 GHz. The significant variations in the magnitude of transmission coefficients within these frequency bands for oil-based and water-based jar samples allow selective focus on subranges with optimal transmission behavior. This selection process will be further demonstrated in the experimental results section, where classification is performed using only the most significant transmission coefficient magnitudes within these frequency bands.

In addition we performed PCA on the training sets for both water-based and oil-based food samples, using datasets containing only amplitude values as well as datasets incorporating the complex numbers of the S-parameters. Figures (4.5.3, 4.5.2) present the projection of the three most significant eigenvectors from the PCA results. These three components account for the majority of the variance, exceeding 80% for all datasets, and effectively summarize the key information across the different datasets. For oil-based samples (Figure 4.5.2), the data demonstrate overlap and a distinctly nonlinear relationship between contaminated and uncontaminated samples in both the magnitude-only and complex nature datasets. Conversely, for water-based samples (Figure 4.5.3), while the magnitude-only dataset also exhibits overlaps, the complex nature dataset reveals linear separability and minimal correlation. Based on this analysis, we explore the application of nonlinear algorithms, such as SVM, to effectively classify and differentiate all sample types.

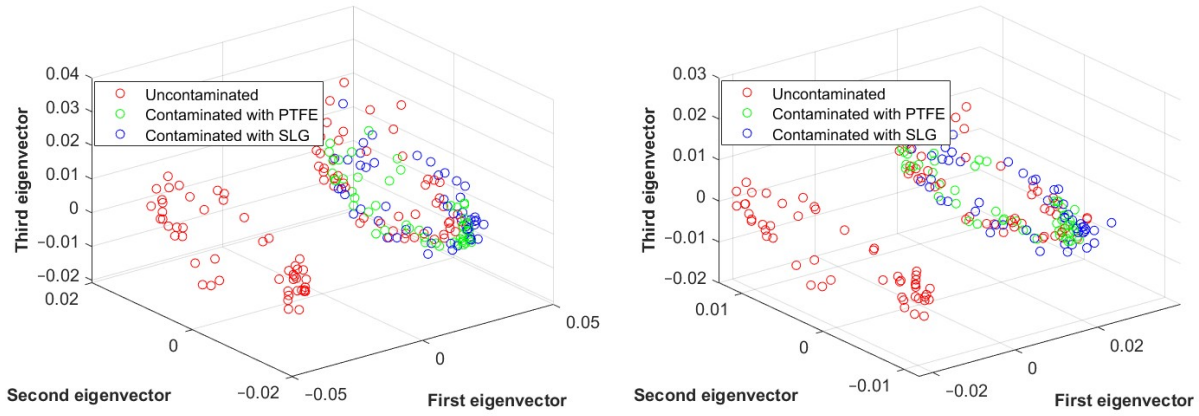

Figure 4.5.2: Projection of PCA results onto the three most significant eigenvectors for oil-based samples: (a) Complex numbers dataset, and (b) Amplitude-only dataset.

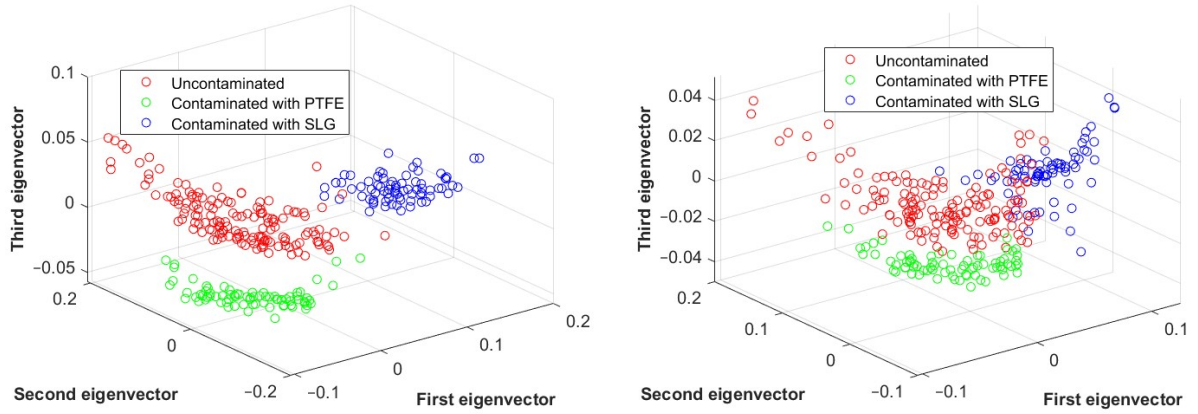

Figure 4.5.3: Projection of PCA results onto the three most significant eigenvectors for water-based samples: (a) Complex numbers dataset, and (b) Amplitude-only dataset.

4.5.1 Classification Results

In this section we present the results obtained by applying the non-linear SVM algorithm to the datasets described in the dataset construction subsection. The analysis focuses on two categories of food products: oil-based and water-based. The following subsections provide detailed findings, addressing various factors influencing the performance of the ML classifier. These factors include the use of the complex numbers dataset, inclusion of only the amplitude component of the measurement data, dataset partitioning (training and testing sets), selection of frequency bands, and different classification types (binary and multiclass). The accuracy values shown in the subsequent tables represent the average performance over 100 classification trials. In this contribution, we evaluate the classifier's performance using the same approach as in the first contribution. Specifically, in each iteration, the dataset is shuffled, and new samples are randomly assigned to the training and testing sets while keeping the optimized hyperparameters constant. Additionally, the presented confusion matrices correspond to the worst reproducible outcomes among the 100 iterations.

In the following subsections, we will examine two types of classifications: binary and multi-class. Binary classification focuses on distinguishing between contaminated and uncontaminated products, while multi-class classification aims to identify the specific type of contaminant. For the multi-class analysis, three categories are considered: uncontaminated, contaminated with PTFE, and contaminated with SLG. While the primary interest of the industry lies in determining whether a product is contaminated (binary classification), multi-class classification provides additional insight by identifying the specific contaminants. This information might be important in pinpointing the stage of the production process responsible for the defects.

Results on Water-based contents

This subsection presents and discusses the classification accuracy achieved on the complex-number dataset for water-based food products under different conditions, as outlined in Table 4.5.1. These conditions include variations in dataset partitioning, classification types, and frequency bands. The results

are analyzed and compared based on these factors. Table 4.5.1 presents results for two dataset splits: 300-200 and 200-300, corresponding to the number of training and test samples, respectively. The classification accuracy is perfect for all binary classifications, regardless of the varying conditions. In multiclass classifications, the accuracy remains consistently high across both dataset splits, ranging from 99.8% to 100%. These findings demonstrate that the SVM model's performance is robust and largely unaffected by the distribution of training and test samples. The minor errors observed in the last two confusion matrices in Table 4.5.1 pertain to a single test sample contaminated with a small PTFE sphere. In one instance, it was misclassified as contaminated with an SLG sphere, and in another, it was incorrectly labeled as uncontaminated which is a more critical misclassification.

Table 4.5.1: Classification results using SVM on the complex numbers dataset of water-based samples.

Dataset Split (Training-Test)	Type of classification	Frequency Band [start : step : end] GHz	Confusion Matrices (On Test Set)	Accuracy (%)
300-200 samples	Binary	[1.5 : 0.2 : 3.5]	$\begin{bmatrix} 150 & 0 \\ 0 & 50 \end{bmatrix}$	100
300-200 samples	Binary	[2.5 : 0.2 : 3.5]	$\begin{bmatrix} 150 & 0 \\ 0 & 50 \end{bmatrix}$	100
200-300 samples	Binary	[1.5 : 0.2 : 3.5]	$\begin{bmatrix} 200 & 0 \\ 0 & 100 \end{bmatrix}$	100
200-300 samples	Binary	[2.5 : 0.2 : 3.5]	$\begin{bmatrix} 200 & 0 \\ 0 & 100 \end{bmatrix}$	100
300-200 samples	Multiclass	[1.5 : 0.2 : 3.5]	$\begin{bmatrix} 150 & 0 & 0 \\ 0 & 25 & 0 \\ 0 & 0 & 25 \end{bmatrix}$	100
300-200 samples	Multiclass	[2.5 : 0.2 : 3.5]	$\begin{bmatrix} 150 & 0 & 0 \\ 0 & 25 & 0 \\ 0 & 0 & 25 \end{bmatrix}$	100
200-300 samples	Multiclass	[1.5 : 0.2 : 3.5]	$\begin{bmatrix} 200 & 0 & 0 \\ 0 & 49 & 1 \\ 0 & 0 & 50 \end{bmatrix}$	99.8
200-300 samples	Multiclass	[2.5 : 0.2 : 3.5]	$\begin{bmatrix} 200 & 0 & 0 \\ 1 & 49 & 0 \\ 0 & 0 & 50 \end{bmatrix}$	99.8

Table 4.5.2 summarizes the results obtained from a dataset containing only the magnitude component of the measurements. For binary classification within the full 1.5–3.5 GHz frequency band, both dataset splits achieved 100% accuracy, with no misclassifications. In the reduced 2.5–3.5 GHz band (as discussed in Figure 4.5.1 for water-based products), the accuracy remains high at 99.7% for both splits, with only a few errors, including one uncontaminated sample misclassified as contaminated. For multiclass classification, the 300–200 dataset split achieved 99.9% accuracy in the 1.5–3.5 GHz band, with minor

misclassifications where an uncontaminated test sample is identified as contaminated. In the 2.5–3.5 GHz band, accuracy slightly decreased to 99.5%, with a small number of misclassifications. The 200–300 dataset split maintained high accuracy (99.8%) across both frequency bands, with confusion matrices showing a PTFE-contaminated sample misclassified as SLG-contaminated. In summary, Table 4.5.2 highlights that classification experiments using magnitude-only data for water-based samples achieved consistently high accuracies. The results are robust across different dataset splits and frequency bands, with only minor variations in accuracy and a few misclassifications.

Table 4.5.2: Classification results using SVM on the amplitude-only dataset for water-based samples.

Dataset Split (Training-Test)	Type of classification	Frequency Band [start : step : end] GHz	Confusion Matrices (On Test Set)	Accuracy (%)
300-200 samples	Binary	[1.5 : 0.2 : 3.5]	$\begin{bmatrix} 150 & 0 \\ 0 & 50 \end{bmatrix}$	100
300-200 samples	Binary	[2.5 : 0.2 : 3.5]	$\begin{bmatrix} 149 & 1 \\ 0 & 50 \end{bmatrix}$	99.7
200-300 samples	Binary	[1.5 : 0.2 : 3.5]	$\begin{bmatrix} 200 & 0 \\ 0 & 100 \end{bmatrix}$	100
200-300 samples	Binary	[2.5 : 0.2 : 3.5]	$\begin{bmatrix} 199 & 1 \\ 0 & 100 \end{bmatrix}$	99.7
300-200 samples	Multiclass	[1.5 : 0.2 : 3.5]	$\begin{bmatrix} 149 & 1 & 0 \\ 0 & 25 & 0 \\ 0 & 0 & 25 \end{bmatrix}$	99.9
300-200 samples	Multiclass	[2.5 : 0.2 : 3.5]	$\begin{bmatrix} 150 & 0 & 0 \\ 0 & 24 & 1 \\ 0 & 0 & 25 \end{bmatrix}$	99.5
200-300 samples	Multiclass	[1.5 : 0.2 : 3.5]	$\begin{bmatrix} 200 & 0 & 0 \\ 0 & 49 & 1 \\ 0 & 0 & 50 \end{bmatrix}$	99.8
200-300 samples	Multiclass	[2.5 : 0.2 : 3.5]	$\begin{bmatrix} 200 & 0 & 0 \\ 0 & 49 & 1 \\ 0 & 0 & 50 \end{bmatrix}$	99.8

Results on Oil-based contents

Following the same approach used for presenting classification results for water-based samples, we now provide the results for classifying food samples based on oil content. For binary classification using the complex nature dataset within the 6–10 GHz frequency band and a 250–240 dataset split, an accuracy of 96.7% is achieved. The confusion matrix indicates a high number of correctly classified samples, with eight false positives are recorded. When narrowing the frequency band to 6–8 GHz (as discussed in

Figure 4.5.1 for oil-based products) with the same dataset split, the accuracy increases slightly to 98%, with the confusion matrix showing fewer false positives (four samples).

For multiclass classification experiments, performance accuracies of 95% and 95.5% are achieved for the 290–200 dataset split across the two frequency bands, respectively. However, the confusion matrices reveal notable misclassifications, particularly within the uncontaminated class. In summary, Table 4.5.3 highlights varying outcomes across different classification scenarios. Binary classification experiments demonstrate high accuracy in both frequency bands, while multiclass classification exhibited slightly lower but still effective accuracy levels.

Table 4.5.3: Classification results using SVM on the complex numbers dataset of oil-based samples.

Dataset Split (Training-Test)	Type of classification	Frequency Band [start : step : end] GHz	Confusion Matrices (On Test Set)	Accuracy (%)
250-240 samples	Binary	[6 : 0.4 : 10]	$\begin{bmatrix} 72 & 8 \\ 0 & 160 \end{bmatrix}$	96.7
250-240 samples	Binary	[6 : 0.4 : 8]	$\begin{bmatrix} 76 & 4 \\ 0 & 160 \end{bmatrix}$	98
290-200 samples	Multiclass	[6 : 0.4 : 10]	$\begin{bmatrix} 90 & 10 & 0 \\ 0 & 50 & 0 \\ 0 & 0 & 50 \end{bmatrix}$	95
290-200 samples	Multiclass	[6 : 0.4 : 8]	$\begin{bmatrix} 91 & 9 & 0 \\ 0 & 50 & 0 \\ 0 & 0 & 50 \end{bmatrix}$	95.5

Table 4.5.4 presents the results for binary classification, where high accuracies are achieved across both frequency bands. For the 6-10 GHz band, the accuracy reaches 98.3%, while the algorithm performs slightly better on the 6-8 GHz band, with an accuracy of 99.6%. Misclassifications are observed only in the false positive class (uncontaminated samples are classified as contaminated). In multiclass classification, perfect performance is achieved in the 6-8 GHz frequency band with 100% accuracy, and a high accuracy of 99.8% is obtained for the 6-10 GHz band.

The significant improvement in performance on the magnitude-only dataset can be attributed to the exclusion of the phase component from the measurements. In the near-field region, the phase of scattering parameters is highly sensitive to small variations in distance. Minor shifts in the object's position relative to the measurement system can cause substantial phase fluctuations. Given the movement of the jar, these phase changes increase the complexity of the dataset. In contrast, the classifications involving water exhibited nearly perfect accuracy in both dataset types, likely due to the high permittivity contrast between water and the contaminants, which simplifies the classification. However, the contrast in permittivity between oil and the contaminants is lower, adding complexity to the classification process and contributing to the observed performance errors in oil-based samples.

Based on the readings from Figure 4.5.1(a,b), we have proposed the idea of selecting a specific subrange within the frequency bandwidths for measurement. This choice is driven by the favorable transmission characteristics observed in the amplitude plot of the scattering parameters in Figure 4.5.1(a,b).

The effectiveness of this approach is confirmed by the results, where the classifier algorithm shows improved performance when using data from the 6 GHz to 8 GHz range for oil-based products.

Table 4.5.4: Classification results using SVM on the amplitude-only dataset for oil-based samples.

Dataset Split (Training-Test)	Type of classification	Frequency Band [start : step : end] GHz	Confusion Matrices (On Test Set)	Accuracy (%)
250-240 samples	Binary	[6 : 0.4 : 10]	$\begin{bmatrix} 76 & 4 \\ 0 & 160 \end{bmatrix}$	98.3
250-240 samples	Binary	[6 : 0.4 : 8]	$\begin{bmatrix} 78 & 2 \\ 0 & 160 \end{bmatrix}$	99.6
290-200 samples	Multiclass	[6 : 0.4 : 10]	$\begin{bmatrix} 100 & 0 & 0 \\ 0 & 49 & 1 \\ 0 & 0 & 50 \end{bmatrix}$	99.8
290-200 samples	Multiclass	[6 : 0.4 : 8]	$\begin{bmatrix} 100 & 0 & 0 \\ 0 & 50 & 0 \\ 0 & 0 & 50 \end{bmatrix}$	100

4.6 Third Contribution

In this contribution, we focus on commercial food products to evaluate and enhance the practicality of our previous works [111, 162]. Two distinct market-available food items are selected: pesto sauce, primarily composed of oil and cheese, classifying it as an oil-based product and a non-homogeneous medium, and pure tomato sauce, identified as a water-based product. The details of the MW sensing system (illustrated in Figure 4.6.1) employed in this approach are outlined in [111]. However, the selected commercial products feature metal caps, which prevent the use of the previously designed arc-shaped antenna arrangement above the jar, as described in [120] and [111]. To address this, the six antennas are completely repositioned and distributed on either side of the jar, as shown in Figure 4.6.1. This triangular arrangement on each side ensures optimal coverage of the jar.

4.6.1 Measurments and Classifications

In this study, building on the findings of our previous work in [111], two distinct frequency bands are selected for the measurements. For tomato sauce samples, which are water-based products with high-loss characteristics and limited microwave (MW) penetration, a frequency range of 2–4 GHz is chosen. In contrast, for pesto sauce samples, which are oil-based products with low-loss characteristics and better MW penetration, a higher frequency range of 6–10 GHz is selected. Eleven frequency points are evenly distributed within each frequency band.

We have prepared three samples of each type: two uncontaminated and one contaminated with a SLG sphere measuring 4 mm in diameter. SLG is chosen for contamination testing because it is commonly used in packaging food and beverage products similar to those tested. The samples and the contaminant

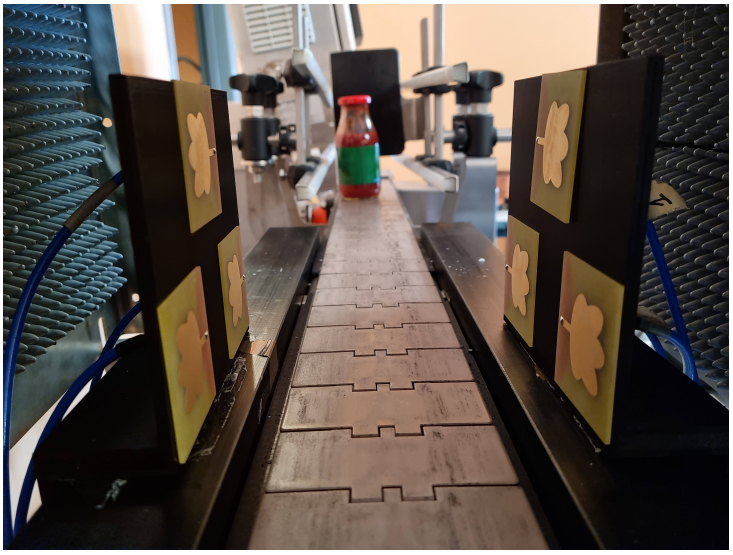

Figure 4.6.1: The updated antenna configuration.

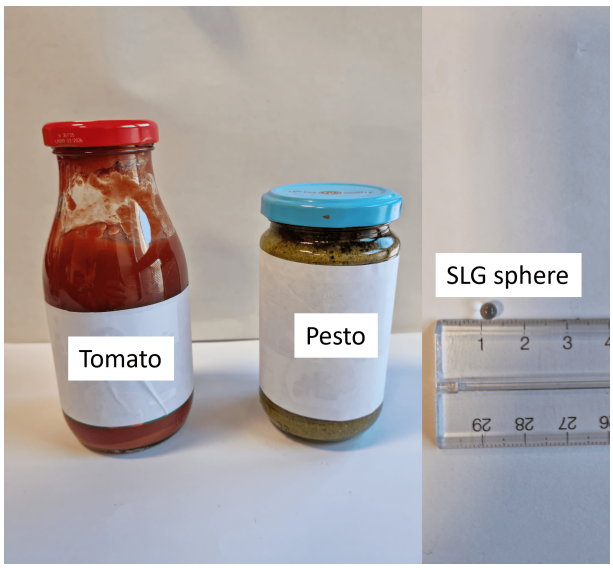

Figure 4.6.2: Packaged food products and a 4 mm SLG sphere used as a contaminant.

are depicted in Figure 4.6.2. A total of 400 measurements are conducted for both food types, equally divided between contaminated and uncontaminated samples. For each test, the sample is rotated at a slight angle to vary its orientation relative to the antenna array elements. This practice enhances the realism and robustness of the measurements. Each measurement produces a $6 \times 6 \times 11$ scattering parameters corresponding to the sample under test. Since these parameters are complex numbers, each sample is represented as a 792-entry vector for use in the classifier. The detailed process of dataset preparation is thoroughly explained in the dataset construction section of this chapter.

For the classification process, two algorithms are employed: the non-linear SVM classifier and the MLP neural network. These algorithms are implemented following the methods outlined in Chapter 3 and the approaches described in [111, 140, 162]. Additionally, the Grey Wolf Optimizer (GWO) is utilized to determine the optimal hyperparameters for both classifiers (C* and γ* for SVM and N* for MLP), as

detailed previously in chapter 3 and in [140].

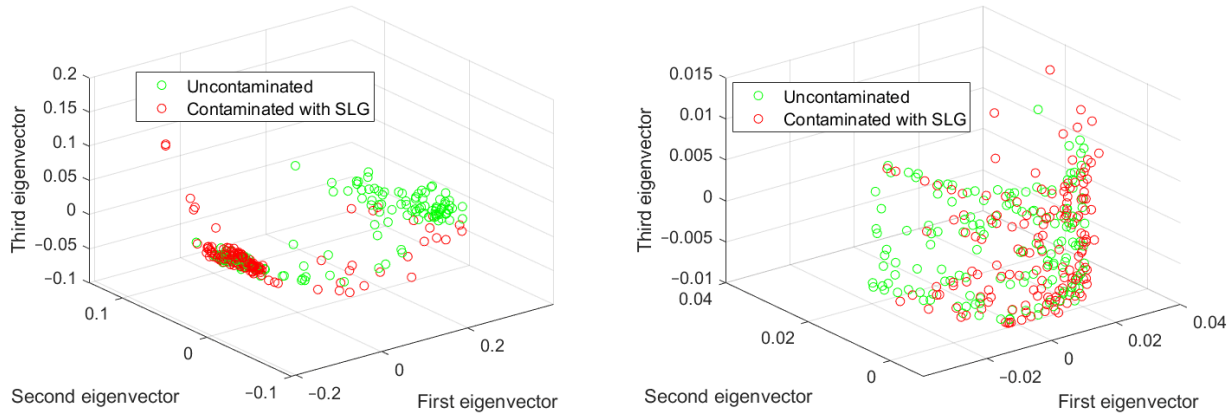

Figure 4.6.3: Projection of PCA results onto the three most significant eigenvectors [163]: (a) Tomato samples, (b) Pesto samples.

Figures 4.6.3a and 4.6.3b illustrate the projection of principal component analysis (PCA) onto the three most significant eigenvectors for the tomato and pesto datasets. These three components account for a significant amount of variance: 95% for the tomato dataset and 85% for the pesto dataset. This indicates that these components effectively capture the key variations within the data, providing valuable insight into the datasets' structures. The dataset structure exhibits a highly nonlinear and correlated relationship for both pesto and tomato cases. The dataset distribution in both cases (tomato and pesto) suggests again the necessity of using a nonlinear ML algorithm, such as MLP or nonlinear SVM.

4.7 Classification results

Table 4.7.1 summarizes the classification results. The datasets are divided into two segments: a training set and a test set, as detailed in Table 4.7.1. The results represent the average of 100 iterations, including both training and testing phases. In each iteration, the algorithm randomly shuffles the datasets and selects samples for training and testing. Both classifiers achieve perfect accuracy of 100% on the two datasets.

For industrial applications, we aim to reduce the number of training samples while increasing the size of the test set. This approach reflects real-world scenarios where industries often rely on a fixed number of training samples, while testing involves a much larger sample pool. Reducing the training sample size, we monitor the performance of both classifiers under various dataset splits. Accuracy remains consistently perfect at 100% across all splits until reaching a training-test split of (100-300). At this point, some misclassifications are observed, with contaminated samples occasionally identified as uncontaminated. Despite this, the accuracy remains high, approximately 98% for both algorithms, as shown in Table 4.7.1.

Table 4.7.1: Classification results.

Food	Classifier	Frequency Band [start : step : end] GHz	Dataset split (Training-Test)	Accuracy (%)
Tomato	Non-Linear SVM	[2 : 0.2 : 4]	(300 – 100)	100
Tomato	Non-Linear SVM	[2 : 0.2 : 4]	(200 – 200)	100
Tomato	Non-Linear SVM	[2 : 0.2 : 4]	(150 – 250)	99
Tomato	Non-Linear SVM	[2 : 0.2 : 4]	(100 – 300)	99
Tomato	MLP	[2 : 0.2 : 4]	(300 – 100)	100
Tomato	MLP	[2 : 0.2 : 4]	(200 – 200)	100
Tomato	MLP	[2 : 0.2 : 4]	(150 – 250)	99
Tomato	MLP	[2 : 0.2 : 4]	(100 – 300)	98
Pesto	Non-Linear SVM	[6 : 0.4 : 10]	(300 – 100)	100
Pesto	Non-Linear SVM	[6 : 0.4 : 10]	(200 – 200)	100
Pesto	Non-Linear SVM	[6 : 0.4 : 10]	(150 – 250)	99
Pesto	Non-Linear SVM	[6 : 0.4 : 10]	(100 – 300)	99
Pesto	MLP	[6 : 0.4 : 10]	(300 – 100)	100
Pesto	MLP	[6 : 0.4 : 10]	(200 – 200)	100
Pesto	MLP	[6 : 0.4 : 10]	(150 – 250)	99
Pesto	MLP	[6 : 0.4 : 10]	(100 – 300)	98

4.8 Conclusion and limitations

The urgent need to detect physical contaminants in food and beverage products before market distribution motivated our development of an MW sensing system for evaluating products with diverse ingredients. Given the widespread presence of water and oil as primary components in many food and beverage items, we presented a versatile methodology applicable to both mediums. This study explored the integration of MW sensing technology with machine learning for physical contaminant detection. The process involved collecting scattering parameters to build datasets, followed by classification using the SVM and MLP algorithms. Our contributions started with a proof of concept demonstrating the effectiveness of such systems on oil-based and water-based products, as outlined in the first and second contributions. We then extended our findings by testing real commercial products to further validate our approach, as presented in the third contribution. The results demonstrated high accuracy across all three contributions, employing different ML algorithms (SVM and MLP) for both binary and multiclass classifications, and utilizing various dataset types (real-imaginary and magnitude-only).

While our studies have significantly advanced the use of MW sensing technology combined with ML tools for the non-invasive evaluation of food and beverage products, it is important to highlight certain limitations to provide a well-rounded perspective on our findings. The primary challenges lie in the algorithm training phase. First, the number of samples used for training in the three contributions was the minimum required to achieve satisfactory classification performance. Additionally, in the multiclass analysis, incorporating more contaminant materials led to decreased classification accuracy. To address

these limitations, our future work will focus on enhancing the methodology robustness by exploring more ML algorithms and expanding the range of contaminants, particularly for multiclass classification. Furthermore, we plan to extend our experimental analysis to a broader variety of food and beverage products and conduct system testing in real industrial environments.

5 Millimeter-Wave (mmW) Imaging assisted wit ML Tools

In the first chapter about state-of-the-art review, we discussed studies on mmW imaging techniques combined with ML tools for classifying apples and peaches [103, 104]. The promising results from these studies motivate us to assess the effectiveness of this approach on more challenging cases—specifically, the classification of in-shell seeds such as almonds and walnuts. Previous research has demonstrated two types of classification: distinguishing between different fruit types (apples and peaches) [103] and identifying healthy versus damaged fruit [104]. This study aims to assess the method's ability to distinguish between almonds and walnuts. The challenge lies in the minimal electromagnetic differences between the two nuts, as their dielectric permittivity values are close, their external size and shape are very similar, and they both have very low water content.

In this chapter, we present the mmW imaging system used in this approach and outline the measurement process. Next, we explain how the acquired data are processed to construct the images and create the dataset, followed by the classification results.

5.1 mmW System Setup and Measurements

The measurement system used in this work is installed at the Laboratory of Electronics, Antennas, and Telecommunications (LEAT). Figure 5.1.1 illustrates the mmW measurement system. It consists of the 3D spherical scanner and offers multidimensional views, complete polarimetric capabilities in monostatic and multistatic configurations, and requires four axes of rotation:

- **The first axis of rotation, denoted as φ:** Rotation around this axis describes an arc in the vertical xoy plane. The angle φ ranges between $\pm 90°$.
- **The second axis, denoted as θ:** Movement around this axis describes an arc perpendicular to the first. The angle θ varies between $\pm 150°$.
- **The third axis of rotation, denoted as χ:** This axis changes the polarization direction. The angle χ rotates over 360°. In this work, we only use the positions $\chi = 0°$ and $\chi = 90°$ to switch from horizontal polarization to vertical polarization respectively defined for $\theta = 0°$
- **The fourth axis, the η axis:** This axis allows the support shown in Figure 5.1.1 (where the object under test is placed) to rotate. It also rotates over 360°, but this axis will not be used in this work.

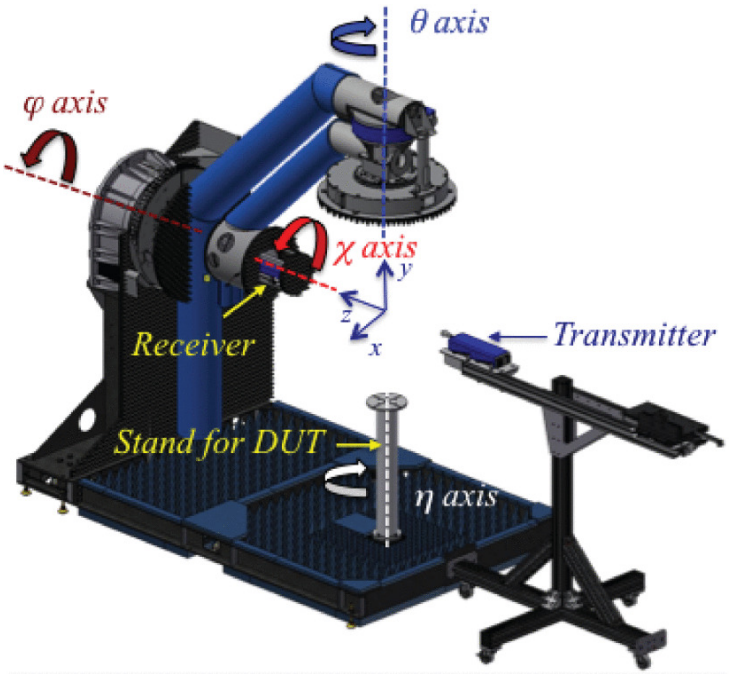

Figure 5.1.1: 3D scanner [164] showing scan axes (θ, ϕ) and polarization axis (χ).

When θ = 90° and φ = 90°, the system's probe is positioned above the support. The rotation axes θ and φ enable the movement of an antenna attached to a pivoting arm that can reach any point on the acquisition sphere. The object under test (OUT) is positioned on a cylindrical Rohacell support, made of polymethacrylimide (PMI), which is placed on a stand constructed from Polyvinyl Chloride (PVC) plastic, as illustrated in Figure 5.1.1. The Rohacell material has a dielectric constant of $\varepsilon_r \approx 1.02$ at a frequency of 1 GHz, which ensures that it is transparent to electromagnetic waves [165]. However, Rohacell is not entirely transparent at millimeter-wave (mmW) frequencies, as will be discussed later when constructing the 2D-FFT images. To address this, we introduce a layer of absorbing material between the Rohacell and the OUT in order to reduce the undesired reflection effects.

Determining the dielectric properties, particularly the relative permittivity ε_r, from measurements of the scattered field is an ill-posed and non-linear problem due to data loss, as outlined in Chapter 1. To mitigate these challenges, additional information is introduced to compensate for the loss of data:

1. Polarization.
2. Frequency.
3. The angle of the incident field $\mathbf{E_i}$.

Regarding the angle of the incident field, the measurement system allows for monostatic and multistatic measurements at any point on the acquisition sphere: the monostatic configuration of the measurement system uses a WR-10 standard gain horn, which, due to its directivity, minimizes interference from directions other than the object under test. As for the multistatic configuration of the measurement system, it uses a waveguide for transmission and a horn antenna for reception. The waveguide antenna provides a fairly wide angle for the incident field $\mathbf{E_i}$, compensating for possible alignment errors.

The choice of the monostatic configuration has several advantages, such as:

- A monostatic system is simpler to design than a multistatic system, especially in millimeter-wave frequency bands.
- The advantage of a multistatic configuration is that it provides useful information when the wave passes through the object under test. However, when working with millimeter waves, we expect low penetration into the fruits that are reached in water.

That is why, for this application, the monostatic configuration is chosen, where the angle of the field $\mathbf{E_i}$ is simply obtained by varying the position of the horn antenna along the θ and φ axes, creating spatial diversity. As for frequency diversity, measurements are made using three frequencies in the W-band (92, 94, and 96 GHz). Finally, measurements are performed in Horizontal Polarization (HP) and Vertical Polarization (VP).

The choice of intermediate frequency (IF) for the VNA influences the noise level and measurement time. We chose an IF of 100 Hz as the best compromise. Indeed, a low IF reduces the noise floor but increases the measurement time, as it has the same effect as averaging. With these settings, the noise floor is -70 dBm, while the maximum input power is approximately 5 dBm.

5.2 Backpropagation Imaging Algorithm

The back-propagation method is a simple processing technique, provided that the distance between the observation plane and the object is known. It is valid under the condition that there are no sources or objects between the reconstruction plane and the observation plane [166].

The scattered field E^s can be defined as:

$$E^s = G^R \, C \, E_{tot} \tag{5.2.1}$$

where:

- G^R is a matrix of dimensions M $\times$ N that contains the impulse response between the object and the receiving antenna, known as the Green's function. Here, M denotes the number of measurement points, and N represents the number of discretized points in the object or reconstruction domain.
- C is a diagonal matrix of dimensions N $\times$ N whose elements depend on the permittivity contrast between the object under test and the testing medium in which the object is located.
- E_{tot} is a vector of dimensions N $\times$ 1 that represents the total field in the test domain.
- E^s is a vector of dimensions M $\times$ 1 that represents the scattered field.

The back-propagation method relies on the computation of $C\,E_{tot}$, referred to as the contrast source, which is determined by:

$$C\,E_{tot} = \left(G^R\right)^{-1} E^s \tag{5.2.2}$$

However, the matrix G^R is not invertible because, in most cases, it is not square. Thus, the pseudo-inverse $\left(G^R\right)^* = \left(G^R\right)^t$ is defined as the conjugate transpose of the matrix G^R [167]. Using this approach, the scattered field can be back-propagated to obtain a field in the observation plane $\Sigma(x, y)$.

$$\Sigma(x,y) = \left(G^R\right)^* E^s = \left(G^R\right)^* G^R \, C \, E_{tot} = \sigma \, I \, C \, E_{tot} \tag{5.2.3}$$

where I is the identity matrix and $\sigma \in \mathbb{R}$ a scaling factor. The matrix $\left(G^R\right)^* G^R$ does not exactly give the identity matrix I; therefore, $\left(G^R\right)^* G^R = \sigma \, I$. The matrix $\left(G^R\right)^*$ can be approximated by the following equation, which represents the summation over all receiving antennas:

$$\Sigma(x,y) = \frac{1}{F}\frac{1}{L}\frac{1}{M}\sum_{f=1}^{F}\sum_{n=1}^{L}\sum_{m=1}^{M} d_m E^s(x_m, y_m, E_l^i e^{j\phi(x,y,x_m,y_m,f)}) \tag{5.2.4}$$

With:

- (x_m, y_m): coordinates of the position of the receiving antenna m.
- E_l^i: incident field from the transmitting antenna l.
- d_m: distance between the object and the receiving antenna m.
- F: number of measurement frequencies.
- L: number of transmitting antennas.
- M: number of receiving antennas.

The phase $\phi(x, y, x_m, y_m, f)$ depends on the geometry of the N cells, the position of the receiving antennas, as well as the frequency and the transmitter [168]. Since we are only working with monostatic measurements, the antenna is both transmitting and receiving ($L = M$) and at a single frequency $F = 1$. Furthermore, we do not directly measure the scattered field E^s but rather the reflection coefficient S_{11}. In our case, the S_{11} coefficients are measured on a sphere, and therefore, we switch to spherical coordinates, and Equation 5.2.4 becomes:

$$\Sigma(x_i, y_j) = \sum_{m=1}^{M} \frac{1}{d_m} S_{11}(u_m, v_m) e^{j\frac{4\pi}{\lambda}(u_m x_i + v_m y_i)} \tag{5.2.5}$$

With

- $\Sigma(x_i, y_j)$: spatial coordinate of the pixel (i, j) in the observation plane.
- $S_{11}(u_m, v_m)$: reflection coefficient at the measurement point in θ and ϕ with $u_m = d_m \sin\theta_m \cos\phi_m$ and $v_m = d_m \sin\theta_m \sin\phi_m$, spectral coordinates of the same measurement point.
- d_m: distance between the antenna and the pixel (i, j).
- λ: wavelength in free space.

5.3 Imaging Using 2D Fourier Transform (2D-FFT)

The two-dimensional Fourier Transform (2D-FT) is commonly recognized as a technique for converting spatial signals into the spectral domain (frequency domain). The 2D-FT is not a full reconstruction

method like tomographic techniques, but it is fast and efficient for processing the data. It serves as an approximation of the back-propagation method, provided that the angle of the incident field is perpendicular to the object's reconstruction plane [166]. However, this approach disregards the distance between the measurement plane and the observation plane. This limitation is acceptable in our case, as the localization and shape of the object are not of primary concern. Nonetheless, the relative permittivity contrast, which is our parameter of interest, remains preserved in the image.

The Two-Dimensional Fourier Transform is defined as:

$$\text{2D-FT}(x_k, y_l) = \sum_{m=0}^{M-1} \sum_{n=0}^{N-1} S_{11}(m,n)\, exp^{2\pi j\left(\frac{mk}{M}+\frac{nl}{N}\right)} \tag{5.3.1}$$

With:

- (x_k, y_l): coordinates of the pixel (k, l).
- $S_{11}(m, n)$: reflection coefficient at the measurement point for θ_m and ϕ_n.
- M and N: number of measurement points in θ and φ respectively.

In this work, we perform measurements around the vertical axis of the object, which leads to distortions in the images obtained using the 2D Fourier Transform (2D-FT) as we move away from the vertical axis. Although it provides a less comprehensive reconstruction, the 2D-FT is computationally efficient, and we employ its Fast Fourier Transform (2D-FFT) implementation, which significantly reduces computational time compared to the direct Fourier Transform.

5.4 Measurements and Data Acquisition

Figure 5.4.1: Walnuts and almonds used in the measurements: W1 to W7 denote the walnuts, and A1 to A8 denote the almonds.

For the measurement process, we prepare 15 samples, consisting of 7 walnuts and 8 almonds, numbered as shown in Figure 5.4.1. The Nut Under Test (NUT) is placed on the absorption material

above the Rohacell support. A WR-10 standard gain horn is mounted on a two-stage arm that rotates around the NUT at a distance of 585 mm. The scanning area spans 30° × 30° in θ and ϕ, with a step size of 0.2°. The step size is chosen to avoid grating lobes, i.e., spurious images, in accordance with the Shannon-Nyquist sampling theorem [169]. With a step size of 0.2°, we are operating at the 'Shannon limit,' which corresponds to the Nyquist rate—the minimum sampling rate necessary to accurately reconstruct a signal. The reference position (θ, ϕ) =(90°, 90°) is defined when the horn is directly above the NUT. The horn operates in a monostatic configuration. This configuration results in a matrix of 151 × 151 measured S_{11} corresponding to the different angles (θ, ϕ).

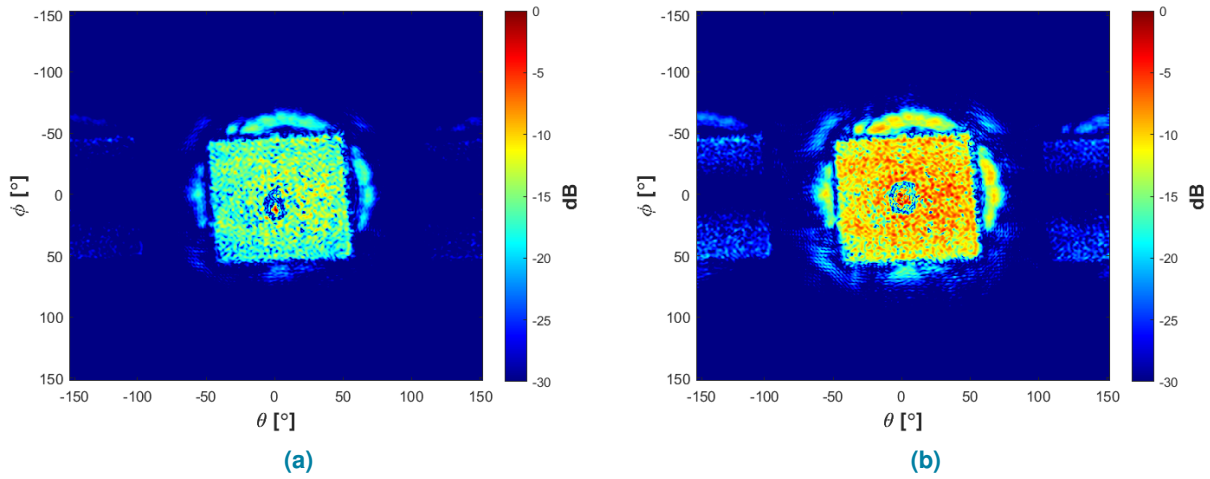

Figure 5.4.2: 2D-FFT images at 92 GHz corresponding to: (a) Almond1, and (b) Walnut1.

For each NUT, data are processed at three specific frequency points—92, 94, and 96 GHz, resulting in three images per sample. Figure 5.4.2 shows an example of these images, specifically at 92 GHz. In the images, mmW imaging reveals the details of the scanning area. For instance, Figures 5.4.2(a) and (b) highlight the reflections from the Rohacell cylindrical support and the absorbing material inserted between the NUT and this support, as indicated by the squared area. Additionally, the scattering from the NUT's bulb is visible, marked by the small red spot at the center of the figures. Notably, the reflection from the NUT appears to be only due to the bulb inside the shell, suggesting that the shell itself is transparent to the mmW.

The three images per sample are insufficient for machine learning algorithms. To make the most of the spatial diversity of our measurements, we increase the number of images by dividing the total measured area of 151×151 for each sample into 51×51 patches along the diagonal, as illustrated in Fig. 5.4.3. This approach represents each sample with 101 patches at each frequency point, resulting in a total of 303 patches per sample across the three frequencies. These patches serve as classification samples for the ML model in three different ways:

- **Path 1**: The first approach is based on image processing. It involves applying the 2D-FFT to each patch, followed by segmentation using Otsu's method [170], which converts RGB patches into binary images. After segmentation, the binary images are transformed back into matrices to prepare them for the classification stage.
- **Path 2**: Using the raw patch data by extracting the real and imaginary parts of S_{11}.

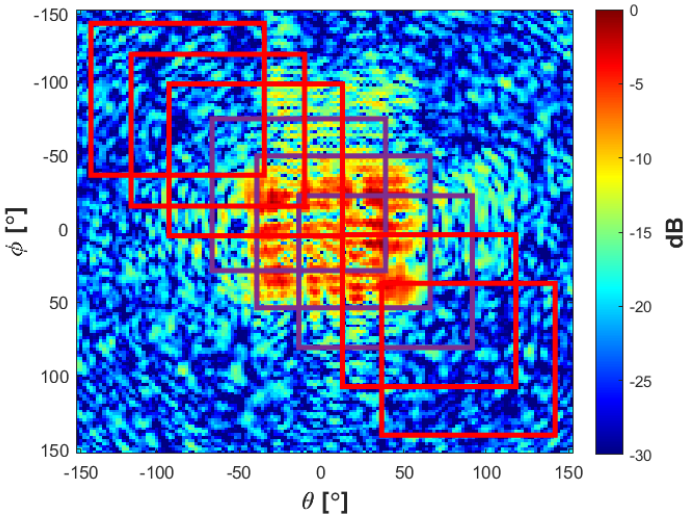

Figure 5.4.3: The amplitude of the measured S_{11} across the entire scanned area, with squares marking the patches along the diagonal.

- **Path 3**: Utilizing the exact patches shown in Figure 5.4.3, i.e., the magnitude of the complex numbers of the reflection coefficients $|S_{11}|$.

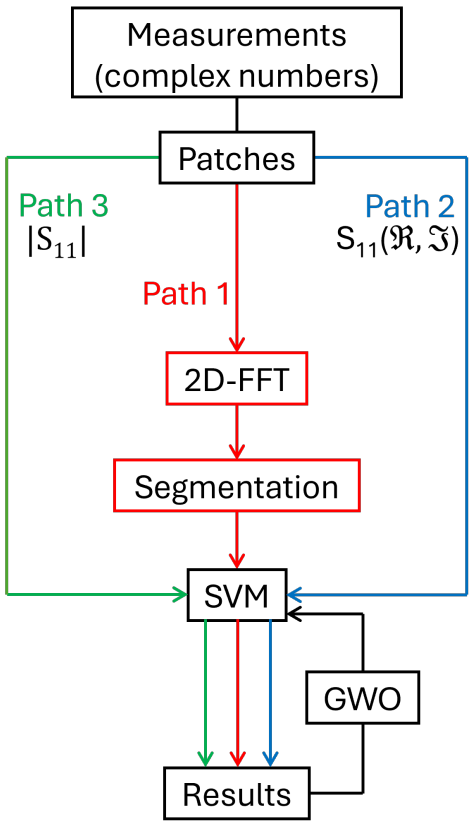

Figure 5.4.4: The complete Flowchart

The three different paths are illustrated in the workflow in Fig. 5.4.4. Our goal is to determine the most

effective classification scheme among them. The first one is based on image processing.

5.5 Classification and Results

From the three approaches, we obtain three distinct datasets: Dataset 1, derived from the processed segmented images in the first path; Dataset 2, containing the raw real and imaginary parts of the patches without preprocessing (path 2); and Dataset 3, consisting of only the magnitude data of these patches, also without preprocessing (path 3). In total, we obtain 4545 classification samples corresponding to the 15 samples shown in Fig. 5.4.1 (7 walnuts and 8 almonds) for each dataset. We randomly select 6 samples (3 walnuts and 3 almonds) for the training phase while the remaining 9 samples (4 walnuts and 5 almonds) are for the test.

5.5.1 Results for Path 1

Before selecting a classifier, it is important to analyze the distribution of the dataset using the PCA. The projection of the PCA results onto the first three principal components for Dataset 1, shown in Figure 5.5.1, reveals a strong nonlinear relationship between the two classes (almonds and walnuts) in both the training and test sets. These three components account for 66% and 62% of the variance in the training and test sets, respectively, indicating that they capture the most significant information about the dataset. The PCA results highlight the need for selecting a nonlinear machine learning algorithm. Therefore, we implement the non-linear SVM, as it has demonstrated strong performance and robustness in similar applications [104], as well as in our previous work on MW detection of contaminants in food and beverage products [111, 162, 163], as introduced in the previous chapter. Additionally, we use the GWO optimization algorithm to find the optimal hyperparameters (C^*, γ^*) that define the hyperplane for separating the different classes.

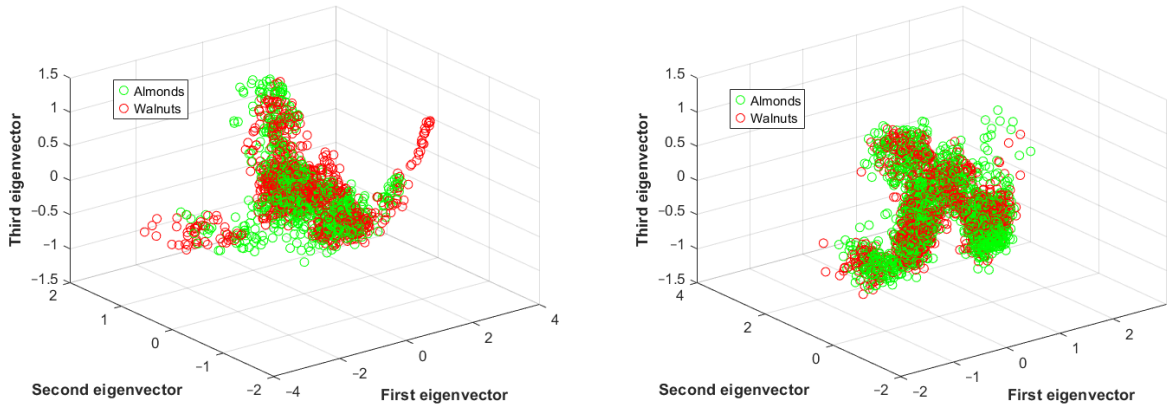

Figure 5.5.1: PCA results projected onto the three principal eigenvectors for Dataset 1: (a) Training set, (b) Test set.

The training and test sets contain 1818 and 2727 patches, respectively, across the three paths. We assign +1 to almond patches and -1 to walnut patches. To enhance the robustness of the classification,

we use the cross-validation method. Cross-validation is a technique for evaluating model performance by testing it on different subsets of the data. In this study, we use 6-fold cross-validation, where the dataset is divided into six distinct subsets. The model is trained and evaluated six times, each time using a different fold as the test set, ensuring that every part of the dataset is used for both training and testing. After optimizing (C^*, γ^*) using the Grey Wolf Optimizer (GWO), the cross-validation accuracy for the training dataset in Path 1 is $80\% \pm 5\%$.

The confusion matrix in Table 5.5.1 presents the classification results, showing an accuracy of 52.5%. A total of 628 out of 1515 patches from almond samples are misclassified, while 669 out of 1212 patches from walnut samples are also misclassified. This result indicates an overfitting problem, as the classification accuracy does not align with the validation accuracy.

Table 5.5.1: Confusion matrices for Datasets 1.

	Positive	Negative
Positive	887	628
Negative	669	543

5.5.2 Results for Path 2

Figure 5.5.2 shows the projection of the PCA results onto the first three principal components for Dataset 2, revealing a strong nonlinear relationship between the two classes (almonds and walnuts) in both the training and test sets. However, unlike Dataset 1, these three components capture only 10% of the variance, suggesting that they do not accurately represent the true distribution of the data.

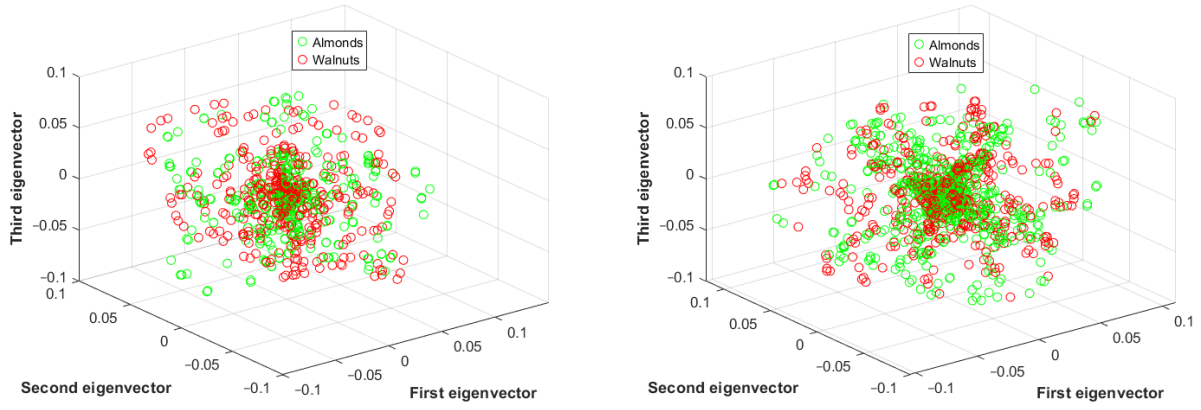

(a) (b)

Figure 5.5.2: PCA results projected onto the three principal eigenvectors for Dataset 2: (a) Training set, (b) Test set.

The confusion matrix in Table 5.5.2 summarizes the classification results, revealing an accuracy of 54.6%. Among the almond samples, 597 out of 1515 patches are misclassified, while 640 out of 1212 walnut patches are misclassified. The accuracy is similar to that of Dataset 1, and the same overfitting issue is observed, as the classification accuracy deviates from the validation accuracy.

Table 5.5.2: Confusion matrices for Datasets 2.

	Positive	Negative
Positive	918	597
Negative	640	572

5.5.3 Results for Path 3

Figure 5.5.3 illustrates the PCA projection onto the first three principal components for Dataset 3, highlighting a strong and similar nonlinear relationship between the two classes (almonds and walnuts) in both the training and test sets. However, these three components account for only 51% of the variance, indicating that they do not fully capture the true data distribution, as the first three components should capture at least 70% – 80% of the variance for a reliable visualization.

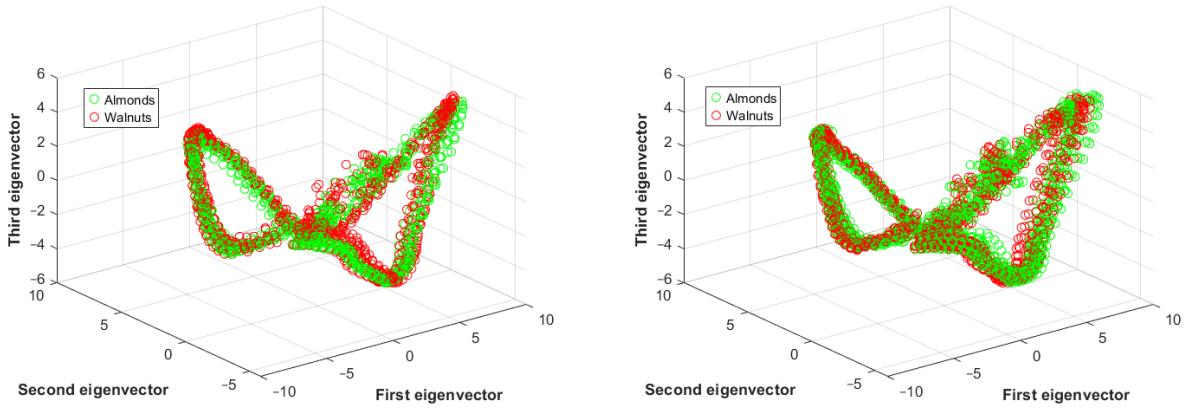

(a) (b)

Figure 5.5.3: PCA results projected onto the three principal eigenvectors for Dataset 3: (a) Training set, (b) Test set.

Table 5.5.3 presents the confusion matrix for the classification results, revealing an accuracy of 43.6%. Among the almond samples, 624 out of 1515 patches are misclassified, while 913 out of 1212 patches from walnut samples are also incorrectly classified. We still observe the same overfitting problem as in Datasets 1 and 2, further highlighting the model's inability to generalize, likely due to the increased complexity of the data distribution.

Table 5.5.3: Confusion matrices for Datasets 3.

	Positive	Negative
Positive	891	624
Negative	913	299

5.5.4 Threshold-Based Classification and Patch Accuracy Analysis

It is important to note that, in this application, each sample is represented by 303 patches. To classify a sample as either a walnut or an almond, all 303 patches must be correctly classified. Achieving 100%

accuracy is challenging, as it requires every patch to be accurately identified in all 303 instances. However, if only a portion of the patches are correctly classified, such as 200 out of 303, it becomes unclear how to determine the sample's true class. To address this, we introduce the concept of a threshold, which defines the minimum number of correctly classified patches required to confidently assign a sample to a specific class. If the number of correctly classified patches exceeds this threshold, the sample is classified accordingly. Tables 5.5.4 present the correctly classified and misclassified patches for each almond and

Table 5.5.4: The correctly and incorrectly classified patches for each walnut and almond in the three datasets

	Dataset 1		Dataset 2		Dataset 3	
	Almond	Walnut	Almond	Walnut	Almond	Walnut
Almond 1	281	22	303	0	298	5
Almond 2	252	51	303	0	302	1
Almond 3	242	61	302	1	286	17
Almond 4	43	260	0	303	3	300
Almond 5	68	235	9	294	2	301
Walnut 1	146	157	150	153	278	25
Walnut 2	143	160	103	200	270	33
Walnut 3	121	182	84	219	63	240
Walnut 4	258	45	302	1	302	1

walnut in the test dataset. The most obvious way to decide whether a nut is well classified is to look at the class to which the majority of patches belong. This is equivalent to put a threshold at 50%. In this case, the classification accuracy for nuts reaches 66% for Datasets 1 and 2, and 44% for Dataset 3. However, a 50% threshold means the decision is made based on a single patch, leaving no security margin. Thus, a higher threshold is more appropriate for improving accuracy. Determining the exact threshold is not straightforward, as it requires a lot of measurements. To address this, we manually adjust the threshold, starting from 50%. To illustrate the impact of the threshold on the final classification results, Figs. 5.5.4, 5.5.5, and 5.5.6 present the performance as the threshold is gradually increased from 50% to 100% across the three classification schemes, corresponding to Datasets 1, 2, and 3.

By comparing the number of well-classified almonds between Dataset 1 (Fig. 5.5.4), Dataset 2 (Fig. 5.5.5), and Dataset 3 (Fig. 5.5.6), we observe, as expected, that increasing the threshold decreases the number of well-classified nuts. Nevertheless, the classification scheme 2 performs better. For example, with a 90% threshold, three out of five almonds are correctly classified in Dataset 2, while only one is correctly classified in Dataset 1, and two in Dataset 3. The same applies to walnuts, with two out of four correctly classified in Dataset 2, and only one in Datasets 1 and 3 when the threshold is set to 60%.

This demonstrates the superiority of the second classification scheme, which directly classifies the real and imaginary parts of the measured data. Additionally, this study highlights the challenge of determining an optimal threshold value, especially given the limited number of measurements, which makes it difficult to accurately identify a threshold that maximizes correct classifications.

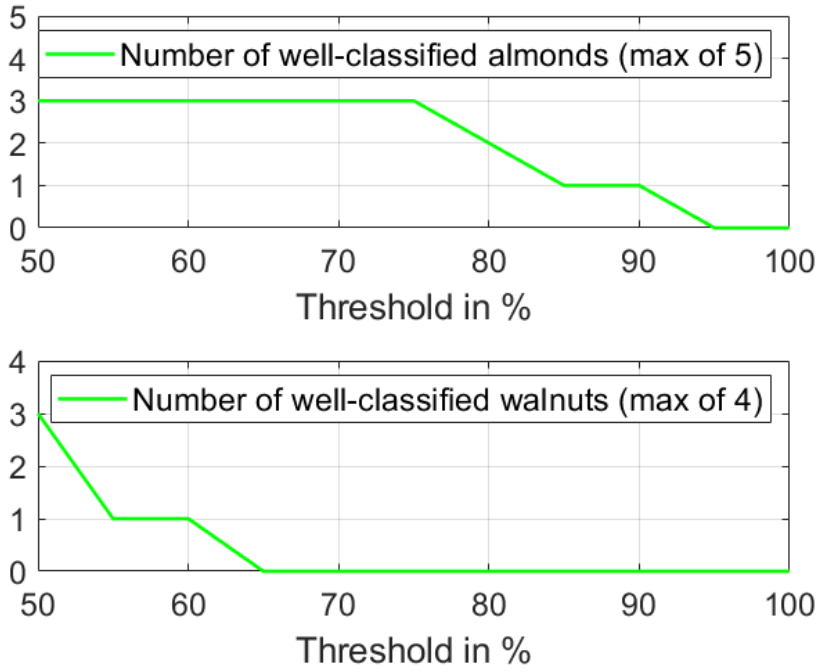

Figure 5.5.4: The number of well-classified almonds and walnuts as a function of the threshold for Dataset 1.

5.6 Conclusion and Challenges

In this chapter, we explore the feasibility of using mmW imaging combined with SVM classifier to classify two types of in-shell seeds: almonds and walnuts. We propose three classification schemes: one based on 2D-FFT image processing and two others that directly utilize the real-imaginary components and magnitude of the measured S_{11}, respectively. The presence of the shell makes classification more challenging compared to soft fruits, leading to a drop in accuracy from 100% for soft fruits [104] to 66% for the best-performing scheme in this study. The results are influenced by the threshold, which is currently set manually. Future work will focus on developing an automated method for threshold selection. To achieve better generalization, expanding the dataset with additional measurements will be necessary.

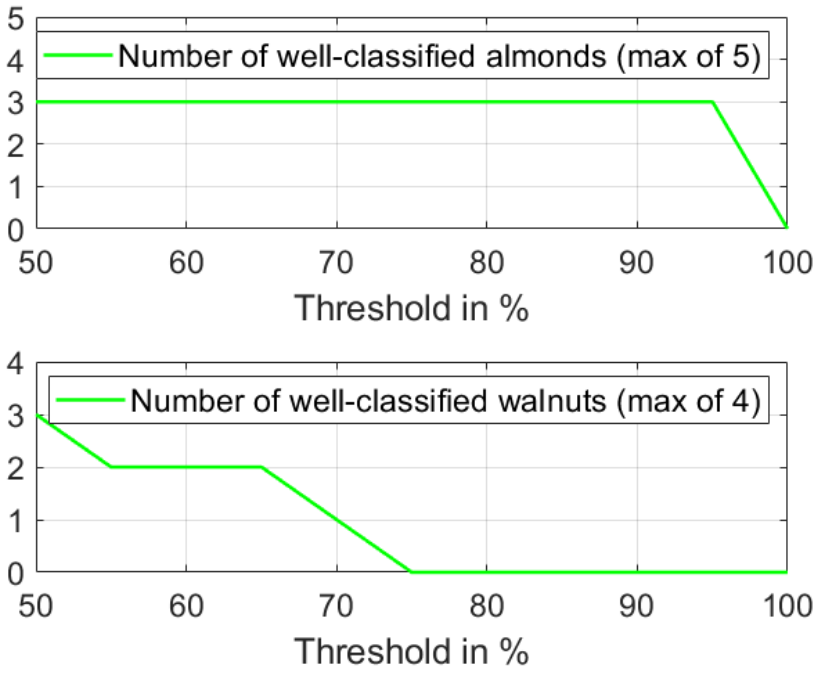

Figure 5.5.5: The number of well-classified almonds and walnuts as a function of the threshold for Dataset 2.

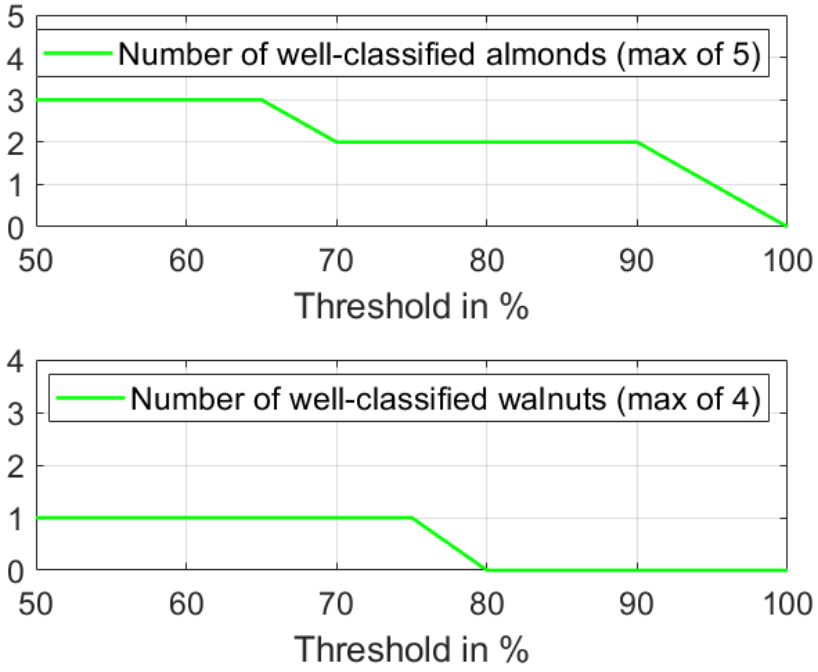

Figure 5.5.6: The number of well-classified almonds and walnuts as a function of the threshold for Dataset 3.

6 Conclusion and Perspectives

6.1 Conclusion

This thesis explores the application of MW and mmW sensing technologies combined with machine learning (ML) for non-destructive food quality and safety assessment. The research addresses the critical challenge of detecting physical contaminants in food and beverage products, where existing techniques (X-ray, metal detectors, NIR, and THz imaging) exhibit limitations such as low penetration depth and material detection constraints.

The study builds upon MWI principles and sensing techniques to develop an inline monitoring system capable of detecting contaminants in packaged food and beverage products. This system is designed for seamless integration into production lines, utilizing electromagnetic wave propagation, optimal antenna configurations, and ML-based classification techniques (SVM and MLP).

The key contributions of this work include:

- **Proof-of-concept validation:** MW sensing is validated for oil-based and water-based products.
- **Application of ML classification:** SVM and MLP algorithms are employed for binary and multiclass contaminant detection.
- **Real-world validation:** The approach is tested on commercial food and beverage products, demonstrating high classification accuracy.

Additionally, this research extends MW sensing to mmW imaging, applying it to in-shell seed classification (almonds vs. walnuts). This case study reveals the challenges posed by shells, which reduce classification accuracy compared to soft fruits. The study proposes three classification schemes and highlights the need for further improvements in threshold selection and dataset expansion.

6.2 Perspective and Future Work

While the proposed MW sensing system and ML integration demonstrate promising results, several challenges remain:

- **Dataset limitations:** The training dataset size is minimal for achieving acceptable classification accuracy. Future work will focus on increasing the dataset size to improve generalization.
- **Multiclass classification challenges:** Adding more contaminants reduces classification accuracy. To address this, future research will explore other ML algorithms and optimization techniques.

- **Miniaturize the MW sensing system:** More compact devices are better suited for industrial applications.
- **Real-world industrial testing:** Although laboratory validation is successful, real-world testing in industrial environments remains necessary to refine system performance.
- **Expansion to diverse food products:** The system will be tested across a broader range of food and beverage products to enhance applicability and robustness.
- **Automation of threshold selection in case of in-shell seed classification:** The current method includes manual threshold adjustments, impacting accuracy. Future work will develop automated thresholding techniques.

By addressing these challenges, this research aims to further improve MW sensing and ML-based classification for real-time, inline food safety monitoring, offering a viable alternative to existing technologies.

7 Bibliography

[1] C. I. of Food Safety, "Food safety and the types of food contamination." https://blog.foodsafety.ca/food-safety-and-types-food-contamination. Accessed: 2024-08-28.

[2] traqfood, "The different types of food contamination." https://www.traqfood.com/en/blog-haccp-method/haccp-measures/the-regulatory-obligations-of-the-restaurateur/article/the-different-types-of-food-contamination/. Accessed: 2024-08-28.

[3] S. Wilkinson, "Types of food contamination." https://cpdonline.co.uk/knowledge-base/food-hygiene/types-of-food-contamination/. Accessed: 2024-08-28.

[4] flexxray, "2024 physical contamination in food." https://flexxray.com/lp/physical-contamination-in-food-benchmark-report-2024/. Accessed: 2024-08-28.

[5] safefood360, "How do physical hazards occur in the food safety process." https://safefood360.com/blog/how-do-physical-hazards-occur-in-the-food-safety-process/. Accessed: 2024-08-28.

[6] masterpackgroup, "3 common contamination risks in food packaging." https://blog.masterpackgroup.com/3-common-contamination-risks-in-food-packaging. Accessed: 2024-08-28.

[7] J. Bovay, "Food safety, reputation, and regulation," *Applied Economic Perspectives and Policy*, vol. 45, no. 2, pp. 684–704, 2023.

[8] M. Pakdel, A. Olsen, and E. M. S. Bar, "A review of food contaminants and their pathways within food processing facilities using open food processing equipment," *Journal of Food Protection*, vol. 86, no. 12, p. 100184, 2023.

[9] Clarifrui, "What a difference a defect makes: Streamlining decision-making with a platform for detecting fresh fruit and vegetable defects and evaluating quality." https://www.clarifruit.com/blog/what-a-difference-a-defect-makes-streamlining-decision-making-with-a-platform-for-detecting-fresh-fruit-and-vegetable-defects-and-evaluating-quality/. Accessed: 2024-08-28.

[10] M. Soltani Firouz and H. Sardari, "Defect detection in fruit and vegetables by using machine vision systems and image processing," *Food Engineering Reviews*, vol. 14, no. 3, pp. 353–379, 2022.

[11] myhaccp, "Establish a monitoring system." https://myhaccp.food.gov.uk/help/guidance/principle-4-establish-a-monitoring-system. Accessed: 2024-08-28.

[12] food safety magazine, "On-line monitoring tools for food processing." https://www.food-safety.com/articles/5410-on-line-monitoring-tools-for-food-processing. Accessed: 2024-08-28.

[13] W. Labs, "Inline monitoring aids in food safety and quality." https://www.foodengineeringmag.com/articles/90659-inline-monitoring-aids-in-food-safety-and-quality. Accessed: 2024-08-28.

[14] kpmanalytics, "At-line nir analysis to minimize over-formulation costs in food production." https://www.kpmanalytics.com/articles-insights/at-line-nir-analysis-to-minimize-over-formulation-costs-in-food-production. Accessed: 2024-08-28.

[15] P. Bhatt, S. Mutturi, and M. Thakur, "Spectroscopy based in-line monitoring and control of food quality and safety," in *Engineering Aspects of Food Quality and Safety*, pp. 339–382, Springer, 2023.

[16] Sesotec, "X-ray inspection systems in food processing plants." https://www.sesotec.com/na/en-US/products/groups/x-ray-inspection-systems-for-packaged-products. Accessed: 2024-08-28.

[17] M. Graves, A. Smith, and B. Batchelor, "Approaches to foreign body detection in foods," *Trends in Food Science & Technology*, vol. 9, no. 1, pp. 21–27, 1998.

[18] D. Mery, I. Lillo, H. Loebel, V. Riffo, A. Soto, A. Cipriano, and J. M. Aguilera, "Automated fish bone detection using x-ray imaging," *Journal of Food Engineering*, vol. 105, no. 3, pp. 485–492, 2011.

[19] R. P. Haff and N. Toyofuku, "X-ray detection of defects and contaminants in the food industry," *Sensing and Instrumentation for Food Quality and Safety*, vol. 2, pp. 262–273, 2008.

[20] Scintacor, "The use of x-rays in food inspection." https://scintacor.com/the-use-of-x-rays-in-food-inspection/. Accessed: 2024-08-28.

[21] Manitoba, "X-ray inspection systems in food processing plants." https://www.manitoba.ca/agriculture/food-safety/at-the-food-processor/x-ray-inspection-systems.html. Accessed: 2024-08-28.

[22] E. Jackson and R. Haff, "X-ray detection and sorting of olives damaged by fruit fly," in *2006 ASAE Annual Meeting*, p. 1, American Society of Agricultural and Biological Engineers, 2006.

[23] Sesotec, "Basics of metal detection in the food industry." https://www.sesotec.com/emea/en/resources/expertise/metal-detection-in-the-food-industry. Accessed: 2024-08-28.

[24] H. Kilifarev, "Development of a monitoring device for metal fragments in food products–hardware," in *BIO Web of Conferences*, vol. 102, p. 03009, EDP Sciences, 2024.

[25] K. Payne, C. A. O'Bryan, J. A. Marcy, and P. G. Crandall, "Detection and prevention of foreign material in food: A review," *Heliyon*, 2023.

[26] Yamato, "An 8-step guide to metal detecting in the food industry and why it's so important." https://yamatoscale.co.za/public/metal-detecting-guide-food-industry. Accessed: 2024-08-28.

[27] B. Liu and W. Zhou, "The research of metal detectors using in food industry," in *Proceedings of 2011 International Conference on Electronics and Optoelectronics*, vol. 4, pp. V4–43, IEEE, 2011.

[28] N. Food, "Understanding near infrared (nir) spectroscopy in food testing." https://www.newfoodmagazine.com/article/243932/understanding-nir-spectroscopy-food-testing/. Accessed: 2024-08-28.

[29] W. Wang and J. Paliwal, "Near-infrared spectroscopy and imaging in food quality and safety," *Sensing and instrumentation for food quality and safety*, vol. 1, pp. 193–207, 2007.

[30] X. Fu and Y. Ying, "Food safety evaluation based on near infrared spectroscopy and imaging: a review," *Critical Reviews in Food Science and Nutrition*, vol. 56, no. 11, pp. 1913–1924, 2016.

[31] J.-L. Li, D.-W. Sun, and J.-H. Cheng, "Recent advances in nondestructive analytical techniques for determining the total soluble solids in fruits: a review," *Comprehensive Reviews in Food Science and Food Safety*, vol. 15, no. 5, pp. 897–911, 2016.

[32] M. Manley, "Near-infrared spectroscopy and hyperspectral imaging: non-destructive analysis of biological materials," *Chemical Society Reviews*, vol. 43, no. 24, pp. 8200–8214, 2014.

[33] E. Guzmán, V. Baeten, J. A. F. Pierna, and J. A. García-Mesa, "Infrared machine vision system for the automatic detection of olive fruit quality," *Talanta*, vol. 116, pp. 894–898, 2013.

[34] Terasense, "Terahertz food inspection." https://terasense.com/applications/terahertz-food-inspection/. Accessed: 2024-08-28.

[35] C. Jördens and M. Koch, "Detection of foreign bodies in chocolate with pulsed terahertz spectroscopy," *Optical Engineering*, vol. 47, no. 3, pp. 037003–037003, 2008.

[36] A. A. Gowen, C. O'Sullivan, and C. P. O'Donnell, "Terahertz time domain spectroscopy and imaging: Emerging techniques for food process monitoring and quality control," *Trends in Food Science & Technology*, vol. 25, no. 1, pp. 40–46, 2012.

[37] H. Ge, M. Lv, X. Lu, Y. Jiang, G. Wu, G. Li, L. Li, Z. Li, and Y. Zhang, "Applications of thz spectral imaging in the detection of agricultural products," in *Photonics*, vol. 8, p. 518, MDPI, 2021.

[38] Y. Fu, Y. Ren, and D.-W. Sun, "Novel analysis of food processes by terahertz spectral imaging: A review of recent research findings," *Trends in Food Science & Technology*, p. 104463, 2024.

[39] L. Afsah-Hejri, P. Hajeb, P. Ara, and R. J. Ehsani, "A comprehensive review on food applications of terahertz spectroscopy and imaging," *Comprehensive Reviews in Food Science and Food Safety*, vol. 18, no. 5, pp. 1563–1621, 2019.

[40] S. Zappia, L. Crocco, and I. Catapano, "Thz imaging for food inspections: A technology review and future trends," in *Terahertz Technology* (B. You and J.-Y. Lu, eds.), ch. 5, Rijeka: IntechOpen, 2021.

[41] G.-J. Kim, J.-I. Kim, S.-G. Jeon, J. Kim, K.-K. Park, and C.-H. Oh, "Enhanced continuous-wave terahertz imaging with a horn antenna for food inspection," *Journal of Infrared, Millimeter, and Terahertz Waves*, vol. 33, pp. 657–664, 2012.

[42] G. Ridler, "Plastic contamination and glass shards spark food recalls." https://www.foodmanufacture.co.uk/Article/2023/10/09/plastic-contamination-and-glass-shards-spark-food-recalls. Accessed: 2024-08-28.

[43] J. Whitworth, "Eu food and beverage recalls rise in early 2023." https://www.foodsafetynews.com/2023/06/eu-food-and-beverage-recalls-rise-in-early-2023/. Accessed: 2024-08-28.

[44] USDA, "Recalls and public health alerts." https://www.fsis.usda.gov/recalls. Accessed: 2024-08-28.

[45] FDA, "Recalls, market withdrawals, and safety alerts." https://www.fda.gov/safety/recalls-market-withdrawals-safety-alerts. Accessed: 2024-08-28.

[46] L. E. Larsen and J. H. Jacobi, "Microwave scattering parameter imagery of an isolated canine kidney," *Medical physics*, vol. 6, no. 5, pp. 394–403, 1979.

[47] J. H. Jacobi and L. E. Larsen, "Microwave time delay spectroscopic imagery of isolated canine kidney," *Medical Physics*, vol. 7, no. 1, pp. 1–7, 1980.

[48] J. C. Bolomey, A. Izadnegahdar, L. Jofre Roca, C. PICHOT DU MEZERAY, and G. Peronnet, "Microwave diffraction tomography for biomedical applications," *IEEE Transactions on Microwave Theory and Techniques*, vol. 30, no. 11, pp. 1998–2000, 1982.

[49] P. M. Meaney, K. D. Paulsen, A. Hartov, and R. K. Crane, "An active microwave imaging system for reconstruction of 2-d electrical property distributions," *IEEE Transactions on Biomedical Engineering*, vol. 42, no. 10, pp. 1017–1026, 1995.

[50] L. Jofre, M. S. Hawley, A. Broquetas, E. de Los Reyes, M. Ferrando, and A. R. Elias-Fuste, "Medical imaging with a microwave tomographic scanner," *IEEE Transactions on Biomedical Engineering*, vol. 37, no. 3, pp. 303–312, 1990.

[51] E. J. Bond, X. Li, S. C. Hagness, and B. D. Van Veen, "Microwave imaging via space-time beamforming for early detection of breast cancer," *IEEE Transactions on Antennas and Propagation*, vol. 51, no. 8, pp. 1690–1705, 2003.

[52] M. R. Casu, M. Vacca, J. A. Tobon, A. Pulimeno, I. Sarwar, R. Solimene, and F. Vipiana, "A cots-based microwave imaging system for breast-cancer detection," *IEEE transactions on biomedical circuits and systems*, vol. 11, no. 4, pp. 804–814, 2017.

[53] R. Scapaticci, J. Tobon, G. Bellizzi, F. Vipiana, and L. Crocco, "Design and numerical characterization of a low-complexity microwave device for brain stroke monitoring," *IEEE Transactions on Antennas and Propagation*, vol. 66, no. 12, pp. 7328–7338, 2018.

[54] P.-H. Tournier, M. Bonazzoli, V. Dolean, F. Rapetti, F. Hecht, F. Nataf, I. Aliferis, I. El Kanfoud, C. Migliaccio, M. de Buhan, M. Darbas, S. Semenov, and C. Pichot, "Numerical modeling and high-speed parallel computing: New perspectives on tomographic microwave imaging for brain stroke detection and monitoring," *IEEE Antennas and Propagation Magazine*, vol. 59, no. 5, pp. 98–110, 2017.

[55] V. L. Coli, P.-H. Tournier, V. Dolean, I. El Kanfoud, C. Pichot, C. Migliaccio, and L. Blanc-Féraud, "Detection of simulated brain strokes using microwave tomography," *IEEE journal of electromagnetics, RF and microwaves in medicine and biology*, vol. 3, no. 4, pp. 254–260, 2019.

[56] S. A. Rezaeieh, A. Zamani, and A. Abbosh, "3-d wideband antenna for head-imaging system with performance verification in brain tumor detection," *IEEE Antennas and Wireless Propagation Letters*, vol. 14, pp. 910–914, 2014.

[57] K. Lalitha and J. Manjula, "Non-invasive microwave head imaging to detect tumors and to estimate their size and location," *Physics in Medicine*, vol. 13, p. 100047, 2022.

[58] J. A. Tobon Vasquez, R. Scapaticci, G. Turvani, G. Bellizzi, D. O. Rodriguez-Duarte, N. Joachimowicz, B. Duchêne, E. Tedeschi, M. R. Casu, L. Crocco, *et al.*, "A prototype microwave system for 3d brain stroke imaging," *Sensors*, vol. 20, no. 9, p. 2607, 2020.

[59] R. Zoughi, *Microwave non-destructive testing and evaluation principles*, vol. 4. Springer Science & Business Media, 2000.

[60] D. J. Daniels, *EM detection of concealed targets*, vol. 196. John Wiley & Sons, 2009.

[61] J.-C. Bolomey and F. E. Gardiol, *Engineering applications of the modulated scatterer technique*. Artech House, 2001.

[62] S. Clerjon and J. Damez, "Microwave sensing for meat and fish structure evaluation," *Measurement Science and Technology*, vol. 18, no. 4, p. 1038, 2007.

[63] X. Bohigas, R. Amigó, and J. Tejada, "Characterisation of sugar content in yoghurt by means of microwave spectroscopy," *Food Research International*, vol. 41, no. 1, pp. 104–109, 2008.

[64] E. Cheng, M. Fareq, A. Shahriman, R. Mohd Afendi, Y. Lee, S. Khor, W. Tan, M. Nashrul Fazli, A. Abdullah, and M. Jusoh, "Development of microstrip patch antenna sensing system for salinity and sugar detection in water," *Int. J. Mech. Mechatronics Eng*, vol. 15, no. 5, pp. 31–36, 2014.

[65] J. A. T. Vasquez, R. Scapaticci, G. Turvani, M. Ricci, L. Farina, A. Litman, M. R. Casu, L. Crocco, and F. Vipiana, "Noninvasive inline food inspection via microwave imaging technology: An application example in the food industry," *IEEE Antennas and Propagation Magazine*, vol. 62, no. 5, pp. 18–32, 2020.

[66] A. A. Gibson, S. K. Ng, B. B. Noh, H. S. Chua, A. D. Haigh, G. Parkinson, P. Ainsworth, and A. Plunkett, "An overview of microwave techniques for the efficient measurement of food materials," *Food Manufacturing Efficiency*, vol. 2, no. 1, p. 35, 2008.

[67] Z. Meng, Z. Wu, and J. Gray, "Microwave sensor technologies for food evaluation and analysis: Methods, challenges and solutions," *Transactions of the Institute of Measurement and Control*, vol. 40, no. 12, pp. 3433–3448, 2018.

[68] C. Bircan and S. Barringer, "Salt-starch interactions as evidenced by viscosity and dielectric property measurements," *Journal of food science*, vol. 63, no. 6, pp. 983–986, 1998.

[69] M. Castro-Giráldez, M.-C. Aristoy, F. Toldrá, and P. Fito, "Microwave dielectric spectroscopy for the determination of pork meat quality," *Food research international*, vol. 43, no. 10, pp. 2369–2377, 2010.

[70] S. K. Ng, A. Gibson, G. Parkinson, A. Haigh, P. Ainsworth, and A. Plunkett, "Bimodal method of determining fat and salt content in beef products by microwave techniques," *IEEE Transactions on Instrumentation and Measurement*, vol. 58, no. 10, pp. 3778–3787, 2009.

[71] S. Clerjon and J.-L. Damez, "Microwave sensing for an objective evaluation of meat ageing," *Journal of Food Engineering*, vol. 94, no. 3-4, pp. 379–389, 2009.

[72] P. G. Bartley, S. O. Nelson, R. W. McClendon, and S. Trabelsi, "Determining moisture content of wheat with an artificial neural network from microwave transmission measurements," *IEEE transactions on instrumentation and measurement*, vol. 47, no. 1, pp. 123–126, 1998.

[73] S. Trabelsi and S. O. Nelson, "Free-space measurement of dielectric properties of cereal grain and oilseed at microwave frequencies," *Measurement Science and Technology*, vol. 14, no. 5, p. 589, 2003.

[74] R. Knöchel, F. Daschner, and W. Taute, "Resonant microwave sensors for instantaneous determination of moisture in foodstuffs," *Food control*, vol. 12, no. 7, pp. 447–458, 2001.

[75] P. Leekul, T. Limpiti, T. Tantisopharak, P. Yoiyod, S. Chivapreecha, C. Phongcharoenpanich, and M. Krairiksh, "Remote sensing of the physical qualities of fruits," in *2014 Asia-Pacific Microwave Conference*, pp. 1113–1114, 2014.

[76] S. Suttapa, "Microwave sensor response in relation to durian maturity," in *Proc. CIGR Section VI International Symposium on Food Processing and Monitoring Technology in Bioprocesses and Food Quality Management, Potsdam, Germany, Sept. 2009*, 2009.

[77] J. A. Tobon Vasquez, R. Scapaticci, G. Turvani, G. Bellizzi, N. Joachimowicz, B. Duchêne, E. Tedeschi, M. R. Casu, L. Crocco, and F. Vipiana, "Design and experimental assessment of a 2d microwave imaging system for brain stroke monitoring," *International Journal of Antennas and Propagation*, vol. 2019, no. 1, p. 8065036, 2019.

[78] M. Bertero, P. Boccacci, and C. De Mol, *Introduction to inverse problems in imaging*. CRC press, 2021.

[79] N. Zeni, L. Crocco, M. Cavagnaro, and G. Bellizzi, "A simple differential microwave imaging approach for in-line inspection of food products," *Sensors*, vol. 23, no. 2, p. 779, 2023.

[80] G. Bellizzi, A. Buzzin, L. Crocco, A. Mastrandrea, N. Zeni, S. Zumbo, and M. Cavagnaro, "A simple microwave imaging system for food product inspection through a symmetry-based microwave imaging approach," *Sensors*, vol. 24, no. 1, p. 99, 2023.

[81] D. Henry, H. Aubert, T. Véronèse, and É. Serrano, "Remote estimation of intra-parcel grape quantity from three-dimensional imagery technique using ground-based microwave fmcw radar," *IEEE Instrumentation & Measurement Magazine*, vol. 20, no. 3, pp. 20–24, 2017.

[82] A. Massa, G. Oliveri, M. Salucci, N. Anselmi, and P. Rocca, "Learning-by-examples techniques as applied to electromagnetics," *Journal of Electromagnetic Waves and Applications*, vol. 32, no. 4, pp. 516–541, 2018.

[83] A. Massa, D. Marcantonio, X. Chen, M. Li, and M. Salucci, "Dnns as applied to electromagnetics, antennas, and propagation—a review," *IEEE Antennas and Wireless Propagation Letters*, vol. 18, no. 11, pp. 2225–2229, 2019.

[84] A. E. Maxwell, T. A. Warner, and F. Fang, “Implementation of machine-learning classification in remote sensing: An applied review,” *International journal of remote sensing*, vol. 39, no. 9, pp. 2784–2817, 2018.

[85] S. Caorsi and G. Cevini, “An electromagnetic approach based on neural networks for the gpr investigation of buried cylinders,” *IEEE Geoscience and Remote Sensing Letters*, vol. 2, no. 1, pp. 3–7, 2005.

[86] S. Cashman, O. Korostynska, A. Shaw, P. Lisboa, and L. Conroy, “Detecting the presence and concentration of nitrate in water using microwave spectroscopy,” *IEEE Sensors Journal*, vol. 17, no. 13, pp. 4092–4099, 2017.

[87] R. K. Amineh, M. Ravan, and D. Tandel, “Detection of water pollutants with a nonuniform array of microwave sensors,” *IEEE Transactions on Instrumentation and Measurement*, vol. 72, pp. 1–11, 2023.

[88] L. Harrsion, M. Ravan, D. Tandel, K. Zhang, T. Patel, and R. K. Amineh, “Material identification using a microwave sensor array and machine learning,” *Electronics*, vol. 9, no. 2, p. 288, 2020.

[89] N. Kazemi, M. Abdolrazzaghi, P. E. Light, and P. Musilek, “In–human testing of a non-invasive continuous low–energy microwave glucose sensor with advanced machine learning capabilities,” *Biosensors and Bioelectronics*, vol. 241, p. 115668, 2023.

[90] V. Mariano, J. A. Tobon Vasquez, M. R. Casu, and F. Vipiana, “Brain stroke classification via machine learning algorithms trained with a linearized scattering operator,” *Diagnostics*, vol. 13, no. 1, p. 23, 2022.

[91] A. Hossain, M. T. Islam, and A. F. Almutairi, “A deep learning model to classify and detect brain abnormalities in portable microwave based imaging system,” *Scientific Reports*, vol. 12, no. 1, p. 6319, 2022.

[92] S. A. AlShehri and S. Khatun, “Uwb imaging for breastr cancer detection using neural network,” *Progress In Electromagnetics Research C*, vol. 7, pp. 79–93, 2009.

[93] I. T. Rekanos, “Neural-network-based inverse-scattering technique for online microwave medical imaging,” *IEEE transactions on magnetics*, vol. 38, no. 2, pp. 1061–1064, 2002.

[94] V. Leemans, H. Magein, and M.-F. Destain, “Defect segmentation on ‘jonagold’apples using colour vision and a bayesian classification method,” *Computers and Electronics in Agriculture*, vol. 23, no. 1, pp. 43–53, 1999.

[95] Q. Li, M. Wang, and W. Gu, “Computer vision based system for apple surface defect detection,” *Computers and electronics in agriculture*, vol. 36, no. 2-3, pp. 215–223, 2002.

[96] L. J. Rozario, T. Rahman, and M. S. Uddin, “Segmentation of the region of defects in fruits and vegetables,” *International Journal of Computer Science and Information Security*, vol. 14, no. 5, p. 399, 2016.

[97] P. Mehl, K. Chao, M. Kim, and Y. Chen, “Detection of defects on selected apple cultivars using hyperspectral and multispectral image analysis,” *Applied engineering in agriculture*, vol. 18, no. 2, p. 219, 2002.

[98] B. Bennedsen and D. Peterson, “Performance of a system for apple surface defect identification in near-infrared images,” *Biosystems engineering*, vol. 90, no. 4, pp. 419–431, 2005.

[99] C. Migliaccio, B. Nguyen, C. Pichot, N. Yonemoto, K. Yamamoto, K. Yamada, H. Nasui, W. Mayer, A. Gronau, and W. Menzel, “Millimeter-wave radar for rescue helicopters,” in *2006 9th International Conference on Control, Automation, Robotics and Vision*, pp. 1–6, IEEE, 2006.

[100] K. Mazouni, A. Zeitler, J. Lanteri, C. Pichot, J.-Y. Dauvignac, C. Migliaccio, N. Yonemoto, A. Kohmura, and S. Futatsumori, “76.5 ghz millimeter-wave radar for foreign objects debris detection on airport runways,” *International Journal of Microwave and Wireless Technologies*, vol. 4, no. 3, pp. 317–326, 2012.

[101] F. Nsengiyumva, C. Migliaccio, L. Brochier, J. Lanteri, J.-Y. Dauvignac, and C. Pichot, “90 ghz, 3-d scattered field measurements for investigation of foreign object debris,” *IEEE Transactions on Antennas and Propagation*, vol. 67, no. 9, pp. 6217–6222, 2019.

[102] R. Grisot, P. Laurent, C. Migliaccio, J.-Y. Dauvignac, M. Brulc, C. Chiquet, and J.-P. Caruana, “Monitoring of heart movements using an fmcw radar and correlation with an ecg,” *IEEE Transactions on Radar Systems*, vol. 1, pp. 423–434, 2023.

[103] F. Zidane, J. Lanteri, J. Marot, L. Brochier, N. Joachimowicz, H. Roussel, and C. Migliaccio, “Nondestructive control of fruit quality via millimeter waves and classification techniques: Investigations in the automated health monitoring of fruits,” *IEEE Antennas and Propagation Magazine*, vol. 62, no. 5, pp. 43–54, 2020.

[104] F. Zidane, J. Lanteri, L. Brochier, N. Joachimowicz, H. Roussel, and C. Migliaccio, “Damaged apple sorting with mmwave imaging and nonlinear support vector machine,” *IEEE Transactions on Antennas and Propagation*, vol. 68, no. 12, pp. 8062–8071, 2020.

[105] F. Zidane, J. Lanteri, C. Migliaccio, and J. Marot, "System measurement optimized for damages detection in fruit," in *2021 IEEE Conference on Antenna Measurements & Applications (CAMA)*, pp. 550–554, IEEE, 2021.

[106] E. Kızılay, C. Aydinalp, and M. N. Akinci, "Neural network-based classification for walnut state using microwave scattering parameters," *Authorea Preprints*, 2023.

[107] M. El Abed, J.-Y. Dauvignac, J. Lanteri, and C. Migliaccio, "Liquid classification based on mmw experiments and multiclass svm," in *2024 IEEE International Symposium on Antennas and Propagation and INC/USNC-URSI Radio Science Meeting (AP-S/INC-USNC-URSI)*, pp. 1153–1154, IEEE, 2024.

[108] W. B. Teseme and H. W. Weldeselassie, "Review on the study of dielectric properties of food materials," *Am. J. Eng. Technol. Manag*, vol. 5, pp. 76–83, 2020.

[109] S. O. Nelson, "Chapter 11 - dielectric properties of selected food materials," in *Dielectric Properties of Agricultural Materials and their Applications* (S. O. Nelson, ed.), pp. 147–165, San Diego: Academic Press, 2015.

[110] B. Tıraş, S. Dede, and F. Altay, "Dielectric properties of foods," *Turkish Journal of Agriculture-Food Science and Technology*, vol. 7, no. 11, pp. 1805–1816, 2019.

[111] A. Darwish, M. Ricci, J. A. Tobon Vasquez, C. Migliaccio, and F. Vipiana, "Near-field microwave sensing technology enhanced with machine learning for the non-destructive evaluation of packaged food and beverage products," *Scientific Reports*, vol. 14, no. 1, p. 13413, 2024.

[112] K. Technologies, "Keysight streamline series usb vector network analyzer p937xa 2-port, up to 26.5 ghz," *Data Sheet Tech. Specif.*, vol. 85, pp. 1–24, 2018.

[113] "M980xa series PXIe vector network analyzer, data sheet." https://www.keysight.com/us/en/assets/3119-1014/data-sheets/5992-3596.pdf. Accessed: 2024-01-10.

[114] C. A. Balanis, *Antenna theory: analysis and design*. John wiley & sons, 2015.

[115] S. K. Palaniswamy, M. Kanagasabai, S. A. Kumar, M. G. N. Alsath, S. Velan, and J. K. Pakkathillam, "Super wideband printed monopole antenna for ultra wideband applications," *International Journal of Microwave and Wireless Technologies*, vol. 9, no. 1, pp. 133–141, 2017.

[116] O. M. Bucci and G. Franceschetti, "On the degrees of freedom of scattered fields," *IEEE transactions on Antennas and Propagation*, vol. 37, no. 7, pp. 918–926, 1989.

[117] O. Bucci and T. Isernia, "Electromagnetic inverse scattering: Retrievable information and measurement strategies," *Radio science*, vol. 32, no. 6, pp. 2123–2137, 1997.

[118] O. M. Bucci, L. Crocco, and R. Scapaticci, "On the optimal measurement configuration for magnetic nanoparticles-enhanced breast cancer microwave imaging," *IEEE Transactions on Biomedical Engineering*, vol. 62, no. 2, pp. 407–414, 2014.

[119] O. M. Bucci, C. Gennarelli, and C. Savarese, "Representation of electromagnetic fields over arbitrary surfaces by a finite and nonredundant number of samples," *IEEE Transactions on Antennas and Propagation*, vol. 46, no. 3, pp. 351–359, 1998.

[120] M. Ricci, J. A. T. Vasquez, R. Scapaticci, L. Crocco, and F. Vipiana, "Multi-antenna system for in-line food imaging at microwave frequencies," *IEEE Transactions on Antennas and Propagation*, vol. 70, no. 8, pp. 7094–7105, 2022.

[121] C. H. Benson[1] and P. J. Bosscher, "Time-domain reflectometry (tdr) in geotechnics: a review," *Nondestructive and automated testing for soil and rock properties*, vol. 1350, p. 113, 1999.

[122] H. H. Nissen and P. Moldrup, "Theoretical background for the tdr methodology," in *Proceedings of the symposium: time domain reflectometry applications in soil science*, vol. 16, pp. 9–23, 1994.

[123] N. Kumar, S. Sonowal, *et al.*, "Email spam detection using machine learning algorithms," in *2020 Second International Conference on Inventive Research in Computing Applications (ICIRCA)*, pp. 108–113, IEEE, 2020.

[124] V. Y. Chong, *Handwritten Digit Recognition Using Neural Network*. PhD thesis, Universiti Malaysia Sabah, 2004.

[125] M. Li, Y. Jiang, Y. Zhang, and H. Zhu, "Medical image analysis using deep learning algorithms," *Frontiers in Public Health*, vol. 11, p. 1273253, 2023.

[126] Z. Ahmed, S. Amizadeh, M. Bilenko, R. Carr, W.-S. Chin, Y. Dekel, X. Dupre, V. Eksarevskiy, S. Filipi, T. Finley, *et al.*, "Machine learning at microsoft with ml. net," in *Proceedings of the 25th ACM SIGKDD international conference on knowledge discovery & data mining*, pp. 2448–2458, 2019.

[127] C. Wang, Y. Wu, S. Chen, S. Liu, J. Li, Y. Qian, and Z. Yang, "Self-supervised learning for speech recognition with intermediate layer supervision," *arXiv preprint arXiv:2112.08778*, 2021.

[128] G. Tanzer, M. Suzgun, E. Visser, D. Jurafsky, and L. Melas-Kyriazi, "A benchmark for learning to translate a new language from one grammar book," *arXiv preprint arXiv:2309.16575*, 2023.

[129] P. Nagaraj, R. Banala, and A. K. Prasad, "Real time face recognition using effective supervised machine learning algorithms," in *Journal of Physics: Conference Series*, vol. 1998, p. 012007, IOP Publishing, 2021.

[130] A. McGregor, M. Hall, P. Lorier, and J. Brunskill, "Flow clustering using machine learning techniques," in *Passive and Active Network Measurement: 5th International Workshop, PAM 2004, Antibes Juan-les-Pins, France, April 19-20, 2004. Proceedings 5*, pp. 205–214, Springer, 2004.

[131] G. Punj and D. W. Stewart, "Cluster analysis in marketing research: Review and suggestions for application," *Journal of marketing research*, vol. 20, no. 2, pp. 134–148, 1983.

[132] A. E. Ezugwu, A. M. Ikotun, O. O. Oyelade, L. Abualigah, J. O. Agushaka, C. I. Eke, and A. A. Akinyelu, "A comprehensive survey of clustering algorithms: State-of-the-art machine learning applications, taxonomy, challenges, and future research prospects," *Engineering Applications of Artificial Intelligence*, vol. 110, p. 104743, 2022.

[133] I. Syarif, A. Prugel-Bennett, and G. Wills, "Unsupervised clustering approach for network anomaly detection," in *Networked Digital Technologies: 4th International Conference, NDT 2012, Dubai, UAE, April 24-26, 2012. Proceedings, Part I 4*, pp. 135–145, Springer, 2012.

[134] A. Pinto, L.-C. Herrera, Y. Donoso, and J. A. Gutierrez, "Enhancing critical infrastructure security: Unsupervised learning approaches for anomaly detection," *International Journal of Computational Intelligence Systems*, vol. 17, no. 1, p. 236, 2024.

[135] H. Zhou and Y. Zhang, "Unsupervised community detection algorithm based on graph convolution network and social media," *Mobile Information Systems*, vol. 2022, no. 1, p. 4368829, 2022.

[136] M. W. Libbrecht and W. S. Noble, "Machine learning applications in genetics and genomics," *Nature Reviews Genetics*, vol. 16, no. 6, pp. 321–332, 2015.

[137] D. He, Y. Song, D. Jin, Z. Feng, B. Zhang, Z. Yu, and W. Zhang, "Community-centric graph convolutional network for unsupervised community detection," in *Proceedings of the twenty-ninth international conference on international joint conferences on artificial intelligence*, pp. 3515–3521, 2021.

[138] C. Cortes and V. Vapnik, "Support vector networks," *Machine Learning*, vol. 20, pp. 273–297, 1995.

[139] A. Janjic, I. Akduman, M. Cayoren, O. Bugdayci, and M. E. Aribal, "Support vector machine algorithm for clinical microwave breast cancer screening and early detection," in *2023 IEEE Conference on Antenna Measurements and Applications (CAMA)*, pp. 344–346, IEEE, 2023.

[140] F. Zidane, V. L. Coli, J. Lanteri, J. Marot, L. Brochier, D. Binder, and C. Migliaccio, "Artificial intelligence-based low-terahertz imaging for archaeological shards' classification," *IEEE Transactions on Antennas and Propagation*, vol. 70, no. 8, pp. 6300–6312, 2022.

[141] F. Pedregosa, G. Varoquaux, A. Gramfort, V. Michel, B. Thirion, O. Grisel, M. Blondel, P. Prettenhofer, R. Weiss, V. Dubourg, J. Vanderplas, A. Passos, D. Cournapeau, M. Brucher, M. Perrot, and E. Duchesnay, "Scikit-learn: Machine learning in Python," *Journal of Machine Learning Research*, vol. 12, pp. 2825–2830, 2011.

[142] F. Rosenblatt, *The perceptron: a theory of statistical separability in cognitive systems (Project Para)*. Cornell Aeronautical Laboratory, 1958.

[143] T. Amr, *Hands-On Machine Learning with scikit-learn and Scientific Python Toolkits: A practical guide to implementing supervised and unsupervised machine learning algorithms in Python*. Packt Publishing Ltd, 2020.

[144] D. Kinga, J. B. Adam, *et al.*, "A method for stochastic optimization," in *International conference on learning representations (ICLR)*, vol. 5, p. 6, San Diego, California;, 2015.

[145] D. C. Liu and J. Nocedal, "On the limited memory bfgs method for large scale optimization," *Mathematical Programming*, vol. 45, pp. 503–528, 1989.

[146] R. H. Byrd, P. Lu, J. Nocedal, and C. Zhu, "A limited memory algorithm for bound constrained optimization," *SIAM Journal on scientific computing*, vol. 16, no. 5, pp. 1190–1208, 1995.

[147] A. Nielsen, "Neural networks and deep learning," 2015.

[148] P. E. Hart, D. G. Stork, R. O. Duda, *et al.*, *Pattern classification*. Wiley Hoboken, 2000.

[149] R. Garnett, *Bayesian optimization*. Cambridge University Press, 2023.

[150] S. Sharma, S. Sharma, and A. Athaiya, "Activation functions in neural networks," *Towards Data Sci*, vol. 6, no. 12, pp. 310–316, 2017.

[151] Y. Bai, "Relu-function and derived function review," in *SHS Web of Conferences*, vol. 144, p. 02006, EDP Sciences, 2022.

[152] M. Badiger and J. A. Mathew, "Retrospective review of activation functions in artificial neural networks," in *Proceedings of Third International Conference on Communication, Computing and Electronics Systems: ICCCES 2021*, pp. 905–919, Springer, 2022.

[153] A. D. Jagtap and G. E. Karniadakis, "How important are activation functions in regression and classification? a survey, performance comparison, and future directions," *Journal of Machine Learning for Modeling and Computing*, vol. 4, no. 1, 2023.

[154] S. Wold, K. Esbensen, and P. Geladi, "Principal component analysis," *Chemometrics and Intelligent Laboratory Systems*, vol. 2, no. 1, pp. 37–52, 1987. Proceedings of the Multivariate Statistical Workshop for Geologists and Geochemists.

[155] J. D. Horel, "Complex principal component analysis: Theory and examples," *Journal of climate and Applied Meteorology*, pp. 1660–1673, 1984.

[156] L. I. Smith, "A tutorial on principal components analysis," tech. rep., Cornell University, USA, February 26 2002.

[157] S. Mirjalili, S. M. Mirjalili, and A. Lewis, "Grey wolf optimizer," *Advances in engineering software*, vol. 69, pp. 46–61, 2014.

[158] F. Zidane, *Tri de pommes par imagerie microonde*. PhD thesis, Université Côte d'Azur, 2022.

[159] A. Darwish, M. Ricci, J. T. Vasquez, C. Migliaccio, and F. Vipiana, "Support vector machine for multiclass contaminant classification in food products using microwave sensing," in *2024 IEEE International Symposium on Antennas and Propagation and INC/USNC-URSI Radio Science Meeting (AP-S/INC-USNC-URSI)*, pp. 931–932, IEEE, 2024.

[160] M. Ricci, B. Štitić, L. Urbinati, G. Di Guglielmo, J. A. T. Vasquez, L. P. Carloni, F. Vipiana, and M. R. Casu, "Machine-learning-based microwave sensing: A case study for the food industry," *IEEE Journal on Emerging and Selected Topics in Circuits and Systems*, vol. 11, no. 3, pp. 503–514, 2021.

[161] F. Zidane, J. Lantéri, L. Brochier, J. Marot, and C. Migliaccio, "Fruit sorting with amplitude-only measurements," in *2021 18th European Radar Conference (EuRAD)*, pp. 373–376, IEEE, 2022.

[162] A. Darwish, M. Ricci, F. Zidane, J. A. T. Vasquez, M. R. Casu, J. Lanteri, C. Migliaccio, and F. Vipiana, "Physical contamination detection in food industry using microwave and machine learning," *Electronics*, vol. 11, no. 19, p. 3115, 2022.

[163] A. Darwish, M. Ricci, J. A. T. Vasquez, C. Migliaccio, and F. Vipiana, "Microwave-assisted detection of physical intrusions in commercial food packaged products via machine learning," in *2024 54th European Microwave Conference (EuMC)*, pp. 573–576, IEEE, 2024.

[164] F. Nsengiyumva, C. Migliaccio, L. Brochier, J.-Y. Dauvignac, I. Aliferis, and C. Pichot, "New w-band scattering measurement system: Proof of concept and results for 2-d objects," *IEEE Transactions on Antennas and Propagation*, vol. 66, no. 12, pp. 7224–7236, 2018.

[165] F. Nsengiyumva, C. Migliaccio, L. Brochier, J. Lanteri, J.-Y. Dauvignac, and C. Pichot, "90 ghz, 3-d scattered field measurements for investigation of foreign object debris," *IEEE Transactions on Antennas and Propagation*, vol. 67, no. 9, pp. 6217–6222, 2019.

[166] C. Pichot, "Introduction à l'imagerie microonde," *lecture notes, University of Nice-Sophia Antipolis, Electronics, Antennas and Telecommunications Laboratory (LEAT)*, 2012.

[167] P. Lobel, C. Picbota, L. B. Feraud, and M. Barlaud, "Conjugate gradient algorithm with edge-preserving regularization for image reconstruction from experimental data," in *IEEE Antennas and Propagation Society International Symposium. 1996 Digest*, vol. 1, pp. 644–647, IEEE, 1996.

[168] A. Zeitler, *Investigation of mm-wave imaging and radar systems*. PhD thesis, Université Nice Sophia Antipolis; Universität Ulm, 2013.

[169] E. Por, M. van Kooten, and V. Sarkovic, "Nyquist–shannon sampling theorem," *Leiden University*, vol. 1, no. 1, pp. 1–2, 2019.

[170] N. Otsu *et al.*, "A threshold selection method from gray-level histograms," *Automatica*, vol. 11, no. 285-296, pp. 23–27, 1975.

List of Figures

List of Tables

Contrôle non destructif de produits alimentaires par imagerie microonde et millimétrique

---

Controllo non distruttivo dei prodotti alimentari mediante imaging a microonde e onde millimetriche

---

Non-destructive Evaluation of Food Products by Microwave and mmW Imaging

---

Ali Darwish